VRIJE UNIVERSITEIT BRUSSEL

A search for flavour changing neutral currents involving a top quark and a Z boson, using the data collected by the CMS collaboration at a centre-of-mass energy of 13 TeV

Isis Van Parijs

Proefschrift ingediend met het oog op het behalen van de academische graad Doctor in de Wetenschappen.

Published in Faculteit Wetenschappen & Bio-ingenieurswetenschappen
Vrije Universiteit Brussel
At 10 November 2017.

Responsible Contact: Isis Van Parijs
Intitute for High Energy Physics
Promotor: Prof. Jorgen D'Hondt

First Referee: Prof. Dr. J. D’Hondt
Date of Hand-in: 10 November 2017
Date of Defense: 10 December 2017

Contents

1 Theoretical basis

The Standard Model (SM) [1] is a name given in the 1970s to a theory describing the fundamental particles and their interactions. This quantum field theory describes the particles and their interactions as fields and has successfully incorporated three of the four fundamental forces in the universe. In Section 1.1, the particle content of the SM is summarised, while Section 1.2 describes the SM Lagrangian and its symmetries. In Section 1.3, the flavour content of the SM is highlighted, and Section 1.4 focusses on the top quark in the SM. The latest experimental results related to the properties of the top quark are summarised in Section **??**.

The successful theory of the SM has some shortcomings which are discussed in Section 1.6 and lead to searches for a more general theory. One of such is using an effective field theory (EFT) approach [2] to search for new physics in a model independent way. In Section 1.7 an EFT model focussing on flavour changing neutral currents (FCNC) involving a top quark is presented. Its current experimental constraints are given in Section 1.8.

1.1 Elementary particles and forces

The interactions in nature can be described by four forces, the strong force, the electromagnetic (EM) force, the weak force and the gravitational force. These interactions happen via particles with an integer spin known as bosons. The strong interaction is mediated by eight gluons g, while the electromagnetic force is mediated by photons γ, and the weak force by Zand $W^{\pm}$ bosons. In Table 1.1, the forces and their characteristics are shown. The gravitational force is the only force not included in the SM and can be neglected for energies lower than the Planck scale (1.22×10^{19} GeV).

Table 1.1: The four forces of nature and their characteristics.

	Range	Mediator
Strong force	10^{-15} m	8 gluons
Electromagnetic force	∞	photon
Weak force	10^{-18} m	$W^{\pm}$, Zbosons
Gravitational force	∞	unknown

The fermions are the particles that make up the visible matter in the universe. They carry half integer spin and can be subdivided into leptons and quarks, where leptons do not interact strongly. Each fermion has a corresponding anti-fermion which has the same mass and is oppositely charged. The electron e is the first elementary particle discovered [3] and belongs to the first generation of leptons together with the electron neutrino ν_e. The second generation comprises the muon μ and muon neutrino ν_μ, whereas the third generation consists of the tau τ and tau neutrino ν_τ. The neutrinos are neutral particles, while the other leptons have charge $\pm q_\mathrm{e}$ with q_e representing the elementary charge of 1.602×10^{-19} C. The masses of charged leptons differ by four orders of magnitude between the first and third generations. In the SM the neutrinos are assumed to be massless, nonetheless it is experimentally established that neutrinos do have a tiny non-zero mass [4, 5]. In Table 1.2, the leptons and their properties in the SM are summarised.

Table 1.2: The properties of the leptons in the three generations of the SM [6], where q_e represents the elementary charge.

Generation	Particle	Mass	Charge
First	e^-	0.511 MeV	$-q_\mathrm{e}$
	ν_e	≈ 0	0
Second	μ^-	106 MeV	$-q_\mathrm{e}$
	ν_μ	≈ 0	0
Third	τ^-	1 777 MeV	$-q_\mathrm{e}$
	ν_τ	≈ 0	0

The quarks can also be divided into three generations. Unlike the leptons, they carry colour charge and can interact via the strong interaction. The top quark, discovered in 1995 at the Tevatron [7, 8], is the heaviest SM particle with a mass[1] measured to be $173.34 \pm 0.27(\mathrm{stat}) \pm 0.71(\mathrm{syst})$ GeV [9]. The quarks and their properties are summarised in Table 1.3. In nature, only colour neutral objects can exist. This has as consequence that quarks are bound through gluons into mesons (quark+anti-quark) and baryons (three quarks). These mesons and baryons are mostly short-lived and unstable particles that rapidly decay through $\mathrm{W}^\pm$ and Z bosons. The only known stable baryon is the proton, made up of two up quarks and one down quark.

The scalar boson, commonly known as the Higgs boson, is the last piece of the SM discovered in 2012 [10, 11]. It is responsible for the masses of the $\mathrm{W}^\pm$ and Zboson, and that of the fermions.

1.2 Standard Model Lagrangian, connecting fields with particles

The SM is a quantum field theory and thus describes the dynamics and kinematics of particles and forces by a Lagrangian $\mathscr{L}$. The theory is based on the $\mathrm{SU(3)_C} \times \mathrm{SU(2)_L} \times \mathrm{U(1)_Y}$ gauge symmetry, where $\mathrm{SU(2)_L} \times \mathrm{U(1)_Y}$ describes the electroweak interaction and $\mathrm{SU(3)_C}$ the strong

[1] In this thesis all masses and energies are expressed in natural units, where the speed of light and $\hbar$ are taken to be equal to one.

Table 1.3: The properties of the quarks in the three generations of the SM [6], where q_e represents the elementary charge.

Generation	Particle	Mass	Charge
First	up u	$2.2^{+0.6}_{-0.4}$ MeV	$\frac{2}{3}\ q_e$
	down d	$4.7^{+0.5}_{-0.4}$ MeV	$\frac{-1}{3}\ q_e$
Second	charm c	1.28 ± 0.03 GeV	$\frac{2}{3}\ q_e$
	strange s	96^{+8}_{-4} MeV	$\frac{-1}{3}\ q_e$
Third	top t	173.1 ± 0.6 GeV	$\frac{2}{3}\ q_e$
	bottom b	$4.18^{+0.04}_{-0.03}$ GeV	$\frac{-1}{3}\ q_e$

interaction. The indices refer to colour C, the left chiral nature of the $\mathrm{SU(2)_L}$ coupling L, and the weak hypercharge Y. Its Lagrangian is constructed such that contains symmetries representing physics conservation laws such as conservation of energy, momentum and angular momentum. The symmetries under local gauge transformations are sustained by demanding gauge invariance[2].

The $\mathrm{U(1)_Y}$ group has one generator Y with an associated gauge field B_μ. The three gauge fields W^1_μ, W^2_μ, and W^3_μ, are associated to $\mathrm{SU(2)_L}$ with three generators that can can be written as half of the Pauli matrices:

$$T_1 = \frac{1}{2}\begin{pmatrix} 0 & 1 \\ 1 & 0 \end{pmatrix},\ T_2 = \frac{1}{2}\begin{pmatrix} 0 & -i \\ i & 0 \end{pmatrix},\ \text{and } T_3 = \frac{1}{2}\begin{pmatrix} 1 & 0 \\ 0 & -1 \end{pmatrix}. \tag{1.1}$$

The generators T^a satisfy the Lie algebra:

$$\left[T_a, T_b\right] = i\epsilon_{abc}T^c \text{ and} \left[T_a, Y\right] = 0, \tag{1.2}$$

where ϵ_{abc} is an antisymmetric tensor. The gauge fields of $\mathrm{SU(2)_L}$ only couple to left-handed fermions as required by the observed parity violating nature of the weak force. The $\mathrm{SU(3)_C}$ group represents quantum chromodynamics (QCD). It has eight generators corresponding to eight gluon fields $\mathrm{G}^{1\ldots8}_\mu$. Unlike $\mathrm{SU(2)_L} \times \mathrm{U(1)_Y}$, $\mathrm{SU(3)_C}$ is not chiral.

Under $\mathrm{SU(3)_C}$ quarks are colour triplets while leptons are colour singlets. This implies that the quarks carry a colour index ranging between one and three, whereas leptons do not take part in strong interactions. Based on the chirality, the quarks and leptons are organized in doublets or singlets. Each generation i of fermions consists of left-handed doublets and right-handed singlets:

$$\mathrm{l_{L,i}} = \begin{pmatrix} \mathrm{e_{L,i}} \\ \nu_{\mathrm{L,i}} \end{pmatrix},\ \mathrm{e_{R,i}},\ \mathrm{q_{L,i}} = \begin{pmatrix} \mathrm{u_{L,i}} \\ \mathrm{d_{L,i}} \end{pmatrix},\ \mathrm{u_{R,i}},\ \text{and } \mathrm{d_{R,i}} \tag{1.3}$$

The SM Lagrangian can be decomposed as a sum of four terms

$$\mathscr{L}_{\mathrm{SM}} = \mathscr{L}_{\mathrm{gauge}} + \mathscr{L}_{\mathrm{f}} + \mathscr{L}_{\mathrm{Yuk}} + \mathscr{L}_{\phi}, \tag{1.4}$$

[2]Different field configurations of unobservable fields can result in identical quantities. Transformations between such configurations are called gauge transformation and the absence of change in the measurable quantities is a characteristic called gauge invariance.

that are related to the gauge, fermion, Yukawa and scalar sectors. The gauge Lagrangian regroups the gauge fields of all three symmetry groups, and the fermionic part consists of kinetic energy terms for quarks and leptons. The interaction between fermions and the scalar doublet ϕ gives rise to fermion masses and is described by the Yukawa Lagrangian. The scalar part of the Lagrangian is composed of a kinematic and potential component related to the scalar boson.

For the electroweak theory, two coupling constants are introduced, namely g' for $\mathrm{U}(1)_\mathrm{Y}$ and g for $\mathrm{SU}(2)_\mathrm{L}$. The physically observable gauge bosons of this theory are the photon field A_μ, the Z boson field Z^0_μ, and the W boson fields $\mathrm{W}^\pm_\mu$. These are a superposition of the four gauge fields of $\mathrm{SU}(2)_\mathrm{L} \times \mathrm{U}(1)_\mathrm{Y}$:

$$\mathrm{A}_\mu = \sin\theta_\mathrm{W}\mathrm{W}^3_\mu + \cos\theta_\mathrm{W}\mathrm{B}_\mu,\ \mathrm{Z}^0_\mu = \cos\theta_\mathrm{W}\mathrm{W}^3_\mu - \sin\theta_\mathrm{W}\mathrm{B}_\mu,\ \text{and } \mathrm{W}^\pm_\mu = \sqrt{\frac{1}{2}}\left(\mathrm{W}^1_\mu \mp i\mathrm{W}^2_\mu\right), \quad (1.5)$$

where θ_W represents the weak mixing angle defined as $\tan\theta_\mathrm{W} = \frac{g'}{g}$.

The coupling constant representing the strength of the QCD interactions is denoted as g_s. In QCD their is asymptotic freedom whereby the strong coupling constant becomes weaker as the energy with which the interaction between strongly interacting particles is probed increases, and stronger as the distance between the particles increases. A consequence of this is known as colour confinement, the quarks and gluons can not exist on their own and are not observed individually. They are bound in colour neutral states called hadrons, this process is known as hadronisation.

Electroweak symmetry breaking

In $\mathscr{L}_\mathrm{gauge}$ and $\mathscr{L}_\mathrm{f}$ are no mass terms for fermions present because only singlets under $\mathrm{SU}(3)_\mathrm{C} \times \mathrm{SU}(2)_\mathrm{L} \times \mathrm{U}(1)_\mathrm{Y}$ can acquire a mass with an interaction of the type $m^2\phi^\dagger\phi$ without breaking the gauge invariance. In order to accommodate mass terms for fermions and gauge fields, electroweak symmetry breaking, leading to $\mathscr{L}_\phi$ is introduced.

The scalar doublet is introduced in the SM as

$$\phi = \frac{1}{\sqrt{2}}\begin{pmatrix}\varphi_1 + i\varphi_2 \\ \varphi_3 + i\varphi_4\end{pmatrix}. \quad (1.6)$$

Its field potential is of the form

$$V(\phi) = \mu^2\phi^\dagger\phi + \lambda(\phi^\dagger\phi)^2, \quad (1.7)$$

with $\mu^2 < 0$ and λ a positive integer. This choice of parameters gives the potential a "Mexican hat" shape. It has an infinite set of minima (ground states) and by expanding the field around an arbitrary choice of ground state, the electroweak symmetry is broken ($\not{\mathrm{EW}}$):

$$\phi = \begin{pmatrix}0 \\ \frac{v}{\sqrt{2}}\end{pmatrix} + \hat{\phi}, \quad (1.8)$$

where v is the vacuum expectation value (vev), measured to be around 245 GeV and corresponds to $\sqrt{\frac{-\mu}{\lambda}}$. The scalar doublet's four degrees of freedom are reduced to three degrees of freedom that couple to the gauge fields and fix the W^+, W^- and Zbosons. The remaining fourth degree of freedom has given rise to a physically observable particle, called the Brout-Englert-Higgs (BEH) boson. This spontaneous symmetry breaking leaves the gauge invariance intact and gives masses to the $W^\pm$ and Zbosons as:

$$m_W = \frac{1}{2} v |g| \quad \text{and} \quad m_Z = \frac{1}{2} v \sqrt{g'^2 + g^2}. \tag{1.9}$$

The Brout-Englert-Higgs field couples universally to fermions with a strength proportional to their masses, and to gauge bosons with a strength proportional to the square of their masses.

1.3 Flavours in the SM

Flavour changing charged currents are introduced in 1963 by Nicola Cabibbo [12]. Via interactions with a W boson the flavour of the quarks is changed. At the time of the postulation only up, down, and strange quarks were known and the charged weak current was described as a coupling between the up quark and d_{weak}, where d_{weak} is a linear combination of the down and strange quarks, $d_{weak} = \cos\theta_c d + \sin\theta_c s$. This linear combination is a direct consequence of the chosen rotation

$$\begin{pmatrix} d_{weak} \\ s_{weak} \end{pmatrix} = \begin{pmatrix} \cos\theta_c & \sin\theta_c \\ -\sin\theta_c & \cos\theta_c \end{pmatrix} \begin{pmatrix} d \\ s \end{pmatrix} = \mathscr{R} \begin{pmatrix} d \\ s \end{pmatrix}, \tag{1.10}$$

where the rotation angle θ_c is known as the Cabibbo angle. This provides a definition for the charged weak current between u and d quarks,

$$J_\mu = \bar{u} \gamma_\mu (1 + \gamma_5) d_{weak}. \tag{1.11}$$

A consequence of Cabibbo's approach is that the s_{weak} is left uncoupled, leading to Glashow, Iliopoulos and Maiani (GIM) [13–15] to require the existence of a fourth quark with charge $\frac{2}{3} q_e$. This quark, known as the charm quark, couples to s_{weak} and a new definition of the charged weak current is modified to

$$J_\mu = \begin{pmatrix} \bar{u} & \bar{c} \end{pmatrix} \gamma_\mu (1 + \gamma_5) \mathscr{R} \begin{pmatrix} d \\ s \end{pmatrix} = \bar{U} \gamma_\mu (1 + \gamma_5) \mathscr{R} D. \tag{1.12}$$

The neutral weak current is defined as

$$J_3 = \bar{U} \gamma_\mu (1 + \gamma_5) \left[\mathscr{R}, \mathscr{R}^\dagger \right] D, \tag{1.13}$$

and is diagonal in flavour space. This has as consequence that no flavour changing neutral currents occur at tree-level interactions [1].

Kobayashi and Maskawa generalised the Cabibbo rotation matrix to accommodate a third generation of quarks. The result is a 3×3 unitary matrix known as the CKM matrix, responsible for the mixing of weak interaction states of down-type quarks:

$$\begin{pmatrix} d_{weak} \\ s_{weak} \\ b_{weak} \end{pmatrix} = \begin{pmatrix} V_{ud} & V_{us} & V_{ub} \\ V_{cd} & V_{cs} & V_{cb} \\ V_{td} & V_{ts} & V_{tb} \end{pmatrix} \begin{pmatrix} d \\ s \\ b \end{pmatrix} = \mathscr{V}_{CKM} \begin{pmatrix} d \\ s \\ b \end{pmatrix}, \tag{1.14}$$

where $\mathscr{V}_{\mathrm{CKM}}$ is unitary ($\mathscr{V}^{\dagger}_{\mathrm{CKM}}\mathscr{V}_{\mathrm{CKM}} = \mathbb{1}$). A general 3×3 unitary matrix depends on three real angles and six phases. For the CKM matrix, the freedom to redefine the phases of the quark eigenstates can remove fives of the phases, leaving a single physical phase known as the Kobayashi-Maskawa phase. This phase is responsible for the charge parity violation in the SM [16]. Each element V_{ij} of $\mathscr{V}_{\mathrm{CKM}}$ represents the transition probability of a quark i going to a quark j, and is experimentally determined to be [6]

$$\mathscr{V}_{\mathrm{CKM}} = \begin{pmatrix} 0.97425 \pm 0.00022 & 0.2253 \pm 0.0008 & (4.13 \pm 0.49) \times 10^{-3} \\ 0.225 \pm 0.008 & 0.986 \pm 0.016 & (41.1 \pm 1.3) \times 10^{-3} \\ (8.4 \pm 0.6) \times 10^{-3} & (40.0 \pm 2.7)\, 10^{-3} & 1.021 \pm 0.032 \end{pmatrix}. \tag{1.15}$$

From Equation 1.15 follows that top quarks predominantly decay via charged weak currents to bottom quarks, with a probability consistent with unity. In the SM, FCNC can only occur via higher loop interactions which are highly suppressed. The expected transition probabilities for a top quark decaying via a FCNC interaction in the SM are given in Table 1.4, where it is clear that the FCNC top quark interactions of the SM is still beyond the reach of the sensitivity of current experiments.

Table 1.4: The predicted branching ratios $\mathscr{B}$ for FCNC decays involving the top quark in the SM [17].

Process	$\mathscr{B}$ in the SM	Process	$\mathscr{B}$ in the SM
$\mathrm{t} \to \mathrm{uZ}$	8×10^{-17}	$\mathrm{t} \to \mathrm{cZ}$	1×10^{-14}
$\mathrm{t} \to \mathrm{u}\gamma$	4×10^{-16}	$\mathrm{t} \to \mathrm{c}\gamma$	5×10^{-14}
$\mathrm{t} \to \mathrm{ug}$	4×10^{-14}	$\mathrm{t} \to \mathrm{cg}$	5×10^{-12}
$\mathrm{t} \to \mathrm{uH}$	2×10^{-17}	$\mathrm{t} \to \mathrm{cH}$	3×10^{-15}

1.4 The top quark in the SM

Discovered in 1995 by the CDF and D0 collaborations at the Tevatron with proton-antiproton data [18, 19], the top quark plays an important role in studying high energy physics. Its Yukawa interaction is given by

$$\mathscr{L}_{\mathrm{top-Yukawa}} = -\frac{\lambda_t v}{\sqrt{2}}\bar{\mathrm{t}}_{\mathrm{L}}\mathrm{t}_{\mathrm{R}} - \frac{\lambda_{\mathrm{t}}}{\sqrt{2}}\mathrm{H}\bar{\mathrm{t}}_{\mathrm{L}}\mathrm{t}_{\mathrm{R}} + \mathrm{h.c.}, \tag{1.16}$$

yielding a Yukawa coupling of [6]

$$\lambda_{\mathrm{t}} = \frac{\sqrt{2}m_{\mathrm{t}}}{v} = 0.991 \pm 0.003. \tag{1.17}$$

This Yukawa coupling is very large compared to the other Yukawa couplings in the SM ($\mathscr{O}(10^{-2})$), leading to the belief that the top quark may have an important role in understanding the mechanism of electroweak symmetry breaking. On top of this, the very short lifetime of the top quark makes it an excellent candidate to study the properties of a bare quark. Its high mass, almost 40 times higher than the mass of the closest fermion in mass, leads to a large coupling with the Higgs boson and makes the top quark an interesting candidate to investigate how particles acquire mass.

The CKM matrix element V_{tb}, given in Equation 1.15, is experimentally found to be much larger than V_{ts}, V_{td}, and close to unity. The top quark decays through electroweak interactions since the W boson mass is smaller than the top quark mass and the W boson can be on shell. A consequence of this is that the top quark has a very short lifetime of only $1/\Gamma_t \approx 5\,10^{-25}$ s [6] leading to the fact that the formation of bound states involving top quarks are not allowed. This lifetime is even shorter than the typical hadronisation timescale of $1/\Lambda_{QCD} \approx 10^{-23}$ s, prohibiting gluons to radiate from the top quark and keeping its spin coherent. Since the electroweak interactions have a vector-axial vector (V-A) coupling structure[3] , the top quark spin orientation can be derived from the angular distributions of its decay products. This makes it possible to study the polarisation of top quarks from the angular distributions in various processes.

The massiveness of the top quark leads to the fact that a large amount of energy is needed to create one. This is only the case for high energy collisions such as those happening in the Earth's upper atmosphere when cosmic rays collide with particles in air, or by particle accelerators. The production of top quarks happens in two ways: single via the electroweak interaction or in pairs via the strong interaction. At hadron colliders, the dominant production mechanism is top quark production via gluon ($gg \to t\bar{t}$) or quark fusion ($q\bar{q} \to t\bar{t}$). In Figure 1.1, the different top quark pair production mechanisms are shown. The production channel of gluon fusion is the main contributor to the top quark pair cross section the LHC compared to quark fusion at the Tevatron. The $gg \to t\bar{t}$ process contributes 80-90% to the total top quark pair cross section in the LHC centre-of-mass energy regime of 7-14 TeV [6]. In Table 1.5 the predicted top quark pair production cross sections are given for the LHC and the Tevatron, while in Figure 1.2, a summary plot of the LHC and Tevatron top quark pair cross section measurements as a function of the centre-of-mass energy can be found.

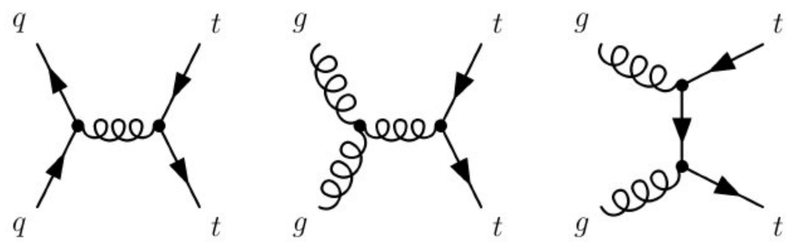

Figure 1.1: Leading order diagrams of the top quark pair production. Gluon fusion (right and middle) are the dominant processes at the LHC, while quark fusion (left) is the dominant one at the Tevatron.

The singly produced top quarks are produced via the electroweak interaction. These production mechanisms are subdivided at leading order into three main channels based on the virtuality ($Q^2 = -p_\mu p^\mu$) of the exchanged W boson. In Figure 1.3, the corresponding Feynman diagrams are shown. The single top quark production cross sections, given in Table 1.6, are smaller than

[3] In the SM a vector - axial vector coupling structure $\left(\gamma^\mu - \gamma^\mu\gamma^5\right)$ is predicted that only permits left-handed fermions or right-handed anti fermions to interact with a spin-1 particle.

Table 1.5: Predictions on the top quark pair production cross sections at next-to-next-to-leading order with next-to-next-to-leading log soft gluon resummation per centre-of-mass energy [6]. The first uncertainty is from scale dependence, while the second uncertainty originates from parton density functions.

Experiment	Top quark mass	Centre-of-mass energy	Cross section (pb)
Tevatron	$m_t = 173.3$ GeV	$\sqrt{s} = 1.96$ TeV	$\sigma_{t\bar{t}} = 7.16^{+0.11+0.17}_{-0.20-0.12}$
LHC	$m_t = 173.2$ GeV	$\sqrt{s} = 7$ TeV	$\sigma_{t\bar{t}} = 173.6^{+4.5+8.9}_{-5.9-8.9}$
LHC	$m_t = 173.2$ GeV	$\sqrt{s} = 8$ TeV	$\sigma_{t\bar{t}} = 247.7^{+6.3+11.5}_{-8.5-11.5}$
LHC	$m_t = 173.2$ GeV	$\sqrt{s} = 13$ TeV	$\sigma_{t\bar{t}} = 816.0^{+19.4+34.4}_{-28.6-34.4}$

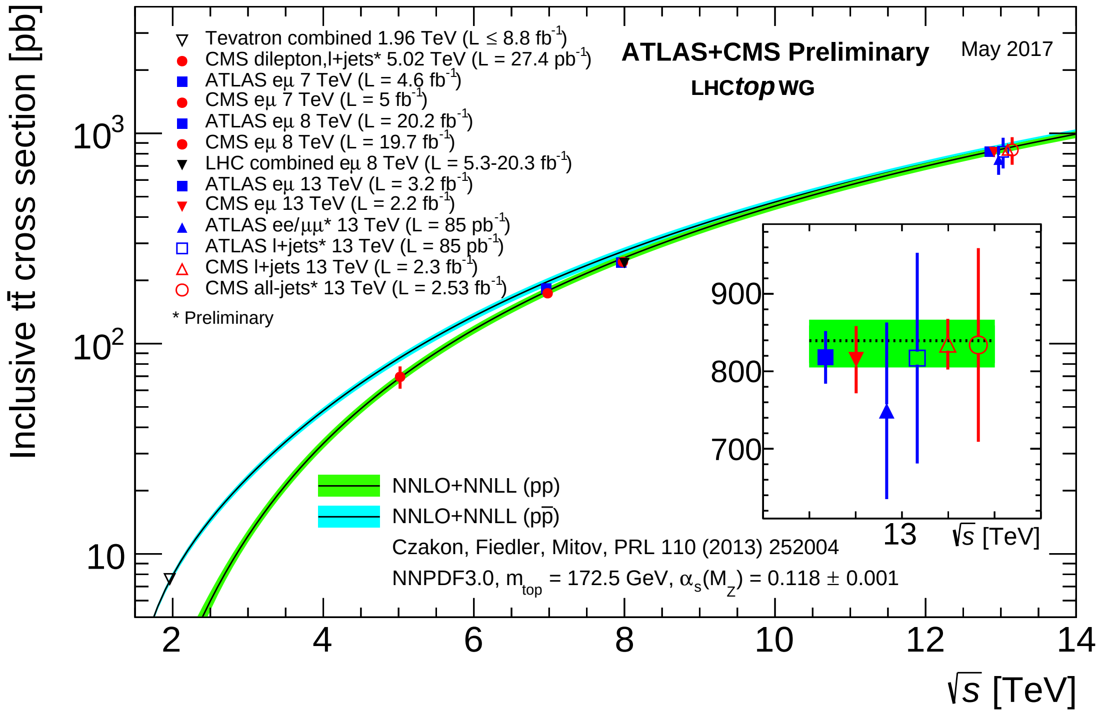

Figure 1.2: Summary of the LHC and the Tevatron measurements of the top quark pair production cross section as function of the centre-of-mass energy compared with the next-to-next-to-leading order QCD calculation. The theory bands are the uncertainties due to renormalization and factorisation scales, parton density functions and the strong coupling. The mass of the top quark is assumed to be 172.5 GeV. Measurements for the same centre-of-mass energy are slightly off-set for clarity. Figure taken from [20].

the top quark pair production cross sections since the electroweak coupling strength is smaller than the strong coupling strength. In addition, for the single top quark production, there is the need of sea quarks (b, q̄) in the initial states for which the parton density functions increase less steeply at low momentum fractions compared to the gluon parton density functions.

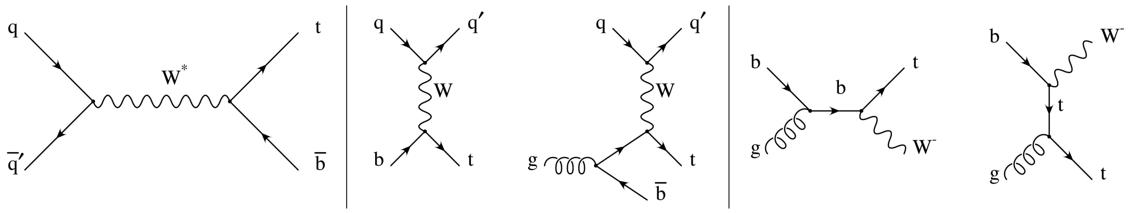

Figure 1.3: Leading order Feynman diagrams of the electroweak production of single top quarks in the s-channel (left), t-channel (middle), and for the tW associated production. Figure taken from [21].

The production via the t-channel has a virtuality of the W boson $Q^2 > 0$, making it space-like. It is produced via the scattering of the W boson of a bottom quark coming from a proton or from gluon splitting (g→bb̄). It has the highest single top quark cross section in proton collisions and the top quark production is roughly twice as large than the antitop quark. This is a consequence of the up-down valence quark composition of the proton. This feature makes the t-channel sensitive to the parton density functions of the proton. The s-channel is the production mechanism with the smallest cross section. Here the W boson is time-like ($Q^2 < 0$) which requires the W boson to have a large virtuality to produce the heavier top quark. It is produced from two quarks belonging to the same isodoublet (e.g. ud̄) and subsequently decays to tb̄. This process get enhanced by many beyond the Standard Model scenarios via the addition of new heavy particles such as W'. The tW-channel has a top quark produced in association with a W boson produced on shell $Q^2 = -m_{\mathrm{W}}^2$. This mode is negligible at the Tevatron, but of relevant size at the LHC. The tW-channel is sensitive to new physics affecting the Wtb vertex. The single top quark production cross section measurements by the CMS collaboration can be found in Figure 1.4.

Table 1.6: Predictions on the single top quark production cross sections at next-to-leading order per centre-of-mass energy [6]. The uncertainties from scale dependence and from parton density functions are combined in quadrature or given separately (scale + PDF). For the t-channel the relative proportions to t and t̄ are 65% and 35%. For the s-channel this is respectively 69% and 31%. The tW-channel has an equal proportion of top and antitop quarks. For Tevatron, the top quark mass is assumed to be 173.3 GeV, while the LHC predictions use $m_{\mathrm{t}} = 172.5$ GeV [6, 22].

Collider	Centre-of-mass energy	Cross section $\sigma_{\mathrm{t+\bar{t}}}$ (pb)		
		t-channel	s-channel	tW-channel
Tevatron	$\sqrt{s} = 1.96$ TeV	$2.06^{+0.13}_{-0.13}$	$1.03^{+0.05}_{-0.05}$	-
LHC	$\sqrt{s} = 7$ TeV	$63.89^{+2.91}_{-2.52}$	$4.29^{+0.19}_{-0.17}$	$15.74^{+0.40+1.10}_{-0.40-1.14}$
LHC	$\sqrt{s} = 8$ TeV	$84.69^{+3.76}_{-3.23}$	$5.24^{+0.22}_{-0.20}$	$22.37^{+0.60+1.40}_{-0.60-1.40}$
LHC	$\sqrt{s} = 13$ TeV	$216.99^{+9.04}_{-7.71}$	$10.32^{+0.40}_{-0.36}$	$71.7^{+1.80+3.40}_{-1.80-3.40}$

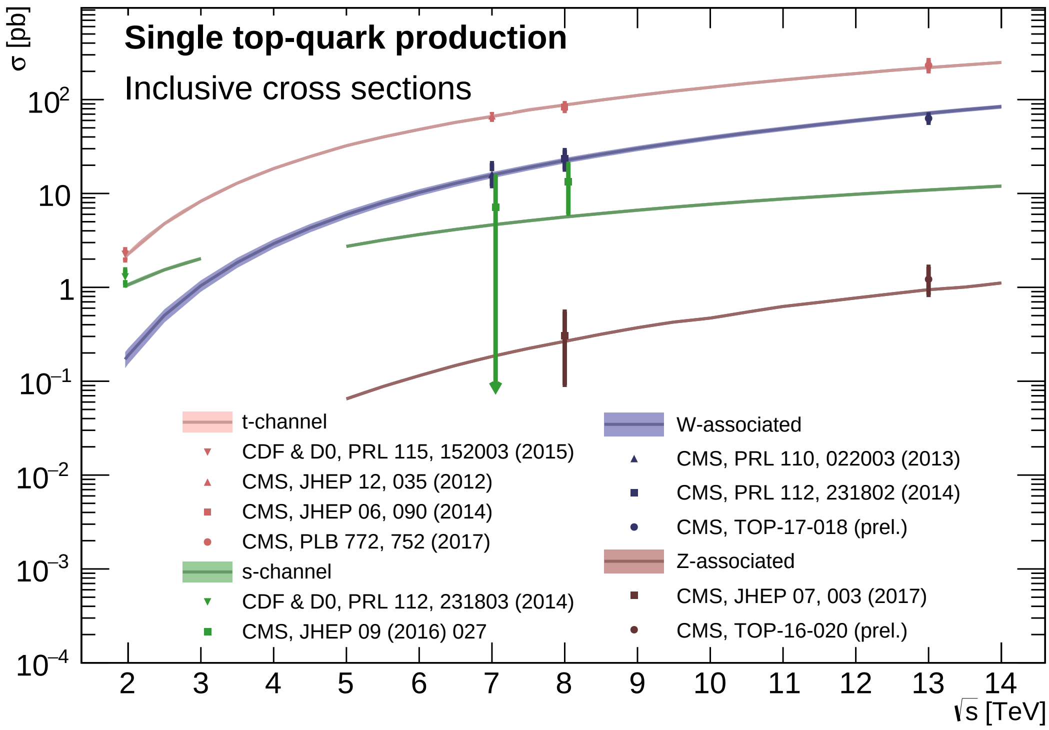

Figure 1.4: Summary of the measurements of the single top top quark production cross section as function of the centre-of-mass energy. Figure taken from [23].

1.5 Effective field theories

Problems can be simplified if one looks at the relevant scale of the process that one want to investigate, for example the chemical properties of an hydrogen atom can be described without any knowledge of quark interactions inside the proton. In this case, the proton can be considered the elementary object (indivisible) due to the fact that the binding energy of the constituents is much bigger than the energy of the electron in orbit around the proton. Effective field theories are based on this kind of separation of different energy scales in a system [24]. Effective field theories can be used for theories where the perturbative expansion cannot be trusted, e.g. QCD at low energy, or as bottom up approach to look for new physics in a model independent way. The latter is the way effective field theory will be used throughout this thesis.

The main idea behind effective field theory is easily explained via the example of the Fermi theory. Fermi explained in 1933 [25] the β-decay as a product of currents:

$$\mathscr{L}_{\mathrm{EFT}}^{\mathrm{Fermi}} = -\frac{G_{\mathrm{F}}}{\sqrt{2}} J^{\mu} J_{\mu}^{\dagger}, \tag{1.18}$$

where G_{F} is the Fermi coupling constant, measured to be $G_{\mathrm{F}} \approx 1.17 \times 10^{-5}$ GeV^{-2}. The current J_{μ} can written as the sum of an hadronic J_{μ}^{h} and leptonic J_{μ}^{l} current, where for simplicity only the leptonic current will be used further.

$$J^l_\mu = \sum_l \bar{\nu}_l \gamma_\mu \left(1-\gamma_5\right) l. \tag{1.19}$$

Historically, charged currents were flavour universal and the later discovered parity violation of the weak interaction led to the V-A structure. After this the $SU(2)_L$ symmetry was postulated and the existence of neutral currents was predicted. The effective Lagrangian used then (given in Equation 1.18), could nowadays be build starting from $SU(2)_L$ symmetries only.

The muon decay can be computed from two different starting points. The effective Fermi Lagrangian provides the decay width of the muon into an electron and two neutrinos

$$\Gamma(\mu \to e\bar{\nu}_e\nu_\mu) \approx \frac{1}{96\pi^3}\frac{m_\mu^2}{\Lambda_F^4}, \tag{1.20}$$

where Λ_F is the energy scale defined as

$$\frac{G_F}{\sqrt{2}} = \frac{1}{\Lambda_F^2}. \tag{1.21}$$

From muon decay measurements, the value of Λ_F is determined to be $\Lambda_F \approx 348\text{GeV}$ [24]. From the SM Lagrangian, one could also calculate the muon decay. Considering that the momenta involved are small compared to the W boson mass, the propagator's denominator can be expanded as [1]

$$\frac{1}{p^2-m_W^2} = -\frac{1}{m_W^2} - \frac{p^2}{m_W^4} + \ldots \tag{1.22}$$

Looking at the first term, and identifying

$$\frac{g^2}{8m_W} = \frac{1}{\Lambda_F}^2, \tag{1.23}$$

one sees that this corresponds with Equation 1.20, thus the effective Lagrangian in Equation 1.18 is the first term of the expansion in $\frac{1}{m_W^2}$ applied on the full Lagrangian.

An effective theory is thus a Taylor expansion in the ratio of two scales and the only remnants of the full theory at low energies are the symmetries and the values of the coupling constants. If the expansion parameter is small, one can truncate the series leading to the Lagrangian containing a a finite number of free coefficients, making predictions possible. The error on these predictions are then of the order as the truncated piece.

The SM can be seen as an effective theory applicable up to energies not exceeding a scale Λ. Therefore, remnants should still be valid and the theory above that scale should have a gauge group containing $SU(3)_C \times SU(2)_L \times U(1)_Y$ and all the SM degrees of freedom, as well as reduce to the SM at lower energies. The general SM Lagrangian becomes then

$$\mathscr{L}_{SM+EFT} = \mathscr{L}^{(4)}_{SM} + \frac{1}{\Lambda}\sum_k C_k^{(5)}Q_k^{(5)} + \frac{1}{\Lambda^2}\sum_k C_k^{(6)}Q_k^{(6)} + \mathscr{O}\left(\frac{1}{\Lambda^3}\right), \tag{1.24}$$

where $Q_{\mathrm{k}}^{(n)}$ are dimension-n operators (currents) and $C_{\mathrm{k}}^{(n)}$ the corresponding dimensionless coupling constants, so-called Wilson coefficients. The Wilson coefficients are determined by the underlying high energy theory.

In the Warsaw basis [26], a set of independent operators of dimension 5 and 6 are built out of the SM fields and are consistent with the SM gauge symmetries and is fully derived in Ref. [26]. In general the various measurements show a good agreement with the SM predictions and by lack of deviations from the SM, limits on the anomalous couplings can be derived. The estimated coupling strengths per operator contributing to single top quark production obtained from various measurements at the LHC and Tevatron are shown in Figure 1.5 for which the conventions are discussed in Ref. [27]. These results are consistent with the SM expectation for which those operators vanish.

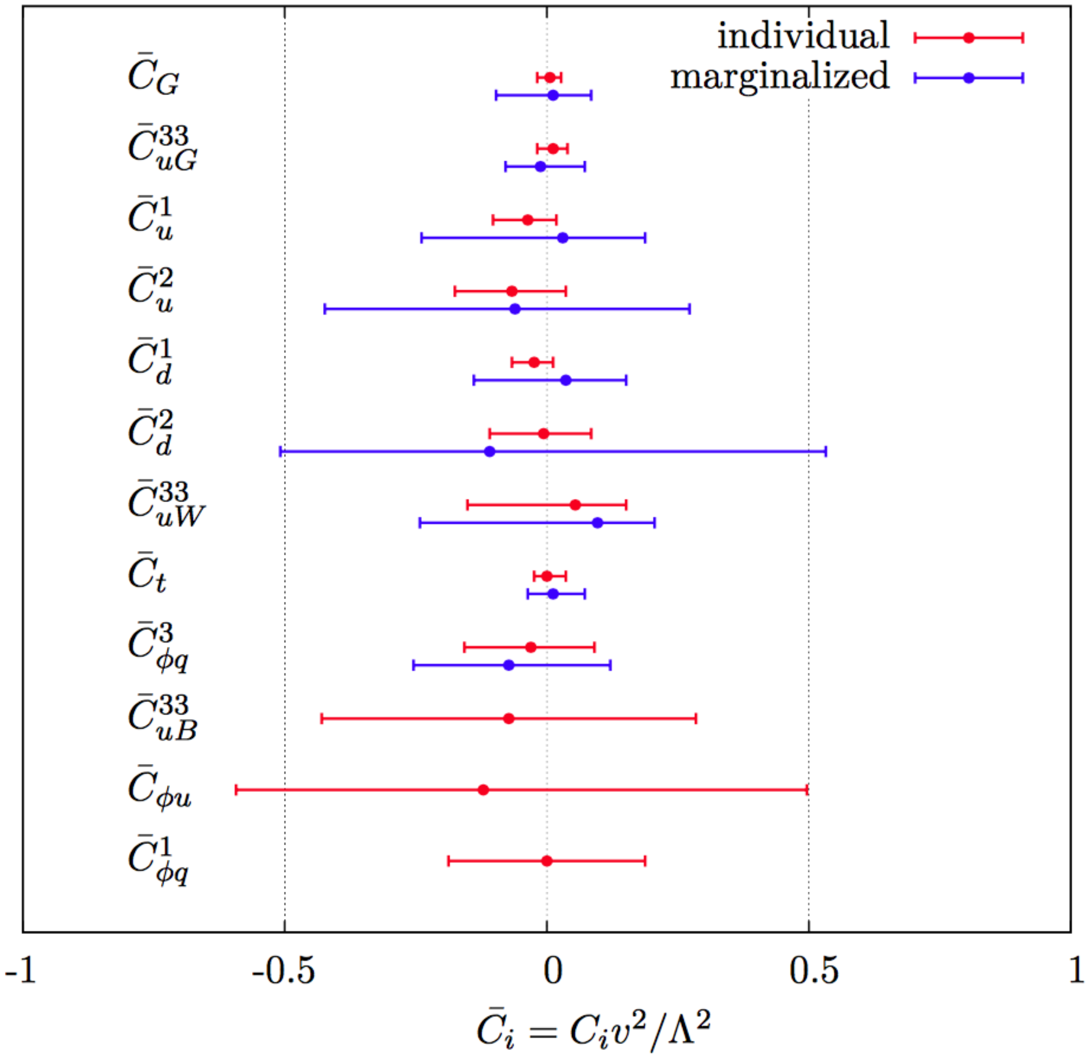

Figure 1.5: Global fit results of top quark effective field theory to experimental data including all constrained operators at dimension six. For the operators, the Warsaw basis of [26] is used. The bounds are set on the Wilson coefficients of various operators contributing to top quark production and decay in two cases (red) all other coefficients set to zero, or (blue) all other coëfficient are marginalised over. Figure taken from [28].

1.6 Motivation for new physics

Many high energy experiments confirm the success of the SM. In particular the scalar boson, the cornerstone of the SM, has consecrated the theory. Unfortunately there are also strong indications that the SM ought to be a lower energy expression of a more global theory. The existence of physics beyond the SM (BSM) [29] is strongly motivated. These motivations are based on direct evidence from observation such as the existence of neutrino masses, the existence of dark matter and dark energy, or the matter-antimatter asymmetry, and also from theoretical problems such as the hierarchy problem, the coupling unification or the large numbers of free parameters in the SM.

In the SM, the neutrinos are assumed to be massless, while experiments with solar, atmospheric, reactor and accelerator neutrinos have established that neutrinos can oscillate and change flavour during flight [4, 5]. These oscillations are only possible when neutrinos have masses. The flavour neutrinos (ν_e, ν_μ, ν_τ) are then linear expressions of the fields of at least three mass eigenstate neutrinos ν_1, ν_2, and ν_3.

The ordinary or baryonic matter described by the SM describes only 5% of the mass (energy) content of the universe. Astrophysical evidence indicated that dark matter is contributing to approximately 27%, and dark energy to 68% of the content of the universe. From the measurements of the temperature and polarizations anisotropies of the cosmic microwave background by the Planck experiment [30], the density of cold non baryonic matter is determined. Cold dark matter is assumed to be only sensitive to the weak and gravitational force, leading to only one possible SM candidate: the neutrino. However, these are too light to account for the vast amount of dark matter and other models are needed. Dark energy is assumed to be responsible for the acceleration in the expansion of the universe [31].

At the Big Bang matter and antimatter are assumed to be produced in equal quantities. However, it is clear that we are surrounded by matter. So where did all the antimatter go? In 1967, Sakharov identified three mechanisms that are necessary to obtain a global matter antimatter asymmetry [32]. These mechanisms are those of baryon and lepton number violation, that at a given moment in time there was a thermal imbalance for the interactions in the universe, and there is charge C and charge parity CP violation[4].

The large number of free parameters in the SM comes from the nine fermion masses, three CKM mixing angles and one CP violating phase, one EM coupling constant g', one weak coupling constant g, one strong coupling constant g_s, one QCD vacuum angle, one vacuum expectation value, and one mass of the scalar boson. This large number of free parameters leads to the expectation of a more elegant and profound theory beyond the SM.

The hierarchy problem [33] is related to the huge difference in energy between the weak scale and the Planck scale. The vev of the Brout-Englert-Higgs field determines the weak scale that is approximately 246 GeV. The radiative corrections to the scalar boson squared mass m_{H}^2, coming from its self couplings and couplings to fermions and gauge bosons, are quadratically

[4]The rate of a process $i \to f$ can be different from the CP-conjugate process: $\bar{i} \to \bar{f}$. The SM includes sources of CP-violation through the residual phase of the CKM matrix. However, these could not account for the magnitude of the asymmetry observed.

proportional to the ultraviolet momentum cut-off Λ_{UV}. This cut-off is at least equal to the energy to which the SM is valid without the need of new physics. For the SM to be valid up to the Planck mass, the correction to m_{H}^2 becomes thirty orders of magnitude larger than m_{H}^2. This implies that an extraordinary cancellation of terms should happen. This is also known as the naturalness problem of the H boson mass.

The correction to the squared mass of the scalar boson coming from a fermion f, coupling to the scalar field ϕ with a coupling λ_{f} is given by

$$\Delta m_{\mathrm{H}}^2 = -\frac{\left|\lambda_{\mathrm{f}}\right|^2}{8\pi^2}\Lambda_{\mathrm{UV}}^2, \tag{1.25}$$

while the correction to the mass from a scalar particle S with a mass m_{S}, coupling to the scalar field with a Lagrangian term $-\lambda_{\mathrm{S}}|\phi|^2|\mathrm{S}|^2$ is

$$\Delta m_{\mathrm{H}}^2 = \frac{\left|\lambda_{\mathrm{S}}\right|^2}{16\pi^2}\left(\Lambda_{\mathrm{UV}}^2 - 2m_{\mathrm{S}}^2 \ln\left(\frac{\Lambda_{\mathrm{UV}}}{m_{\mathrm{S}}}\right) + \ldots\right). \tag{1.26}$$

As one can see the correction term to m_{H}^2 is much larger than m_{H}^2 itself. By introducing BSM physics models that introduce new scalar particles at the TeV scale that couple to the scalar boson one can cancel the Λ_{UV}^2 divergence and avoid this fine-tuning.

The choice of the $\mathrm{SU}(3)_{\mathrm{C}} \times \mathrm{SU}(2)_{\mathrm{L}} \times \mathrm{U}(1)_{\mathrm{Y}}$ symmetry group itself as well as the separate treatment of the three forces included in the SM raises concern. The intensity of the forces show a large disparity around the electroweak scale, but have comparable strengths at higher energies. The electromagnetic and weak forces are unified in a electroweak interaction, but the strong coupling constant does not encounter the other coupling constants at high energies. In order to reach a grand unification, the running of couplings can be modified by the addition of new particles in BSM models.

1.7 An effective approach beyond the SM: FCNC involving a top quark

The closeness of the top quark mass to the electroweak scale led physicist to believe that it is a sensitive probe for new physics. Studying its properties is therefore an important topic of the experimental program at the LHC. Several extensions of the SM enhance the FCNC branching ratios and can be probed at the LHC [17], from which some of them are shown in Table 1.7. Previous searches have been performed at the Tevatron by the CDF [34] and D0 [35] collaborations, and at the LHC by the ATLAS [36–40] and CMS [41–45] collaborations.

The impact of BSM models can be written in a model independent way by means of an effective field theory valid up to an energy scale Λ. The leading effects are parametrized by a set of fully gauge symmetric operators that are added to the SM Lagrangian and can be reduced to a minimal set of operators as seen in Equation 1.24. For simplicity, the assumption is made that new physics effects are exclusively described by dimension-6 operators, thus neglecting

Table 1.7: The predicted branching ratios $\mathscr{B}$ for FCNC interactions involving the top quark in some BSM models [17]: quark singlet (QS), generic two Higgs doublet model (2HDM) and the minimal supersymmetric extensions to the SM (MSSM);

Process	QS	2HDM	MSSM	Process	QS	2HDM	MSSM
$t \to uZ$	$\leq 1.1 \times 10^{-4}$	–	$\leq 2 \times 10^{-6}$	$t \to cZ$	$\leq 1.1 \times 10^{-4}$	$\leq 10^{-7}$	$\leq 2 \times 10^{-6}$
$t \to u\gamma$	$\leq 7.5 \times 10^{-9}$	–	$\leq 2 \times 10^{-6}$	$t \to c\gamma$	$\leq 7.5 \times 10^{-9}$	$\leq 10^{-6}$	$\leq 2 \times 10^{-6}$
$t \to ug$	$\leq 1.5 \times 10^{-7}$	–	$\leq 8 \times 10^{-5}$	$t \to cg$	$\leq 1.5 \times 10^{-7}$	$\leq 10^{-4}$	$\leq 8 \times 10^{-5}$
$t \to uH$	$\leq 4.1 \times 10^{-5}$	$\leq 5.5\ 10^{-6}$	$\leq 10^{-5}$	$t \to cH$	$\leq 4.1 \times 10^{-5}$	$\leq 10^{-3}$	$\leq 10^{-5}$

neutrino physics. In the fully gauge symmetric case, the EFT Lagrangian is then given by

$$\mathscr{L}_{\mathrm{SM+EFT}} = \mathscr{L}_{\mathrm{SM}} + \sum_{\mathrm{i}} \frac{\bar{c}_{\mathrm{i}}}{\Lambda^2} O_{\mathrm{i}} + \mathscr{O}\left(\frac{1}{\Lambda^3}\right), \tag{1.27}$$

where the Wilson coefficients $\bar{c}_{\mathrm{i}}$ depend on the considered theory and on the way that new physics couples to the SM particles. Considering that Λ is large, contributions suppressed by powers of Λ greater than two are neglected. Moreover, all four fermion operators are omitted for the rest of this thesis. The Warsaw basis is adpoted for the independent effective operators [26], parametrising the new physics effects relevant for the flavour changing neutral current interactions of the top quark as, all flavour indices understood,

$$\begin{aligned}
\mathscr{L}^{\mathrm{t}}_{\mathrm{EFT}} = {} & \frac{\bar{c}_{uG}}{\Lambda^2} \Phi^\dagger \cdot \left[\bar{Q}_{\mathrm{L}} \sigma^{\mu\nu} \mathscr{T}_a u_{\mathrm{R}}\right] G^a_{\mu\nu} + \frac{\bar{c}_{uB}}{\Lambda^2} \Phi^\dagger \cdot \left[\bar{Q}_{\mathrm{L}} \sigma^{\mu\nu} u_{\mathrm{R}}\right] B_{\mu\nu} + \frac{2\bar{c}_{uW}}{\Lambda^2} \Phi^\dagger T_{\mathrm{i}} \cdot \left[\bar{Q}_{\mathrm{L}} \sigma^{\mu\nu} u_{\mathrm{R}}\right] W^{\mathrm{i}}_{\mu\nu} \\
& + i \frac{\bar{c}_{hu}}{\Lambda^2} \left[\Phi^\dagger \overleftrightarrow{D}_\mu \Phi\right] \left[\bar{u}_{\mathrm{R}} \gamma^\mu u_{\mathrm{R}}\right] + i \frac{\bar{c}^{(1)}_{hq}}{\Lambda^2} \left[\Phi^\dagger \overleftrightarrow{D}_\mu \Phi\right] \left[\bar{Q}_{\mathrm{L}} \gamma^\mu Q_{\mathrm{L}}\right] \\
& + i \frac{4\bar{c}^{(3)}_{\mathrm{Hq}}}{\Lambda^2} \left[\Phi^\dagger T_i \overleftrightarrow{D}_\mu \Phi\right] \left[\bar{Q}_{\mathrm{L}} \gamma^\mu T^{\mathrm{i}} Q_{\mathrm{L}}\right] + \frac{\bar{c}_{uh}}{\Lambda^2} \Phi^\dagger \Phi\ \Phi^\dagger \cdot \left[\bar{Q}_{\mathrm{L}} u_{\mathrm{R}}\right] + \mathrm{h.c.}\,,
\end{aligned} \tag{1.28}$$

where the left handed $\mathrm{SU}(2)_{\mathrm{L}}$ doublet of the quark fields is denoted by Q_{L}, the up-type right handed fields by u_{R}, the down-type right handed fields by d_{R}, the $\mathrm{SU}(2)_{\mathrm{L}}$ doublet of the Higgs field by Φ, the field strength tensors as

$$\begin{aligned}
B_{\mu\nu} &= \partial_\mu B_\nu - \partial_\nu B_\mu, \\
W^{\mathrm{k}}_{\mu\nu} &= \partial_\mu W^{\mathrm{k}}_\nu - \partial_\nu W^{\mathrm{k}}_\mu - g \epsilon^{\mathrm{k}}_{\mathrm{ij}} W^{\mathrm{i}}_\mu W^{\mathrm{j}}_\nu, \\
\mathrm{G}_{\mu\nu} &= \partial_\mu \mathrm{G}^{\mathrm{a}}_\nu - \partial_\nu \mathrm{G}^{\mathrm{a}}_\mu + g_{\mathrm{s}} f^{\mathrm{a}}_{\mathrm{bc}} \mathrm{G}^{\mathrm{b}}_\mu \mathrm{G}^{\mathrm{c}}_\nu,
\end{aligned} \tag{1.29}$$

denoting the structure constant of the $\mathrm{SU}(3)_{\mathrm{C}}$ group as $f^{\mathrm{a}}_{\mathrm{bc}}$ and the structure constant of the $\mathrm{SU}(2)_{\mathrm{L}}$ group as $\epsilon^{\mathrm{k}}_{\mathrm{ij}}$. The gauge covariant derivatives are also standard defined as

$$D_\mu \Phi = \partial_\mu \Phi - \frac{1}{2} i g' B_\mu \Phi - i g T_{\mathrm{k}} W^{\mathrm{k}}_\mu \Phi \tag{1.30}$$

with the conventions of Section 1.2. The representation matrices T of $\mathrm{SU}(2)_{\mathrm{L}}$ are defined in Equation 1.1, while the representation matrices $\mathscr{T}$ of $\mathrm{SU}(3)_{\mathrm{C}}$ are the Gell-Mann matrices [1].

The hermiatian derivative operator is defined as

$$\Phi^\dagger \overleftrightarrow{D} \Phi = \Phi^\dagger D^\mu \Phi - D_\mu \Phi^\dagger \Phi. \tag{1.31}$$

After electroweak symmetry breaking the operators induce [17, 46] both corrections to the SM couplings and new interactions at tree level such as FCNC interactions. The FCNC interactions of the top quark that are not present in the SM are given by

$$\begin{aligned}
\mathscr{L}^{\mathrm{t}}_{\mathrm{EFT}} = \frac{\sqrt{2}}{2} \sum_{\mathrm{q=u,c}} \Bigg[& g' \frac{\kappa_{\mathrm{t\gamma q}}}{\Lambda} \mathrm{A}_{\mu\nu} \bar{\mathrm{t}} \sigma^{\mu\nu} \left(f^{\mathrm{L}}_{\gamma\mathrm{q}} P_{\mathrm{L}} + f^{\mathrm{R}}_{\gamma\mathrm{q}} P_{\mathrm{R}} \right) \mathrm{q} && (1.32)\\
& + \frac{g}{2\cos\theta_{\mathrm{W}}} \frac{\kappa_{\mathrm{tZq}}}{\Lambda} \mathrm{Z}_{\mu\nu} \bar{\mathrm{t}} \sigma^{\mu\nu} \left(f^{\mathrm{L}}_{\mathrm{Zq}} P_{\mathrm{L}} + f^{\mathrm{R}}_{\mathrm{Zq}} P_{\mathrm{R}} \right) \mathrm{q} && (1.33)\\
& + \frac{\sqrt{2}g}{4\cos\theta_{\mathrm{W}}} \zeta_{\mathrm{tZq}} \bar{\mathrm{t}} \gamma^{\mu} \left(\tilde{f}^{\mathrm{L}}_{\mathrm{q}} P_{\mathrm{L}} + \tilde{f}^{\mathrm{R}}_{\mathrm{q}} P_{\mathrm{R}} \right) \mathrm{q} \mathrm{Z}_{\mu} && (1.34)\\
& + g_{\mathrm{s}} \frac{\kappa_{\mathrm{tgq}}}{\Lambda} \mathrm{Z}_{\mu\nu} \bar{\mathrm{t}} \sigma^{\mu\nu} \left(f^{\mathrm{L}}_{\mathrm{gq}} P_{\mathrm{L}} + f^{\mathrm{R}}_{\mathrm{gq}} P_{\mathrm{R}} \right) \mathrm{q} \mathrm{G}^{\mathrm{a}}_{\mu\nu} && (1.35)\\
& + \eta_{\mathrm{Hqt}} \bar{\mathrm{t}} \left(\hat{f}^{\mathrm{L}}_{\mathrm{q}} P_{\mathrm{L}} + \hat{f}^{\mathrm{R}}_{\mathrm{q}} P_{\mathrm{R}} \right) \mathrm{q} \mathrm{H} + \mathrm{h.c.} \Bigg], && (1.36)
\end{aligned}$$

where the value of the FCNC couplings at scale Λ are represented by κ_{tZq},κ_{tgq},$\kappa_{\mathrm{t\gamma q}}$,$\zeta_{\mathrm{tZq}}$, and η_{Hqt}. These are assumed to be real and positive, with the unit of GeV^{-1} for $\kappa_{\mathrm{tXq}}/\Lambda$ and no unit for ζ_{xqt} and η_{xqt}. In the equation $\sigma^{\mu\nu}$ equals to $\frac{i}{2}\left[\gamma^{\mu}, \gamma^{\nu}\right]$, and the left- and right-handed chirality projector operators are denoted by P_{L} and P_{R}. The electromagnetic coupling constant is denoted by g', the strong interaction coupling is denoted as g_{s}, while the electroweak interaction is parametrised by the coupling constant g and the electroweak mixing angle θ_{W}. The complex chiral parameters are normalized according to $|f^{\mathrm{L}}_{\mathrm{xq}}|^2 + |f^{\mathrm{R}}_{\mathrm{xq}}|^2 = 1$, $|\tilde{f}^{\mathrm{L}}_{\mathrm{q}}|^2 + |\tilde{f}^{\mathrm{R}}_{\mathrm{q}}|^2 = 1$, and $|\hat{f}^{\mathrm{L}}_{\mathrm{q}}|^2 + |\hat{f}^{\mathrm{R}}_{\mathrm{q}}|^2 = 1$. In the expression for $\mathscr{L}^{\mathrm{t}}_{\mathrm{EFT}}$, the unitary gauge is adopted and the scalar field is expanded around its vacuum expectation value v with Hbeing the SM scalar boson, and the field strength tensors of the photon A_{μ}, the gluon field $\mathrm{G}^{1\ldots8}_{\mu}$, and the Z boson Z^{0}_{μ} are defined as

$$\begin{aligned}
\mathrm{A}_{\mu\nu} &= \partial_{\mu}\mathrm{A}_{\nu} - \partial_{\nu}\mathrm{A}_{\mu},\\
\mathrm{Z}_{\mu\nu} &= \partial_{\mu}\mathrm{Z}_{\nu} - \partial_{\nu}\mathrm{Z}_{\mu}, \text{ and}\\
\mathrm{G}_{\mu\nu} &= \partial_{\mu}\mathrm{G}^{\mathrm{a}}_{\nu} - \partial_{\nu}\mathrm{G}^{\mathrm{a}}_{\mu} + g_{\mathrm{s}} f^{\mathrm{a}}_{\mathrm{bc}} \mathrm{G}^{\mathrm{b}}_{\mu} \mathrm{G}^{\mathrm{c}}_{\nu}.
\end{aligned} \tag{1.37}$$

Note that there are two coupling constants arising in $\mathscr{L}^{\mathrm{t}}_{\mathrm{EFT}}$, which is a residue of electroweak symmetry breaking. The massive Z boson will appear in both the Z^{0}_{μ} field as well as the covariant derivative, leading to an extra Z-vertex.

The relations between the Wilson coefficients in (1.28) and the coupling strengths of the interactions in Equation 1.36 can be derived. The 14 effective operators are mapped onto 10 free parameters providing a more minimal parametrisation of the anomalous interactions of the top quark.

$$
\begin{aligned}
\kappa_{\mathrm{tgq}} f^{\mathrm{L}}_{\mathrm{gq}} &= \frac{v}{g_s\Lambda}\left[\bar{c}_{uG}\right]^*_{i3}\,, &
\kappa_{\mathrm{tgq}} f^{\mathrm{R}}_{\mathrm{gq}} &= \frac{v}{g_s\Lambda}\left[\bar{c}_{uG}\right]_{3i}\,,\\
\kappa_{\mathrm{t\gamma q}} f^{\mathrm{L}}_{\mathrm{\gamma q}} &= \frac{v}{g'\Lambda}\left[\cos\theta_{\mathrm{W}}\bar{c}_{uB}-\sin\theta_{\mathrm{W}}\bar{c}_{uW}\right]^*_{i3}\,, &
\kappa_{\mathrm{t\gamma q}} f^{\mathrm{R}}_{\mathrm{\gamma q}} &= \frac{v}{g'\Lambda}\left[\sin\theta_{\mathrm{W}}\bar{c}_{uB}-\cos\theta_{\mathrm{W}}\bar{c}_{uW}\right]_{3i}\,,\\
\kappa_{\mathrm{tZq}} f^{\mathrm{L}}_{\mathrm{Zq}} &= -\frac{2\cos\theta_{\mathrm{W}} v}{g\Lambda}\left[\sin\theta_{\mathrm{W}}\bar{c}_{uB}+\cos\theta_{\mathrm{W}}\bar{c}_{uW}\right]^*_{i3}\,, &
\kappa_{\mathrm{tZq}} f^{\mathrm{R}}_{\mathrm{Zq}} &= -\frac{2\cos\theta_{\mathrm{W}} v}{g\Lambda}\left[\cos\theta_{\mathrm{W}}\bar{c}_{uB}+\sin\theta_{\mathrm{W}}\bar{c}_{uW}\right]_{3i}\,,\\
\zeta_{\mathrm{tZq}} \tilde{f}^{\mathrm{L}}_{\mathrm{Zq}} &= -\frac{2v^2}{\Lambda^2}\left[\left(\bar{c}^{(1)}_{hq}-\bar{c}^{(3)}_{hq}\right)_{i3}+\left(\bar{c}^{(1)}_{hq}-\bar{c}^{(3)}_{hq}\right)^*_{3i}\right]\,, &
\zeta_{\mathrm{tZq}} \tilde{f}^{\mathrm{R}}_{\mathrm{Zq}} &= -\frac{2v^2}{\Lambda^2}\left[(\bar{c}_{hu})_{i3}+(\bar{c}_{hu})^*_{3i}\right]\,,\\
\eta_{\mathrm{tHq}} \hat{f}^{\mathrm{L}}_{\mathrm{Hq}} &= \frac{3v^2}{2\Lambda^2}\left[\bar{c}_{uh}\right]^*_{3i}\,, &
\eta_{\mathrm{tHq}} \hat{f}^{\mathrm{R}}_{\mathrm{Hq}} &= \frac{3v^2}{2\Lambda^2}\left[\bar{c}_{uh}\right]_{i3}\,.
\end{aligned}
\tag{1.38}
$$

1.8 Experimental constraints on top-FCNC

Experiments commonly put limits on the branching ratios which allow an easier interpretation across different EFT models by use of the branching ratio

$$\mathscr{B}(\mathrm{t}\to\mathrm{qX}) = \frac{\delta^2_{\mathrm{tXq}}\Gamma_{\mathrm{t}\to\mathrm{qX}}}{\Gamma_{\mathrm{t}}}, \tag{1.39}$$

where $\Gamma_{\mathrm{t}\to\mathrm{qX}}$ represents the FCNC decay width[5] for a coupling strength $\delta^2_{\mathrm{tXq}} = 1$, and Γ_{t} the full decay width of the top quark. In the SM, supposing a top quark mass of 172.5 GeV, the full width becomes $\Gamma^{\mathrm{SM}}_{\mathrm{t}} = 1.32$ GeV [47].

Searches for top-FCNC usually adopt a search strategy depending on the experimental set-up and the FCNC interaction of interest, looking either for FCNC interactions in the production of a single top quark or in its decay for top quark pair interactions. In Figure 1.6, these two cases are shown for the tZq vertex.

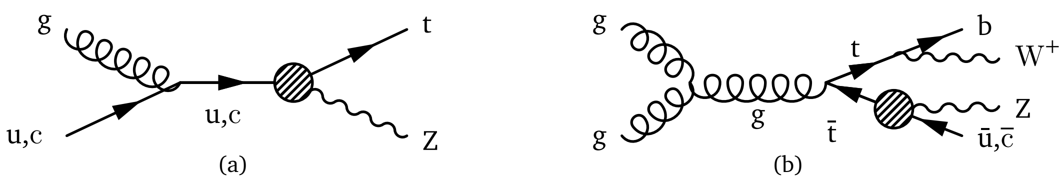

Figure 1.6: Feynman diagrams for the processes with a tZq FCNC interaction, where the FCNC interaction is indicated with the shaded dot. (a) Single top quark production through an FCNC interaction. (b) Top quark pair production with an FCNC induced decay.

[5] The decay width of a certain process represents the probability per unit time that a particle will decay. The total decay width, defined as the sum of all possible decay widths of a particle, is inversely proportional to its lifetime.

The observation of top-FCNC interactions has yet to come and experiments have so far only been able to put upper bounds on the branching ratios. An overview of the best current limits is given in Table 1.8. In Figure 1.7 a comparison is shown between the current best limits set by ATLAS and CMS with respect to several BSM model benchmark predictions. From there one can see that FCNC searches involving a Z or H boson are close to excluding or confirming several BSM theories. In Figure 1.9, the searches performed by CMS are summarised. For the tZq vertex, the best limit from CMS comes from Ref. [41] where both single top quark and top quark pair is studied. The observed (expected) limits 95% CL at 8 TeV for the FCNC tZq interaction by CMS are $\mathcal{B}(t \to uZ) < 2.2 \times 10^{-4}(2.7 \times 10^{-4})$ and $\mathcal{B}(t \to cZ) < 4.9 \times 10^{-4}(12 \times 10^{-4})$. In Figure 1.8, the summary of the 95% confidence level observed limits on the branching ratios of the top quark decays to a charm or up quark and a neutral boson is given, considering the results from the HERA, the LEP, the Tevatron, and the the LHC.

Table 1.8: Overview of the most stringent observed and expected experimental limits on top-FCNC branching ratios $\mathcal{B}$ at 95% confidence level.

Process	Search mode	Observed $\mathcal{B}$	Expected $\mathcal{B}$	Experiment	
$t \to uZ$	top quark pair decay	1.7×10^{-4}	2.4×10^{-4}	ATLAS	[40]
$t \to u\gamma$	single top quark production	1.3×10^{-4}	1.9×10^{-4}	CMS	[43]
$t \to ug$	single top quark production	4.0×10^{-5}	3.5×10^{-5}	ATLAS	[37]
$t \to uH$	top quark pair decay	2.4×10^{-3}	1.7×10^{-3}	ATLAS	[39]
$t \to cZ$	top quark pair decay	2.3×10^{-4}	3.2×10^{-4}	ATLAS	[40]
$t \to c\gamma$	single top quark production	2.0×10^{-3}	1.7×10^{-3}	CMS	[43]
$t \to cg$	single top quark production	2.0×10^{-4}	1.8×10^{-4}	ATLAS	[37]
$t \to cH$	top quark pair decay	2.2×10^{-3}	1.6×10^{-3}	CMS	[39]

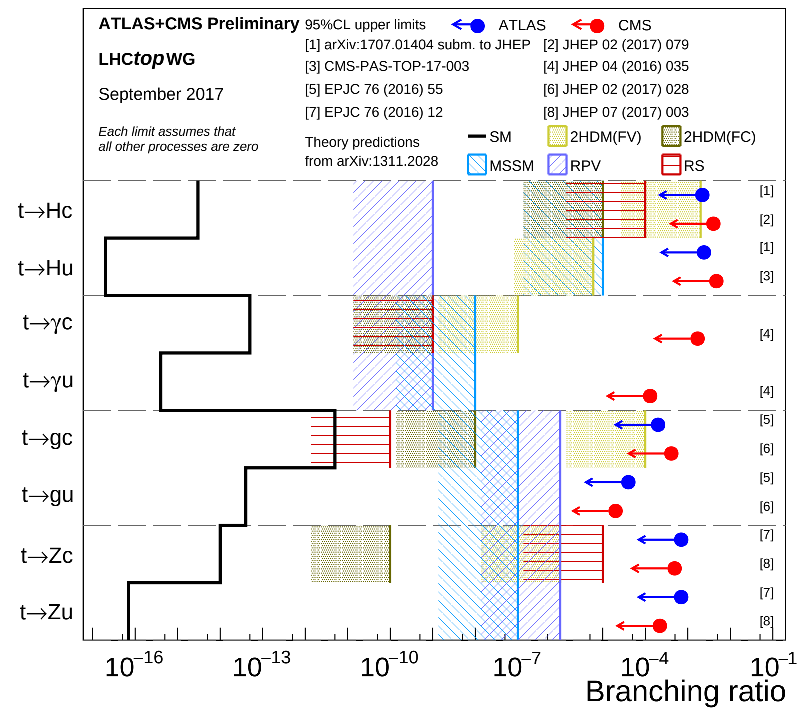

Figure 1.7: Current best limits set by CMS and ATLAS for top-FCNC interactions. Figure taken from [23]. (TO DO Remake with new atlas results)

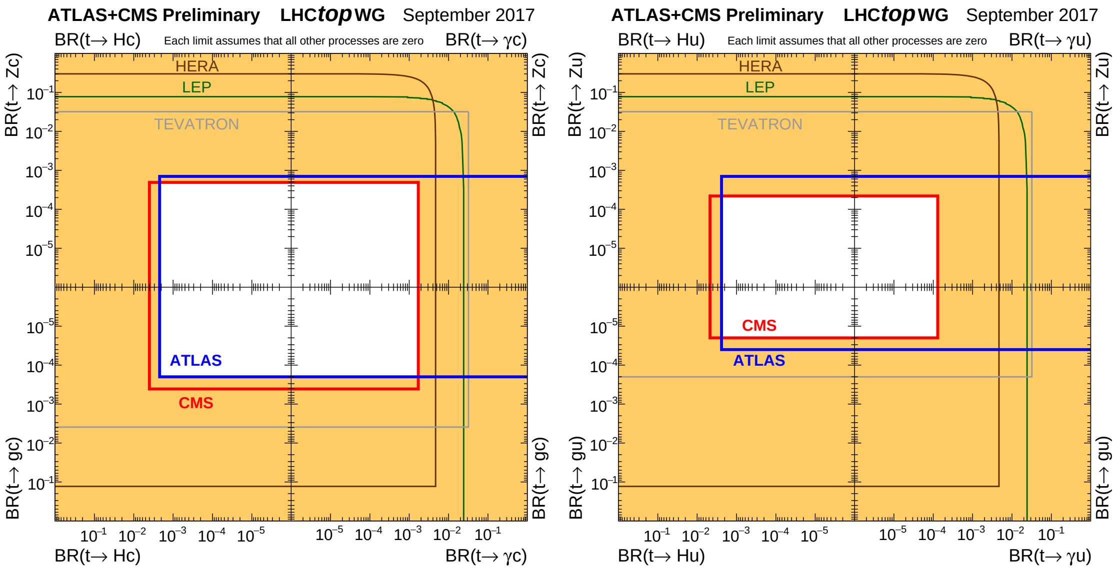

Figure 1.8: Summary of the current 95% confidence level observed limits on the branching ratios of the top quark decays via flavour changing neutral currents to a charm (left) or up (right) quark and a neutral boson. The coloured lines represent the results from HERA (the most stringent limits between the ones obtained by the H1 and ZEUS collaborations, in brown), LEP (combined ALEPH, DELPHI, L3 and OPAL collaborations result, in green), TEVATRON (the most stringent limits between the ones obtained by the CDF and D0 collaborations, in grey). The yellow area represents the region excluded by the ATLAS and the CMS Collaborations. Figure taken from [20].

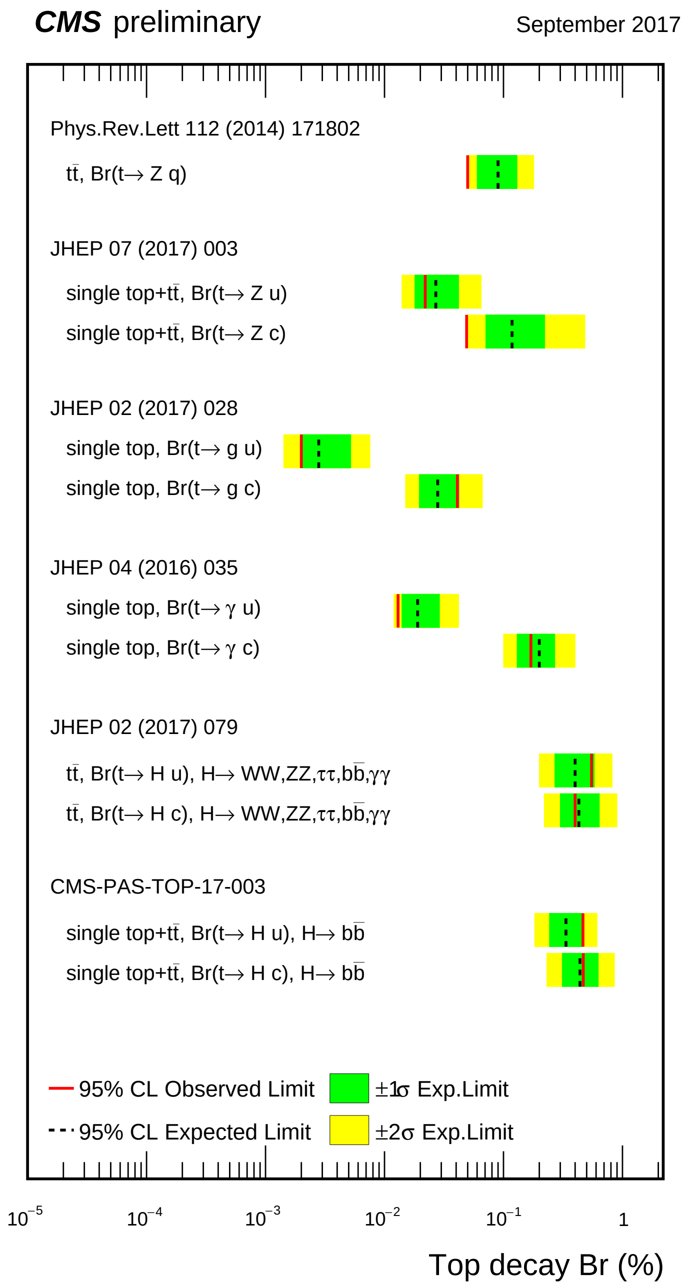

Figure 1.9: Summary of the FCNC branching ratios from CMS searches at 8 TeV. Figure taken from [23].

Experimental set-up 2

A key objective of the Large Hadron Collider (LHC) was the search for the Brout-Englert-Higgs boson. The Large Electron Positron (LEP) [48] and Tevatron [49] experiments established that the mass of the scalar boson has to be larger than 114 GeV [50, 51], and smaller than approximate 1 TeV due to unitarity and perturbativity constraints [52]. On top of this, the search for new physics such as supersymmetry or the understanding of dark matter were part of the motivation for building the LHC. Since the start of its operation, the LHC is pushing the boundaries of the Standard Model, putting the most stringent limits on physics beyond the Standard Model as well as precision measurements of the parameters of the Standard Model. A milestone of the LHC is the discovery the scalar boson in 2012 by the two largest experiments at the LHC [10, 11].

This chapter is dedicated to the experimental set up of the LHC and the Compact Muon Solenoid (CMS) experiment. Section 2.1 describes the LHC and its acceleration process for protons to reach their design energies. The CMS experiment and its components are presented in Section 2.2. The upgrades performed during the long shutdown in 2013 are discussed in Section 2.2.4. The data acquisition of CMS is presented in Section 2.2.3, while the CMS computing model is shown in Section 2.2.5.

2.1 The Large Hadron Collider

The LHC has started its era of cutting edge science on 10 September 2008 [53] after approval by the European Organisation of Nuclear Research (CERN) in 1995 [54]. Installed in the previous LEP tunnel, the LHC consists of a 26.7 km quasi ring, that is installed between 45 and 170 m under the French-Swiss border amidst Cessy (France) and Meyrin (Switzerland). Built to study rare physics phenomena at high energies, the LHC can accelerate mainly two types of particles, protons and lead ions Pb^{45+}, and provides collisions at four interaction points, where the particle bunches are crossing. Experiments for studying the collisions are installed at each interaction point.

As can be seen in Figure 2.1, the LHC is the last element in a chain that creates, injects and accelerates protons. The starting point is the ionisation of hydrogen, creating protons that are injected in a linear accelerator (LINAC 2). Here, the protons obtain an energy of 50 MeV. They continue to the Proton Synchrotron Booster (PSB or Booster), where the packs of protons are accelerated to 1.4 GeV and each pack is split up in twelve bunches with 25 or 50 ns spacing. The Proton Synchrotron (PS) then increases their energy to 25 GeV before the Super Proton Synchrotron (SPS) increases the proton energy up to 450 GeV. Each accelerator ring expands in radius in order to reduce the energy loss of the protons by synchrotron radiation[1] Furthermore, the magnets responsible for the bending of the proton trajectories have to be strong enough to sustain the higher proton energy. Ultimately, the proton bunches are injected into opposite directions into the LHC, where they are accelerated to 3.5 TeV (in 2010 and 2011), 4 TeV (in 2012 and 2013) or 6.5 TeV (in 2015 and 2016) [55].

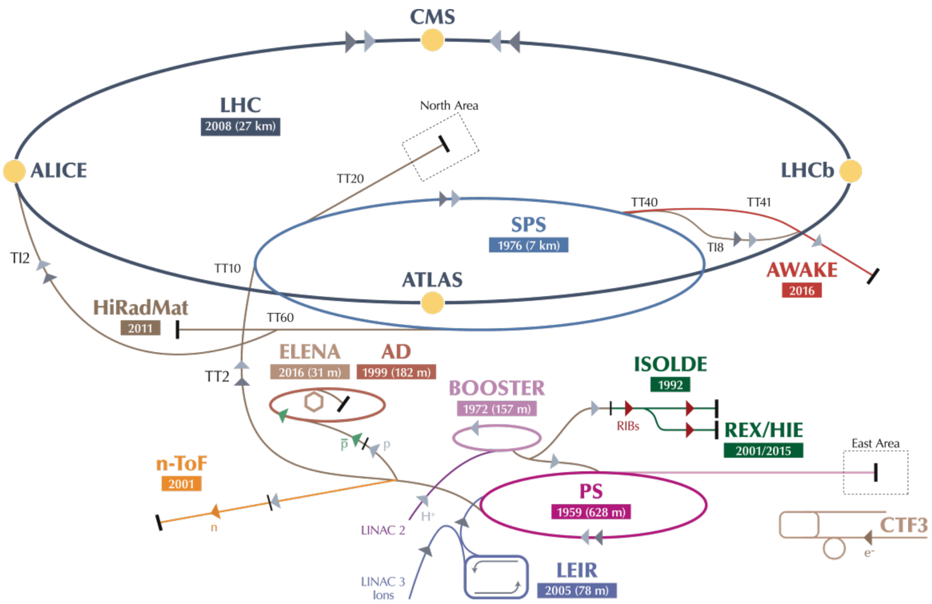

Figure 2.1: Schematic representation of the accelerator complex at CERN [56]. The LHC (dark blue) is the last element in chain of accelerators. Protons are successively accelerated by LINAC 2, the Booster, the Proton Synchrotron (PS) and the Super Proton Synchrotron (SPS) before entering the LHC.

In Figure 2.2 the LHC programme is shown. the first data collisions, so-called Run 1 period, lasted from 2008 until 16 February 2013 after which the CERN accelerator complex shut down for two years of planned maintenance and consolidation during so-called long shutdown 1 (LS1). On 23 March 2015, the new data taking period known as Run 2 started. With a brief end of the year extended technical stop (EYETS). The main activities carried out during the EYETS were the maintenance of many system such as the cryogenics, the cooling, electrical systems, etc.; the replacement of magnet, as well as a de-cabling and cabling campaign on the SPS. Run 2 will last until July 2018 when the long shut down 2 (LS2) will begin for 2 years. The main goal of this shutdown is the LHC injectors upgrade (LUI), but also maintenance and consolidation will be performed. Furthermore, preparations for the High Luminosity LHC,

[1] This energy loss is proportional to the fourth power of the proton energy and inversely proportional to the bending radius.

which will start in 2024, will be done. More information about phase 1 upgrades during LS1 and EYETS is given in Section 2.2.4.
Before the start of the LHC in 2010, the previous energy record was held by the Tevatron collider at Fermilab, colliding proton with antiprotons at $\sqrt{s} = 1.96$ TeV. When completely filled, the LHC nominally contains 2220 bunches in Run 2, compared to 1380 in Run 1 (design: 2200).

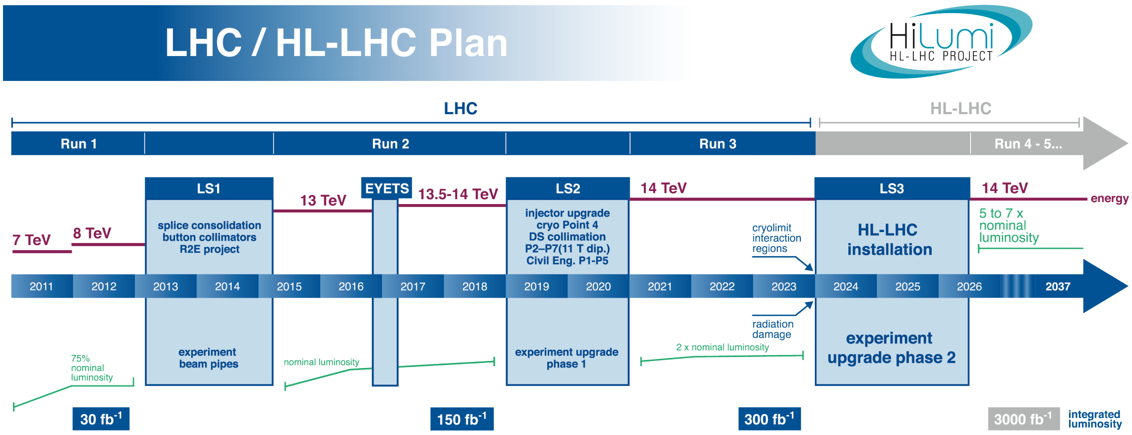

Figure 2.2: The HL-LHC timeline. Figure taken from [57].

Inside the LHC ring [58], the protons are accelerated by the means of radio frequency cavities, while 1232 dipole magnets of approximately 15 m long, each weighing 35 t ensure the deflection of the beams. The two proton beams circulate in opposite direction in separate pipes inside of the magnet. Through the use of a strong electric current in the coils of the magnet, magnetic fields are generated and cause the protons to bend in the required orbits. In order for the coil to become superconducting and able to produce a strong magnetic field of 8.3 T, the magnet structure is surrounded by a vessel. This vessel is filled with liquid Helium making it possible to cool down the magnet to 1.9 K. In order to get more focussed and stabilised proton beams, additional higher-order multipole and corrector magnets are placed along the LHC beam line.

The LHC is home to seven experiments, each located at an interaction point:

- A Toroidal LHC ApparatuS (ATLAS) [59] and the Compact Muon Solenoid (CMS) [60] experiments are the two general purpose detectors at the LHC. They both have a hermetic, cylindrical structure and were designed to search for new physics phenomena along with precision measurements of the Standard Model. The existence of two distinct experiments allows cross-confirmation of any discovery.
- A Large Ion Collider Experiment (ALICE) [61] and the LHC Beauty (LHCb) [62] experiments are focusing on specific phenomena. ALICE studies strongly interacting matter at extreme energy densities where a quark-gluon plasma forms in heavy ion collisions (Pb-Pb or p-Pb). LHCb searches for differences between matter and antimatter with the focus on b physics..

- The forward LHC (LHCf) [63] and the TOTal cross section, Elastic scattering and diffraction dissociation Measurement (TOTEM) [64] experiments are two smaller experiments that focus on head on collisions. LHCf consists of two parts placed before and after ATLAS and studies particles created at very small angles. TOTEM is placed in the same cavern as CMS and measures the total proton-proton cross section and studies elastic and diffractive scattering.
- The Monopoles and Exotics Detector At the LHC (MoEDAL) [65] experiment is situated near LHCb and tries to find magnetic monopoles.

For the enhancement of the exploration of rare events and thus enhancing the number of collisions, high beam energies as well as high beam intensities are required. The luminosity [66] is a measurement of the number of collisions that can be produced in a detector per square meter and per second and is the key role player in this enhancement. The LHC collisions create a number of events per second given by

$$N_{\text{event}} = L\sigma_{\text{event}}, \tag{2.1}$$

where σ_{event} is the cross section of the process of interest and L the machine instantaneous luminosity. This luminosity depends only on the beam parameters and is for a Gaussian beam expressed as

$$L = \frac{1}{4\pi} N_{\text{b}} n_{\text{b}} f_{rev} \frac{N_{\text{b}}}{\epsilon_n} \left(1 + \left(\frac{\theta_c \sigma_z}{2\sigma^*}\right)^2\right)^{\frac{-1}{2}} \frac{\gamma_{\text{r}}}{\beta^*}. \tag{2.2}$$

The number of particles per bunch is expressed by N_{b}, while n_{b} is the number of bunches per beam, f_{rev} the revolution frequency, γ_{r} the relativistic gamma factor, ϵ_n the normalized transverse beam emittance - a quality for the confinement of the beam , β^* the beta function at the collision point - a measurement for the width of the beam, θ_c the angle between two beams at the interaction point, σ_{z} the mean length of one bunch, and σ^* the mean height of one bunch. In Equation 2.2, the blue part represents the stream of particles, the red part the brilliance, and the green part the geometric reduction factor due to the crossing angle at the interaction point.

The peak design luminosity for the LHC is $10^{34}\,\text{cm}^{-2}\text{s}^{-1}$, which leads to about 1 billion proton interactions per second. In 2016, the LHC was around 10% above this design luminosity [67]. The luminosity is not a constant in time since it diminishes due to collisions between the beams, and the interaction of the protons and the particle gas that is trapped in the centre of the vacuum tubes due to the magnetic field. The diffusion of the beam degrades the emittance and therefore also the luminosity. For this reason, the mean lifetime of a beam inside the LHC is around 15 h. The integrated luminosity - the luminosity provided in a certain time range - recorded by CMS and ATLAS over the year 2016 is given in Figure 2.3. In Run 2, the peak luminosity is 13-17$\times 10^{33}$ cm^{-2}s^{-1} compared to 7.7$\times 10^{33}$ cm^{-2}s^{-1} in Run 1. The recorded luminosity is validated for physics analysis keeping 35.9 fb^{-1} during 2016 data taking.

Multiple proton-proton interactions can occur during one bunch crossing, referred to as pileup. On average, the number of pileup events is proportional to the luminosity times the total inelastic proton-proton cross section. In 2016, an average of about 27 of pileup interactions has been observed in 13 TeV proton collisions at the interaction point of CMS. For 2012, this number was about 21 pileup interactions for 8 TeV collisions.

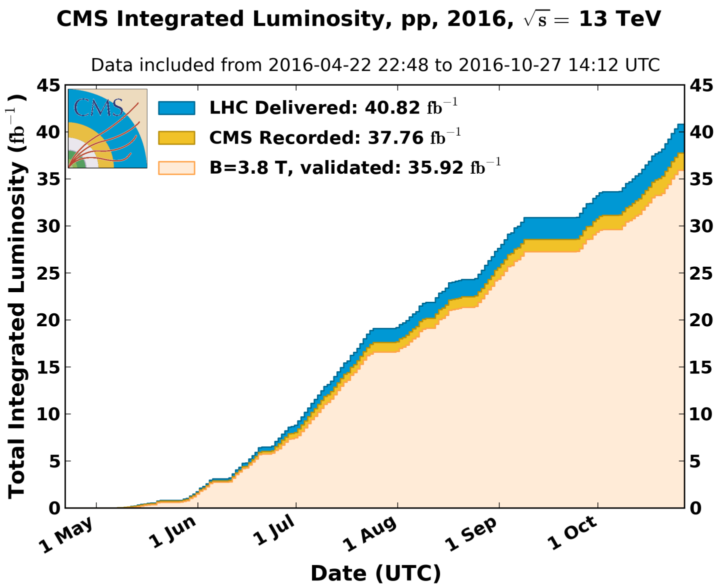

Figure 2.3: Cumulative off-line luminosity measured versus day delivered by the LHC (blue), and recorded by CMS (orange), and certified as good physics analysis during stable beams (light orange) during stable beams and for proton collisions at 13 TeV centre-of-mass energy in 2016. [68].

2.2 The Compact Muon Solenoid

At one of the collision points of the LHC, the CMS detector [69–71] is placed. Weighing 14 000 t, this cylindrical detector is about 28.7 m long and 15 m in diameter. It has an onion like structure of several specialised detectors and contains a superconducting solenoid with a magnetic field of 3.8 T. Living in a hadronic environment, multi-jet processes produced by the strong interaction are the main source of background for rare physics processes. Therefore, good identification, momentum resolution, and charge determination of muons, electrons and photons are one of the main goals of the CMS detector. Additionally, a good charged particle momentum resolution and reconstruction efficiency in the inner tracker provides identification for jets coming from b quarks or tau particles. Also the electromagnetic resolution for an efficient photon and lepton isolation as well as a good hadronic calorimeter for the missing transverse energy[2] were kept into account while designing CMS. In Figure 2.4, an overview of the CMS detector is shown.

2.2.1 CMS coordinate system

The coordinate system used by CMS can be found in Figure 2.5. The origin of the right handed orthogonal coordinate system is chosen to be the point of collisions. The x-axis points towards the centre of the LHC ring such that the y-axis points towards the sky, and the z-axis lies tangent to the beam axis. Since the experiment has a cylindrical shape, customary coordinates are used to describe the momentum $\vec{p}$: the distance $p = |\vec{p}|$, the azimuthal angle[3] $\phi \in [-\pi, \pi]$, the

[2]The missing transverse energy comes from an imbalance in the transverse plane. This will be discussed in Chapter 4.

[3]The azimuthal angle is the angle between the x-axis and the projection in the transverse plane of the momentum $\vec{p}$, denoted as $\vec{p}_T$.

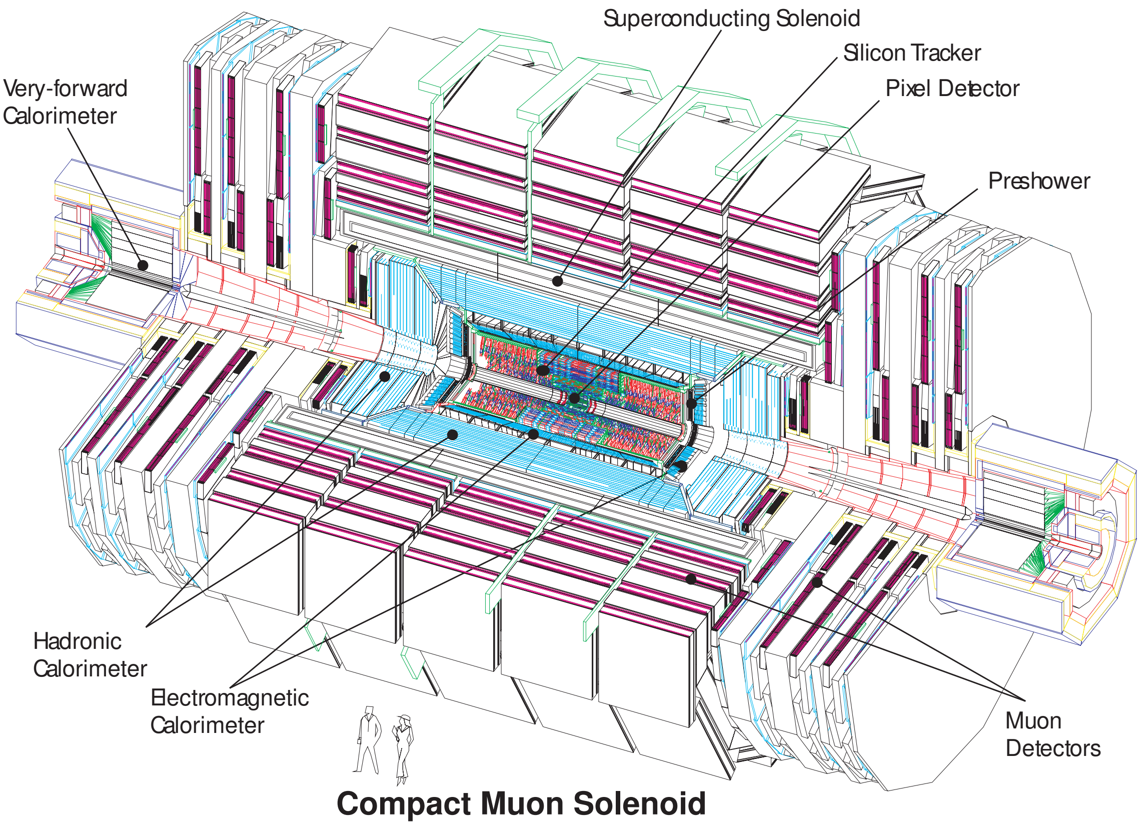

Figure 2.4: Mechanical layout of the CMS detector. Figure taken from [72].

pseudo-rapidity[4] η :

$$\eta = -\ln\left(\tan\left(\frac{\theta}{2}\right)\right). \tag{2.3}$$

For the energies considered at the LHC, where $E >> m$, the pseudo-rapidity is a good approximation of the rapidity y

$$y = \frac{1}{2}\ln\left(\frac{E+p_z}{E-p_z}\right), \tag{2.4}$$

where the difference of rapidities of two particles is invariant under a Lorentz boost in the z-direction.

2.2.2 Towards the heart of CMS

The CMS detector can be divided into two parts. A central barrel is placed around the beam pipe $\left(|\eta| < 1.4\right)$, and two plugs (endcaps) ensure the hermeticity of the detector. In Figure 2.4 and Figure 2.6 the onion like structure of the CMS detector is visible. The choice of a solenoid of 12.9 m long and 5.9 m diameter gives the advantage of bending the particle trajectories in the

[4]The pseudo rapidity is expressed by the polar angle θ between the direction of $\vec{p}$ and the beam.

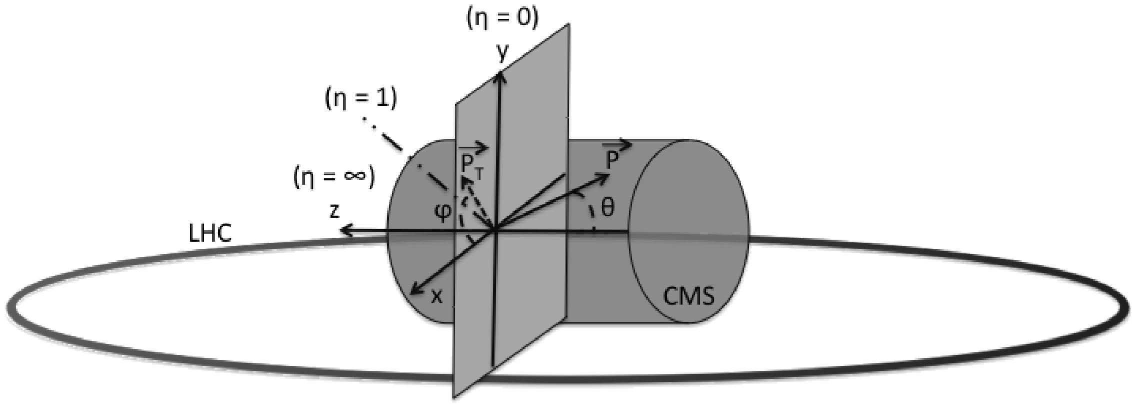

Figure 2.5: Representation of the coordinate system used by CMS. The point of origin is put at the collision point. The x-axis points towards the centre of the LHC ring such that the z-axis lies tangent to the beam axis.

transverse plane. The hadronic calorimeter (Section 2.2.2.3), the electromagnetic calorimeter (Section 2.2.2.4) and the tracker (Section 2.2.2.5) are within the solenoid (Section 2.2.2.2), while the muon chambers (Section 2.2.2.1) are placed outside the solenoid. The data used for the search presented in this thesis is collected after the long shutdown 1. After discussing each part of CMS in their Run 1 configuration, Section 2.2.4 elaborates on their different upgrades for the data collected in Run 2.

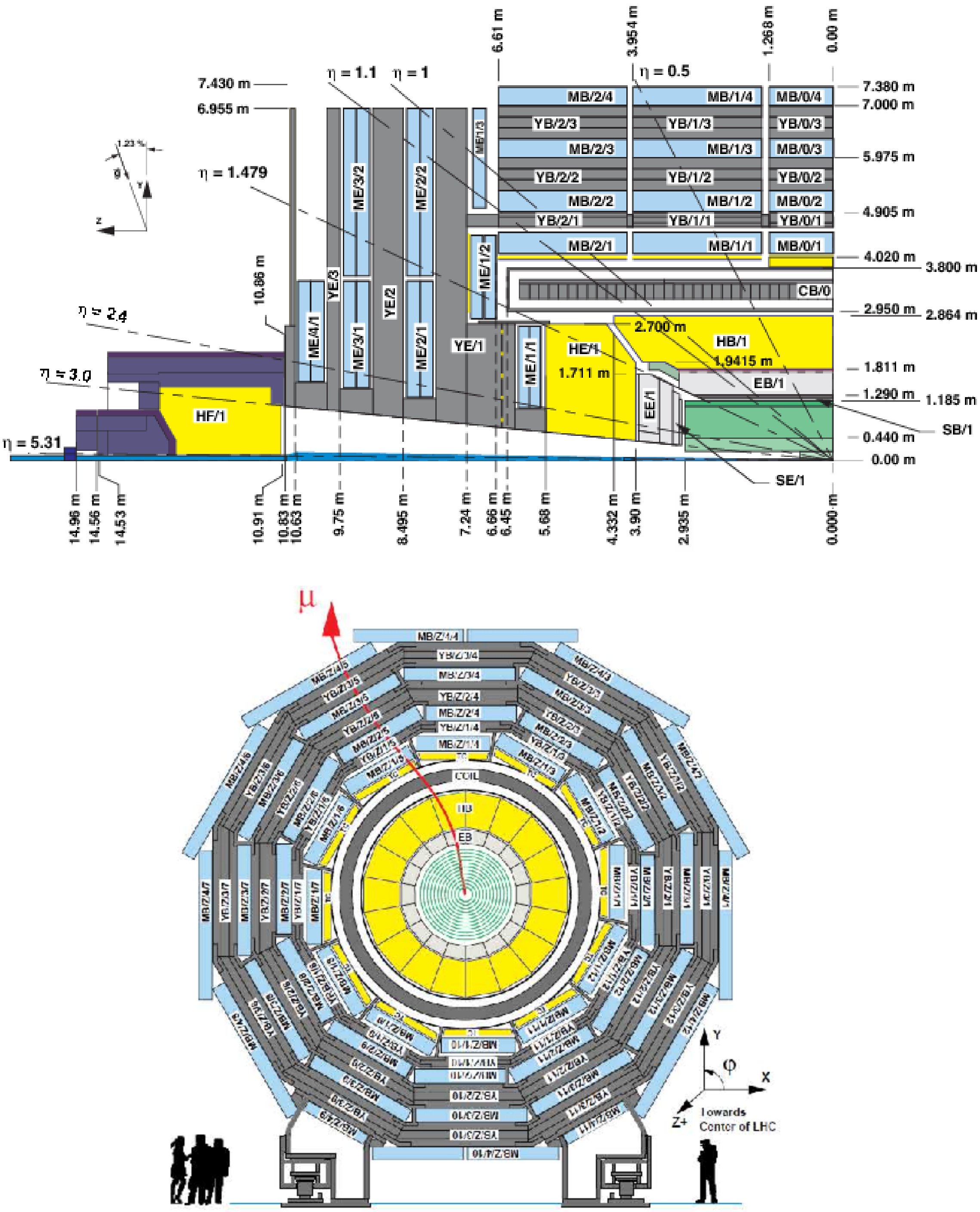

Figure 2.6: Schematic view of the CMS detector in the Run 1 configuration. The longitudinal view of one quarter of the detector is given at the top, while the transversal view is shown at the bottom. The muon system barrel elements are denoted as MBZ/N/S, where Z= −2... + 2 is the barrel wheel number, N= 1...4 the station number and S= 1...12 the sector number. Similary, the steel return yokes are denoted as YBZ/N/S. The solenoid is denoted as CB0, while the hadronic calorimeter is denoted as HE (endcap)/ HB (barrel)/HF (forward) and the electromagnet calorimeter as EE (endcap)/EB (barrel). The green part represents the tracking system (tracker + pixel). Figure taken from [73].

2.2.2.1 Muon system

The outermost part of CMS consists of the muon system. The magnet return yoke is interleaved with gaseous detector chambers for muon identification and momentum measurement. The barrel contains muon stations arranged in five separate iron wheels, while in the endcap four muon stations are mounted onto three independent iron discs on each side. Each barrel wheel has 12 sectors in the azimuthal angle.

The muon system is divided into three parts, shown in Figure 2.7. The muon rate and neutron induced backgrounds are small and the magnetic field is very low for the barrel, thus CMS can use drift tube (DT) chambers. For the endcaps however, the muon and background flux is much higher and there is a need to use cathode strip chambers (CSC) which are able to provide a faster response, higher granularity and have a better resistance against radiation. In order to form a redundant trigger system, resistive plate chambers (RPC) are added. This makes a total of 250 DT, 540 CSC and 610 RPC chambers. In Figure 2.6 the arrangement is shown.

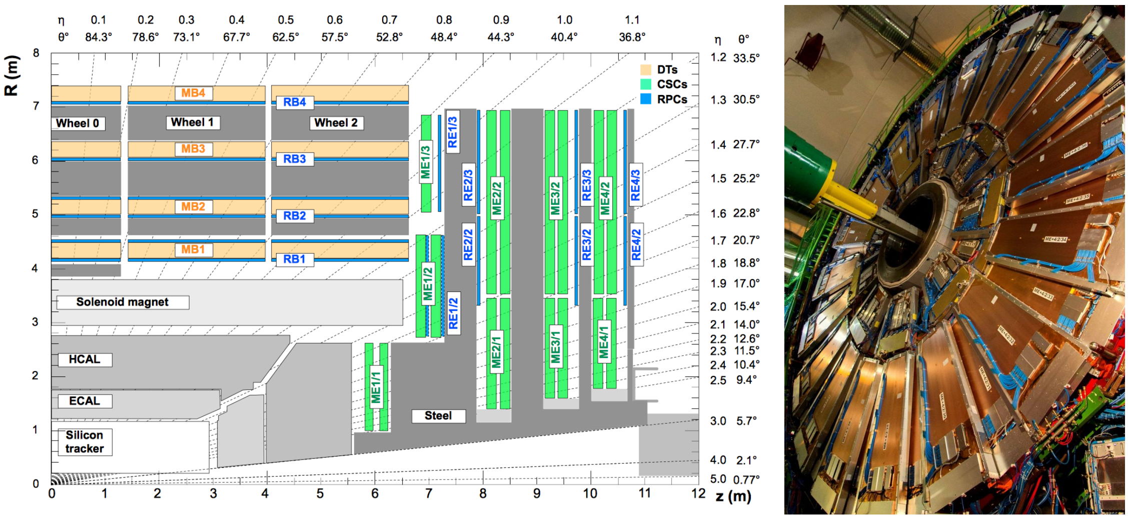

Figure 2.7: (Left) Schematic view of one quarter of the CMS muon system in the Run 1 configuration. The cathode strip chambers (CSC) are shown in green, the drift tubes (DT) are shown in yellow, while the resistive plate chambers (RPC) are shown in blue. Figure taken from [73]. (Right) Cathode strip chambers (ME+4/2 chambers on YE+3). Photo taken from [74].

Providing a measurement for $|\eta| < 1.2$, the DT chambers in the barrel are on average $2 \times 2.5\ \mathrm{m}^2$ in size and consist of 12 layers of DT cells[5] arranged in three groups of four. The $r\phi$ coordinate is provided by the two outside groups, while the middle group measures the z coordinate. For the outer muon station, the DT chambers contain only 8 layers of DT cells, providing a muon position in th $r\phi$ plane. There are four CSC stations in each endcap, providing muon measurements for $0.9 < |\eta| < 2.4$ (Run 1 configuration). These CSCs are multi-wired proportional chambers that consist of 6 anode wire planes crossed by 7 copper strips cathode panels in a gas volume. The r coordinate is provided by the copper strips, while the ϕ coordinate comes from the anode wires, giving a two dimensional position measurement. There are six

[5]The DT cells are 4 cm wide gas tubes with positively charged stretched wires inside.

layers of RPCs in the barrel muon system and one layer into each of the first three stations of the endcap. They are made from two high resistive plastic plates with an applied voltage and separated by a gas volume. Read out strips mounted on top of the plastic plates detect the signal generated by a muon passing through the gas volume. The RPCs provide a fast response with a time resolution of 1 ns and cover a range of $|\eta| < 1.8$ for the Run 1 configuration.

The muon system provides triggering on muons, identifying muons and improves the momentum measurement and charge determination of high p_T muons. On top of the muon system, a fraction of the muon energy is deposited in the electromagnetic calorimeter, the hadronic calorimeter, and outer calorimeter. The high magnetic field enables an efficient first level trigger and allows a good momentum resolution of $\Delta p/p \approx 1\%$ for a p_T of 100 GeV and $\approx 10\%$ for a p_T of 1 TeV. There is an efficient muon measurement up to $|\eta| < 2.4$.

NOTE: check numbers for Run 2

2.2.2.2 Solenoid

Making use of the knowledge of previous experiments like ALEPH and DELPHI at LEP and H1 at HERA, CMS choose for a large super conducting solenoid with a a length of 12.9 m and a inner bore of 5.9 m [71]. With 2 168 turns, a current of 18.5 kA resulting in a magnetic field of 3.8 T, and a total energy of 2.7 GJ, a large bending power can be obtained for a modestly-sized solenoid. In order to ensure a good momentum resolution in the forward regions, a favourable length/radius was necessary. In Figure 2.8, a photo of the CMS solenoid is shown.

The solenoid uses a high-purity aluminium stabilised conductor with indirect cooling from liquid helium, together with fully epoxy impregnation. A four-layer winding is implemented that can withstand an outward pressure of 64 atm. The NbTi cable is co-extruded by pure aluminium that acts as a thermal stabilizer and has an aluminium alloy for mechanical reinforcement. The return of the magnetic field is done by fives wheels, noted by YB in Figure 2.6.

2.2.2.3 Hadronic calorimeter

The hadronic calorimeter (HCAL) is dedicated to precisely measure the energy of charged and neutral hadrons via a succession of absorbers and scintillators. This makes it crucial for physics analyses with hadronic jets or missing transverse energy. The HCAL barrel extends between $1.77 < r < 2.95$ m, where r is the radius in the transverse plane with respect to the beam. Due to space limitations, the HCAL needs to be as small as possible and is made from materials with short interaction lengths[6]. On top of this, the HCAL should be as hermetic as possible and extend to large absolute pseudo rapidities such that it can proved a good measurement of the missing transverse energy.

The quality of the energy measurements is dependent on the fraction of the hadronic shower that can be detected. Therefore, the HCAL barrel (HB) inside the solenoid is reinforced by an outer hadronic calorimeter between the solenoid and muon detectors (HO, see Figure 2.9), using the solenoid as extra absorber. This increases the thickness to 12 interaction lengths. The HB

[6]Here the interaction length is the nuclear interaction length and this is the length needed for absorbing 36.7% of the relativistic charged particles. For the electromagnetic calorimeter this is defined in radiation length X_0. The radiation length is the mean distance over which a high energy electron loses all but $1/e$ of its energy by bremsstrahlung.

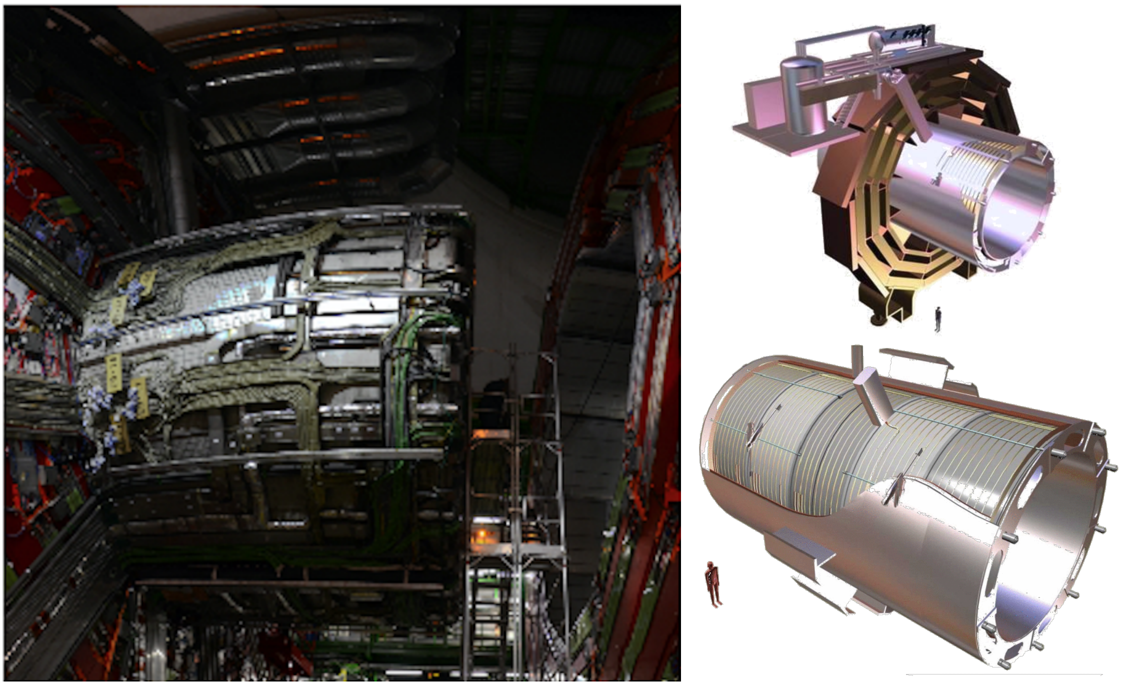

Figure 2.8: (Left) CMS solenoid during the long shutdown in 2013. (Right) An impression of the solenoid magnet taken from [75].

and HO provide measurements for $|\eta| < 1.3$, while an endcap on each side (HE, $1.3 < |\eta| < 3$) and a forward calorimeter (HF, $3.0 < |\eta| < 5.2$) extend the pseudo rapidity range.

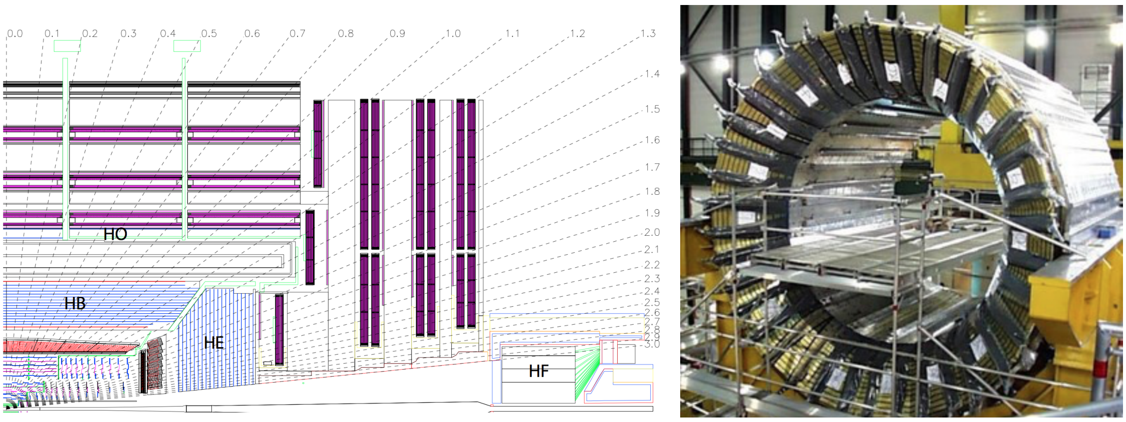

Figure 2.9: (Left) Longitudinal view of the CMS detector showing the locations of the HB, HE, HO, and HF calorimeters. Figure taken from [60]. (Right) CMS barrel calorimeter. Photo taken from [76].

The HB is made of 16 absorber plates where most of them are built from brass and others are made from stainless steal and is about five to ten interaction lengths thick. It is divided in $\eta \times \phi$ towers and contains 2592 read out channels. The HO complements the HB and extends the reach up to twelve interaction lengths. This subsystem contains 2160 read out channels. The HE is also composed of brass absorber plates and has a thickness corresponding to approximately ten interaction lengths, with 2592 read out channels.. The HF experiences intense particle fluxes with an expected energy of 760 GeV deposited on average in a proton interaction at a centre-of-mass of 14 TeV, compared to 100 GeV in the rest of the detector. Therefore, these are Cherenkov light detectors made of radiation hard quartz fibres. The main causes of such large energy events are high energy muons and charged particles from late showering hadrons. During Run 1, it became clear that the glass windows of the photon multiplier tubes (PMTs) had to be replaced which was done during LS1 [77]. The HF represents 1728 read out channels.

The HCAL and electromagnetic calorimeter combined can measure the hadron energy with a resolution $\Delta E/E \approx 100\%\sqrt{E[\mathrm{GeV}]} + 5\%$.

2.2.2.4 Electromagnetic calorimeter

The electromagnetic calorimeter (ECAL) is designed to measure the energy of photons and electrons and covers $|\eta| < 3$. It is an hermetic, homogeneous detector and consists of 75 848 lead tungstate ($PbWO_4$) crystals. These crystals have a fast response time - 80% of the light is emitted within 25 ns - and are radiation hard. The electromagnetic showers produced by passing electrons or photons ionize the crystal atoms which emit a blue-green scintillation light, that is collected by silicon avalanche photodiodes (APDs) in the barrel and vacuum phototriodes (VPTs) in the endcaps. The crystals and the APD response is sensitive to temperature changes and require a stable temperature.

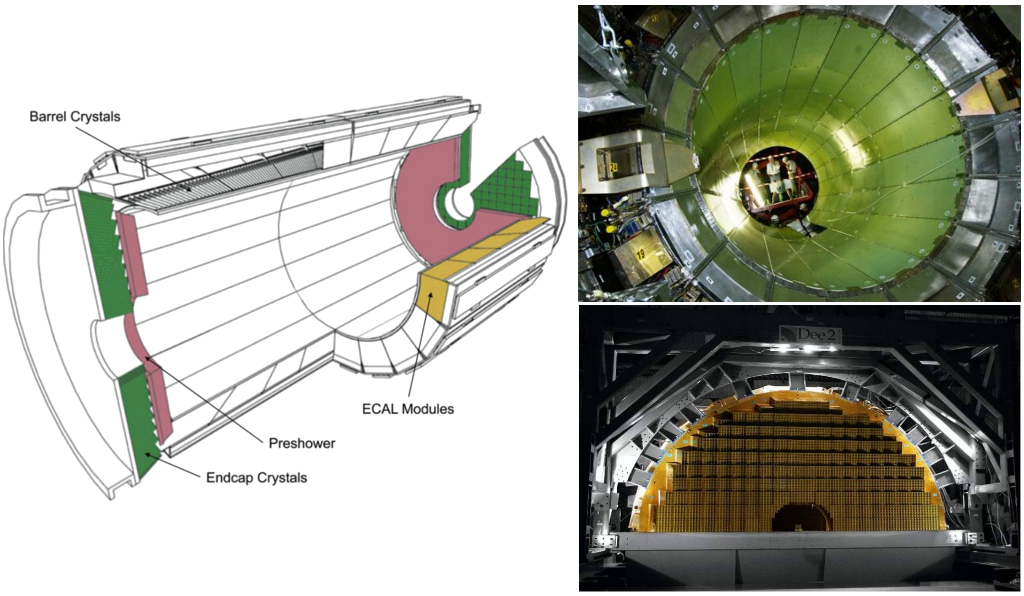

Figure 2.10: (Left) Schematic cross section of the electromagnetic calorimeter taken from [60]. (Right top) The ECAL barrel during construction [78]. (Right bottom) One half of an EE [79].

There are three parts: a central barrel (EB), an endcap region (EE) and a preshower (ES) (Figure 2.10). The EB has an inner radius of 129 cm and corresponds to a pseudo rapidity of $0 < |\eta| < 1.479$. At a distance of 314 cm from the vertex and covering a pseudo rapidity of $1.479 < |\eta| < 3.0$, are the EE. They consist of semi-circular aluminium plates from which structural units of 5×5 crystals (super crystals) are supported. The ES is placed in front of the crystal calorimeter over the endcap pseudo rapidity range with two planes of silicon strip detectors as active elements.

The electromagnetic shower will typically involve more than one channel. More than 90% of the energy of a 35 GeV electron or photon is contained in a 5×5 matrix of crystals. Therefore, a clustering algorithm is performed in order to associate the energy deposits to the particles impinging the calorimeter. The achieved precision [80] for the barrel is $2{\times}10^{-3}$ rad in ϕ and 10^{-3} in η . For the endcaps this is $5{\times}10^{-3}$ rad in ϕ and $2{\times}10^{-3}$ in η . The energy is reconstructed by a supercluster algorithm, taking into account energy radiated via bremsstrahlung or conversion [60]. The energy resolution is given by

$$\frac{\sigma(E)}{E} = \frac{2.8\%}{\sqrt{E}} \oplus \frac{0.128}{E(GeV)} \oplus 0.3\%, \tag{2.5}$$

in the absence of a magnetic field, where the contributions come from the stochastic, noise and constant terms respectively. The dominating term is the constant term ($E_{shower} \approx 100$ GeV) and thus the performance is highly dependent on the quality of calibration and monitoring .

2.2.2.5 Inner tracking system and operations

The tracking system (tracker) [81] is the detecting unit closest to the point of interaction. Responsible for the reconstruction of trajectories from charged particles with $|\eta| < 2.5$ that are bent by the magnetic field, it provides a measurement of the momentum. The tracker is also responsible for the determination of the interaction point or vertex. It should be able to provide high granularity as well as fast read out, and be able to endure high radiation. For these reasons, the CMS collaboration choose silicon detector technology.

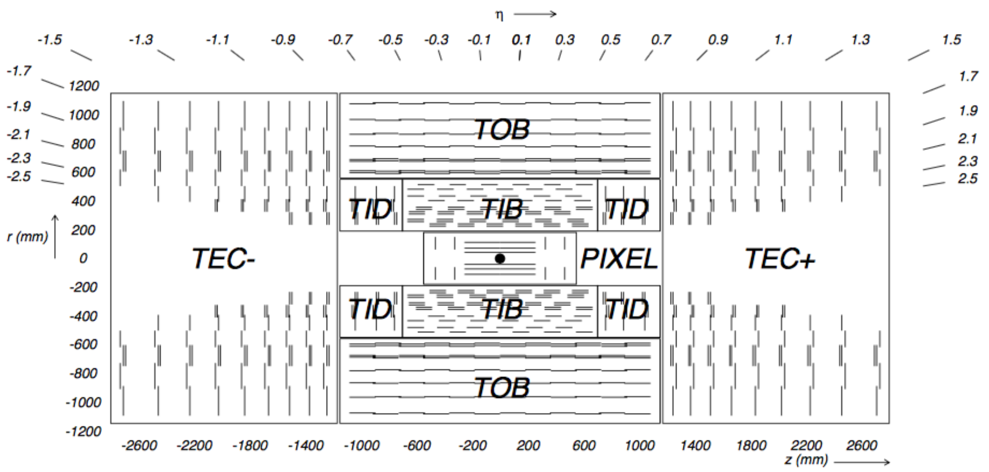

Figure 2.11: Schematic cross section through the CMS tracker. Each line represents a detector module. Double lines indicate back-to-back modules that deliver stereo hits. Figure taken from [60].

The tracking system consists of a cylinder of 5.8 m long and 2.5 m in diameter. It is immersed in a co-axial magnetic field of 3.8 T provided by the solenoid. As shown in Figure 2.11, the tracker is built up from a large silicon strip tracker with a small silicon pixel tracker inside. The inner pixel region ($4.4 < r < 10.2$ cm), gets the highest flux of particles. Therefore, pixel silicon sensors of 100×150 μm^2 are used. It consists of three cylindrical barrels that are complemented by two discs of pixel modules at each side. The silicon strip tracker ($20 < r < 116$cm) has three subdivisions. The Tracker Inner Barrel and Discs (TIB, TID, see Figure 2.13) are composed of four barrel layers accompanied by three discs at each end. The outer part of the tracker - Tracker Outer Barrel (TOB) - consists of 6 barrel layers. In the outer discs, there are nine discs of silicon sensors, referred to as Tracker End Caps (TEC).

Figure 2.12: The pixel barrel being re-installed after the Long Shutdown in 2015, around the beam pipe at CMS [82].

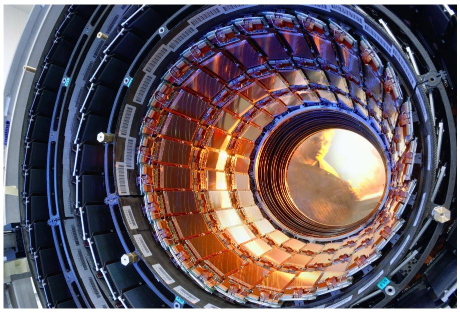

Figure 2.13: First half of the inner tracker barrel, consisting of three layers of silicon modules [83].

The pixel detector, shown in Figure 2.12, has 1440 modules that cover an area of about 1 m^2 and have 66 million pixels. It provides a three-dimensional position measurement of the hits arising from the interaction from charged particles with the sensors. In transverse coordinate ($r\phi$), the hit position resolution is about 10 μm, while 20-40 μm is obtained in the longitudinal coordinate (z). The sensor plane position provides the third coordinate. The TIB/TID, shown in Figure 2.13, delivers up to four $r\phi$-measurements using 320 μm thick silicon micro-strip sensors. These sensors are placed with their strips parallel to the beam axis in the barrel and radial in the discs. In the TIB, the first two layers have a strip pitch of 80μm, while the remaining two have a strip pitch of 120 μm. This leads to a respective single point resolution of 23 μm and 35 μm. For the TID, the pitch varies between 100 μm and 141 μm. The TOB provides six $r\phi$-measurements with a single point resolutions of 53 μm in the first four layers, and 35 μm in the last two layers. It consists of 500 μm thick microstrip sensors with strip pitches of 183 μm (first 4 layers) or 122 μm (last two layers). The TEC provides up to 9 ϕ-measurements via 9 discs consisting of up to 7 rings of silicon microstrip sensors of 97 μmto 184 μm average pitch.

A second co-ordinate measurement (z in the barrel, r on the discs) is provided through the use of a second micro strip detector module mounted back-to-back with a stereo angle of 100 mrad. This is done on the modules in the first two layers and rigns of the TIB, TID, and TOB, as wel as rigns 1,2, and 5 of the TECs (blue line in Figure 2.11). The resolution in the z direction is approximately 230 μm in the TIB and 530 μm in the TOB, and is varying with pitch in the TID and TEC. To allow overlay and avoid gaps in acceptance, each module is shifted slightly in r or z with respect to its neighbouring modules within a layer. With this detector lay out, at least nine points per charged particle trajectory can be measured in an $|\eta|$ range up to 2.4, where at least four of them being two dimensional. The CMS silicon tracker provides 9.3 million readout channels and covers an active area of about 198 m^2.

2.2.3 Data acquisition

At a design luminosity of 10^{34} cm^{-2}s^{-1}, the proton interaction rate exceeds 1 GHz. Given the large size of an event (about 1 MB), the high crossing rate, and that typically tens of collisions happen at the same time, it is impossible for the CMS experiment to store all the data generated. In order to deal with the large amount of data, a two level trigger system has been put in place. The first level (Level-1) is a custom hardware system, while a second high level trigger (HLT) is software based running on a large farm of computers.

CMS Level-1 Trigger

The Level-1 Trigger has to be a flexible, maintainable system, capable of adapting to the evolving physics programme of CMS [84]. Its output rate is restricted to 100 kHz imposed by the CMS readout electronics. It is implemented by custom hardware and selects events containing candidate objects - e.g. ionization deposits consistent with a muon, or energy clusters corresponding to an electron / photon / tau lepton / missing transverse energy / jet. Collisions with large momenta can be selected by using scalar sum of the transverse momenta of the jets.

By buffering the raw data from the CMS subdetectors in front-end drivers, the Level-1 Trigger has a pipeline memory of 3.2 μs to decide whether to keep an event or reject it. The trigger primitives (TP) from the calorimeters and muon detectors are processed in several steps and combined into a global trigger. This information is then combined with the input from the other subsystems for the HLT. The separate inputs are synchronized to each other and the LHC orbit clock and sent to the global trigger module. Here, Level-1 Trigger algorithms are performed within 1 μs to decide whether to keep the event.

CMS HLT Trigger

The HLT is an array of commercially available computers with a programmable menu that has an output rate of on average 400 Hz for off-line event storage. The data processing is based on an HLT path. This is a set of algorithmic steps to reconstruct objects to define selection criteria. Here, the information of all subdetectors can be used to perform algorithms on higher level reconstructed objects.

2.2.4 Phase 1 upgrades

Before the start of taking collision data for 13 TeV operations on 3 June 2015, CMS had a long shutdown (LS1) [85]. During this shutdown, the section of the beryllium beam pipe within CMS was replaced by a narrower one. This operation required the pixel detector to be removed and reinserted into CMS. During Run 2, higher particle fluxes with respect to Run 1 are expected. To avoid longterm damage caused by the intense particle flux at the heart of CMS, the tracker is been made ready to operate at much lower temperature than during Run 1. The electromagnetic calorimeter preshower system was damaged during Run 1, therefore the preshower discs were removed, repaired and reinstalled successfully inside CMS in 2014. To help the discrimination between interesting low momentum muons coming from collisions and muons caused by backgrounds, a fourth triggering and measurement station for muons was added in each of the endcaps. Several new detectors were installed into CMS for measuring the collision rate within the detector and to monitor beam related backgrounds.

During the LS1, the muon system underwent major upgrades [86, 87]. In the fourth station of each endcap, the outermost rings of CSC and RPC chambers were completed, providing an angular coverage of $1.2 < |\eta| < 1.8$ for Run 2, increasing the system redundancy, and allowing tighter cuts on the trigger quality. In order to reduce the environmental noise, outer yoke discs have been placed on both sides for the endcaps. At the innermost rings of the first station, the CSCs have been upgraded by refurbishing the readout electronics to make use of the full detector granularity instead of groups of three as was the case for Run 1. In Figure 2.7 (right), the refurbishing of the CSCs is shown.

Since the HF experiences intense particle fluxes, it became clear during Run 1 that the glass windows of the PMTs need replacing. For the ECAL in Run 1, the energy reconstruction happened via a weighted sum of the digitized samples [88]. For Run 2 however, the reconstruction had to be made more resistant for out of time pile up and a multi-fit approach has been set into place. In this approach, the pulse shape is modelled as a sum of one in-time pulse plus the out of time pulses [80]. The energy resolution is better than 2% in the central barrel region and 2-5 % elsewhere.

During the first data taking period of the LHC (2010 to 2013), the tracker operated at +4°C. With the higher LHC beam intensities from 2015 onwards, the tracker needs to be operated at much lower temperatures. The reason for this is that with intense irradiation, the doping concentration changes, the leakage current increases proportional to the fluence and the charge collection efficiency decreases due to charge trapping. Mostly the leakage current (I) is affected by the temperature change:

$$I \propto T^2 e^{-\frac{E_g}{2kT}}, \tag{2.6}$$

where T is the operating temperature, E_g the band gap and k the Boltzmann constant. There is approximately a factor 15 between the leakage currents at room temperatures and at −10 °C.

During the LS1, the CMS cooling plant was refurbished [89] and the fluorocarbon cooling system overhauled. To help to suppress the humidity inside the tracker, new methods for vapour sealing and insulation were applied. Furthermore, several hundred high-precision sensors are used to monitor the humidity and temperature. In order to get as dry air as possible, a new dry-gas plant provides eight times more dry gas (air or nitrogen) than during the first run, and allows regulation of the flow. As a final addition, the cooling bundles outside the tracker are equipped with heater wires and temperature sensors in order to maintain safe operations above the cavern dew point. For the data taking in 2015-2016, the tracker operated at −15°C.

In Run 2, with the increase in centre of mass energy and a higher luminosity, a larger number of simultaneous inelastic collisions per crossing is expected with respect to Run 1. For this, the CMS Level-1 has been upgraded [90]. All hardware, software, databases and the timing control system have been replaced for Run 2, where the main changes are that the muon system now uses the redundancy of the muon detector system earlier to make a high resolution muon trigger. Other upgrades are that the calorimeter system isn't bound any more for streaming data and the global trigger has more Level-1 Trigger algorithms.

After the first half of Run 2, the innermost part of detection in CMS (pixel detector) was replaced, enhancing the particle tracking capabilities of CMS. The data used in the framework of this thesis however is from before this upgrade. More information on the Pixel upgrade can be found in Refs. [91, 92].

2.2.5 CMS computing model

The selected data is stored, processed and dispersed via the Worldwide Large Hadron Collider Computing Grid (WLCG) [93, 94]. This has a tiered structure that functions as a single, coherent system.

At CERN and the Wigner Research Center for physics, a single Tier-0 is located. The raw data collected by the experiments is archived here, and a first reconstruction of the data is done. This data is then already in a file format usable for physics analysis. Furthermore, it is able to reprocess data when new calibrations become available. The Tier-0 site distributes this data to a total of 14 Tier-1 centres. They carry out data reprocessing and store real data as well as simulated data. The Tier-1 further distributes the data to over 150 Tier-2 centres. These make the data accessible for physics analysis and are also being used for the production of simulated data. The data is made accessible for physicists around the world. For CMS, the Tier-0 site at CERN reconstructs the full collision events and the backup of the data is send to seven Tier-1 computer centres: France, Germany, Italy, Spain, Taiwan, UK, and the US. At the Tier-1 sites the events are again reconstructed using refined calibration constants. The patterns are created and the more complex events are sent to forty Tier-2 centres for specific analysis task.

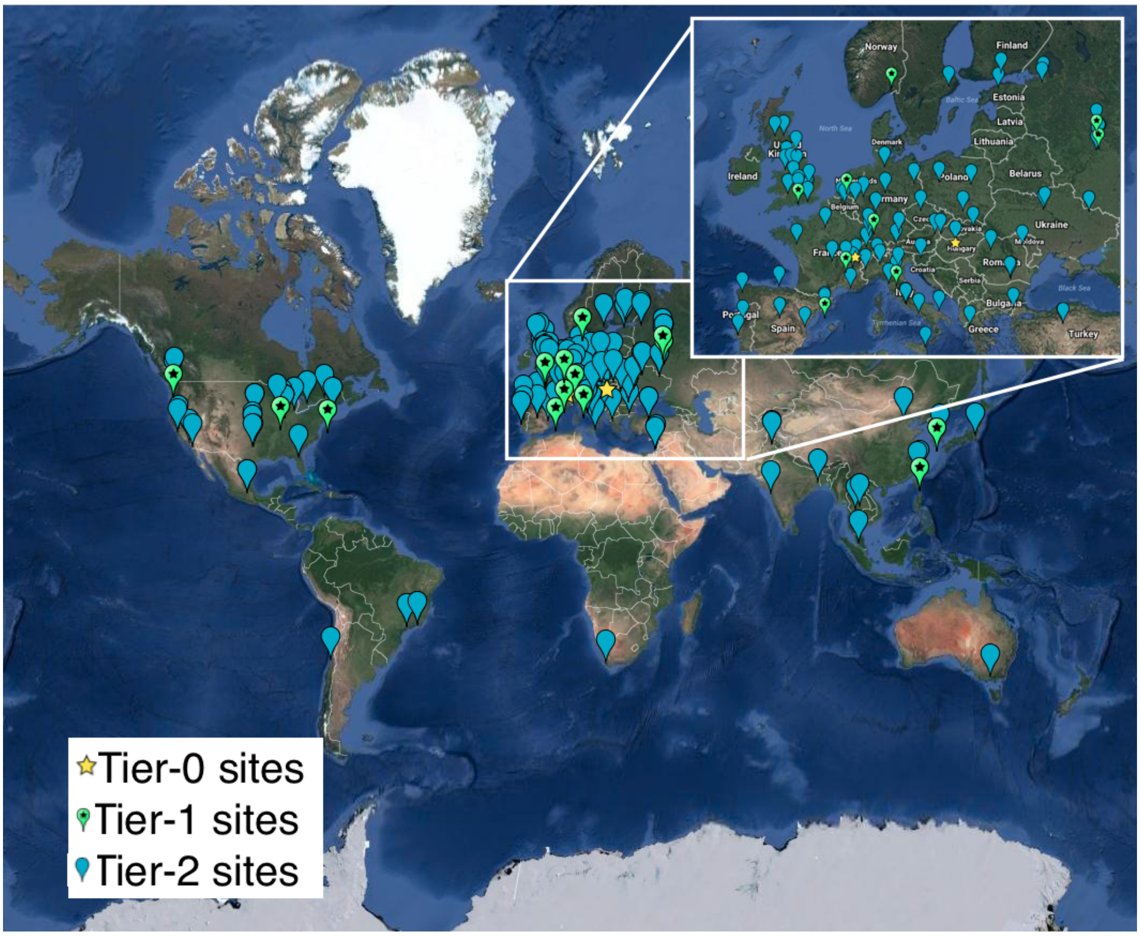

Figure 2.14: Worldwide LHC Computing Grid in 2017 [95].

Analysis techniques 3

In order to study the collisions coming from high energy experiments, many tools have been developed. In Section 3.1, the physics of hadron collision at high energies are presented. These insights are used to generate events via Monte Carlo event generators, explained in Section 3.2. Machine learning helps to differentiate between signal- and background like events. In Section 3.3, the multivariate technique of boosted decision trees is explained. This yields powerful discriminants for separating signal and background events and provides distributions for template-based maximum likelihood fits. The fitting method used in the search presented in this thesis is discussed in Section 3.4.

3.1 Hadron collisions at high energies

All partons can be approximated as free when there is sufficiently high momentum transfer in hadron collisions. The makes it possible to treat a hadron-hadron scattering as a single parton-parton interaction. The momentum of the parton can then be expressed as a fraction of the hadron momentum

$$\vec{p}_{\text{parton}} = x\vec{p}_{\text{hadron}}, \tag{3.1}$$

where x is referred to as the Björken scaling variable. The interaction $\mathrm{p_A p_B} \to \mathrm{X}$ can then be factorised in terms of partonic cross sections $\hat{\sigma}_{\mathrm{ij}\to\mathrm{X}}$ [96]

$$\sigma_{\mathrm{p_A p_B}\to\mathrm{X}} = \sum_{\mathrm{ij}} \iint dx_1 dx_2\, f_{\mathrm{i}}^{\mathrm{A}}(x_1, Q^2) f_{\mathrm{j}}^{\mathrm{B}}(x_2, Q^2) d\hat{\sigma}_{\mathrm{ij}\to\mathrm{X}}, \tag{3.2}$$

where i and j are the partons resolved from protons A and B. The parton density functions (PDF) are denoted as $f_{\mathrm{i}}(x_{\mathrm{j}}, Q^2)$, and Q^2 is the factorisation scale more commonly denoted as μ_{F}. This factorisation scale represents the energy at which the hadronic interaction can be expressed as a product of the partonic cross section and the process independent PDF. In Figure 3.1, the kinematic regions in x and μ_{F} are shown for fixed target and collider experiments.

The parton density functions (PDF) [97–99] represent the momentum distribution of the proton amongst its partons at an energy scale μ_{F}. These functions are obtained from gloabl fits to data since the can not be determined from first principles. From measurements on deep

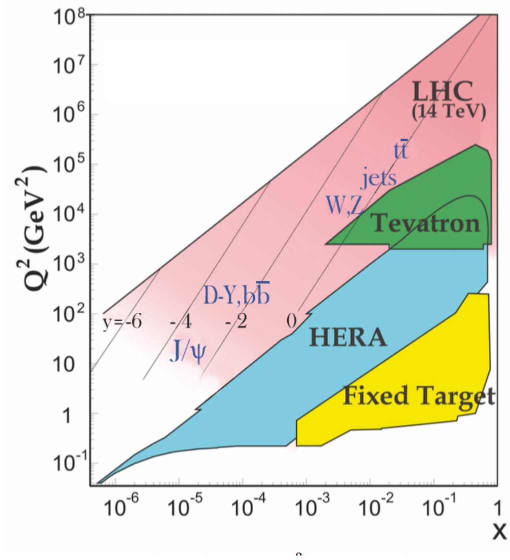

Figure 3.1: Kinematic regions in momentum fraction x and factorisation scale Q^2 probed by fixed-target and collider experiments. Some of the final states accessible at the LHC are indicated in the appropriate regions, where y is the rapidity. In this figure, the incoming partons have $x_{1,2} = (M/14\text{TeV})e^{\pm y}$ with $Q = M$ where M is the mass of the state shown in blue in the figure. For example, exclusive J/ψ and ϒ production at high $|y|$ at the LHC may probe the gluon PDF down to $x \sim 10^{-5}$. Figure taken from [6].

inelastic scattering using lepton-proton collision by the HERA collider [100], supplemented with proton-antiproton collisions from the Tevatron [101], and proton collision data from the ATLAS, CMS and LHCb collaborations at the LHC (Run 1) [102] the PDFs are determined and included in global PDF sets known as the PDF4LHC recommendation [99]. Their measurement at scale μ_F is extrapolated to higher energies by use of the DGLAP equations [103]. Once these PDFs are known, the cross section of a certain process can be calculated and used as input for the Monte Carlo generators used to make the simulated data samples at the LHC. In the framework of this thesis, the NLO PDF4LHC15_100 set is used. This set is an envelope of three sets: CT14, MMHT2014 and NNPDF3.0 [99]. As illustration, the dependency of the PDFs on the momentum fraction x is shown for the NNPDF3.0 set on hadronic scale $\mu_F^2 = 10\text{GeV}^2$ and LHC scale $\mu_F^2 = 10^4\text{GeV}^2$ in Figure 3.2. The gluon density dominated for most values of the momentum fraction, implying that it is easier to probe gluons than the quarks. When the Björken scale is to one, the parton densities of the valence quarks of the proton, up and down quarks,dominate over the gluon density. The sea quarks originating from gluon splitting, the charm, anti-up, and anti-down quarks, have lower densities in general for the proton. The resolution scale Q^2 is typically taken to be the energy scale of the collision. For the top quark pair production a scale of $Q^2 = (350\,\text{GeV})^2$ is chosen, meaning that the centre-of-mass energy of the hard interaction is about twice the top quark mass. The uncertainty on the parton distributions is evaluated using the Hessian technique [104], where a matrix with a dimension identical to the number of free parameters needs to be diagonalised. In the case of PDF4LHC15_100 set, this translates into 100 orthonormal eigenvectors and 200 variations of the PDF parameters in the plus and minus direction.

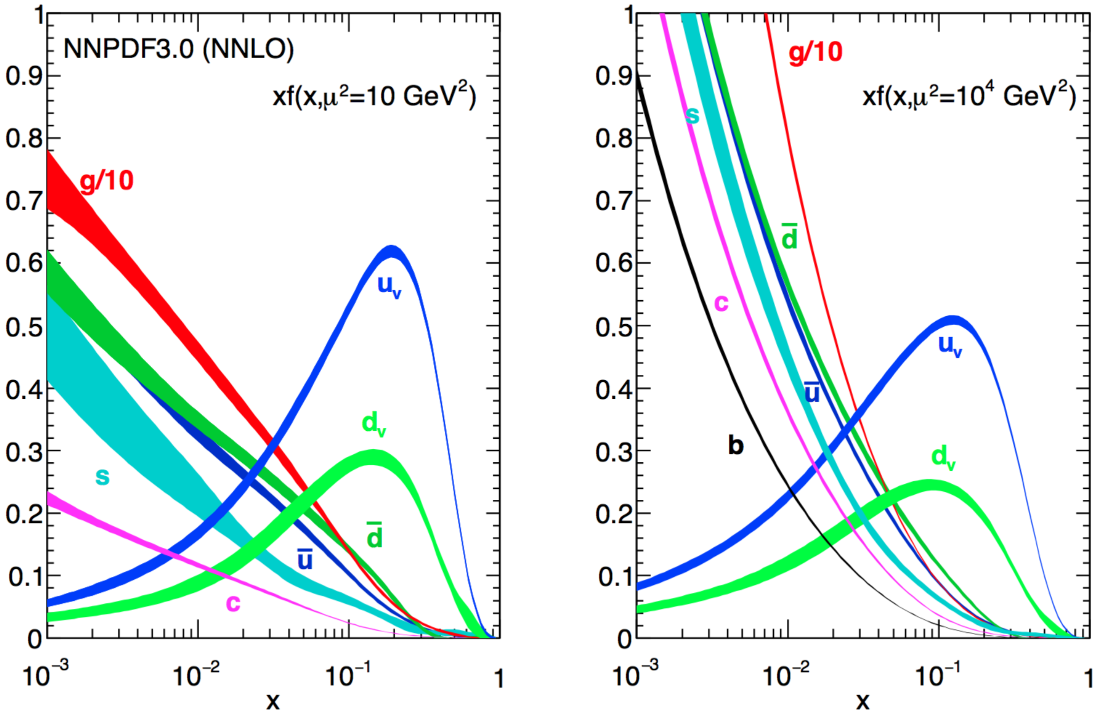

Figure 3.2: The momentum fraction x times the parton distribution functions $f(x)$, where $f = \mathrm{u_v}, \mathrm{d_v}, \bar{\mathrm{u}}, \bar{\mathrm{d}}, \mathrm{s}, \mathrm{c}$, or g as a function of the momentum fraction obtained in the NNLO `NNPDF3.0` global analysis at factorisation scales $\mu^2 = 10\,\mathrm{GeV}^2$ (left) and $\mu^2 = 10^4\,\mathrm{GeV}^2$ (right), with $\alpha_S(M_Z^2) = 0.118$. The gluon PDF has been scaled down by a factor of 0.1. Figure taken from [6].

Quantum fluctuations can cause divergences at high energies. This is solved by introducing a a renormalization scale μ_R to redefine physical quantities, making the theory still able to describe the experimental regime. A consequence of this method is that the coupling constants will run as a function of μ_R. Beyond the renormalization scale, the high energy effects such as the loop corrections to propagators (self energy) are absorbed in the physical quantities through a renormalization of the fields. In particular the running behaviour of the strong coupling constant[1] α_S is found to be

$$\alpha_S = \frac{\alpha_S(\mu_0^2)}{1 + \alpha_S(\mu_0^2)\frac{33-2n_f}{12\pi}\ln\left(\frac{|\mu_R^2|}{\mu_0^2}\right)}, \tag{3.3}$$

with n_f the number of quarks and μ_0 the reference scale at which the coupling is known. The current world average of the strong coupling constant at the Z boson mass is $\alpha_S(\mu_R = m_Z) = 0.1181 \pm 0.0011$ [6]. From Equation 3.3 one can see easily that the coupling strength decreases with increasing renormalization scale, this is known as asymptotic freedom. Additionally, following the behaviour of $\alpha_S(\mu_R^2)$, a limit $\Lambda_{QCD} \approx 200\,\mathrm{MeV}$ is found for which α_S becomes larger than one. Under this limit, the perturbative calculations of observables can no longer be done.

[1]The strong coupling constant is defined as $\alpha_S = \frac{g_S^2}{4\pi}$.

Cross sections can be written in terms of interacting vertices contributing to the matrix element (ME) originating from elements of a perturbative series [105], allowing them to be expanded as a power series of the coupling constant α

$$\sigma = \sigma_{\mathrm{LO}}\left(1 + \left(\frac{\alpha}{2\pi}\right)\sigma_1 + \left(\frac{\alpha}{2\pi}\right)^2 \sigma_2 + \ldots\right). \tag{3.4}$$

Leading order (LO) accuracy contains the minimal amount of vertices in the process, then depending on where the series is cut off one speaks of next-to-leading order (NLO), or next-to-next-to-leading order (NNLO) accuracy in α. Predictions including higher order corrections tend to be less affected by theoretical uncertainties originating from a variation of the chosen renormalization and factorisation scales.

3.2 Event generation

In order to compare reconstructed data with theoretical predictions, collision events are generated and passed through a simulation of the CMS detector and an emulation of its readout. For the detector simulation, a so-called Full Simulation package [106, 107] based on the `Geant4` toolkit [108] is employed. This allows detailed simulations of the interactions of the particles with the detector material.

3.2.1 Fundamentals of simulating a proton collision

The generation of $\mathrm{pp} \to \mathrm{X}$ events is subdivided into sequential steps [109–111], as shown in Figure 3.3.

The interaction of two incoming protons is often soft and elastic leading to events that are not interesting in the framework of this thesis. More intriguing are the hard interactions between two partons from the incoming protons. The event generation starts from the matrix elements of a hard scattering process of interest. The corresponding cross section integral is sampled using Monte Carlo techniques and the resulting sample of events reflect the probability distribution of a process over its final state phase space. A parton shower (PS) program is then used to simulate the hadronisation of final state partons, coming from the sample of events of the hard interaction, into hadrons which then decay further. On top of this, radiation of soft gluons or quarks from initial or final state partons is simulated. These are respectively referred to as initial state radiation (ISR) or final state radiation (FSR). The contributions from soft secondary interactions, the so-called underlying event (UE), and colour reconnection effects are also taken into account. A brief overview of the employed programs used for the event generation of the signal and main background processes used in the search presented in the thesis is given in Section 3.2.2.

3.2.2 Programs for event generation

The `FEYNRULES` package [112] allows for the calculation of the Feynman rules in momentum space for any quantum field theory model. By use of a Lagrangian, the set of Feynman rules associated with this Lagrangian is calculated. Via the `Universal Feynrules Output` (UFO) [113] the results are then passed to matrix element generators.

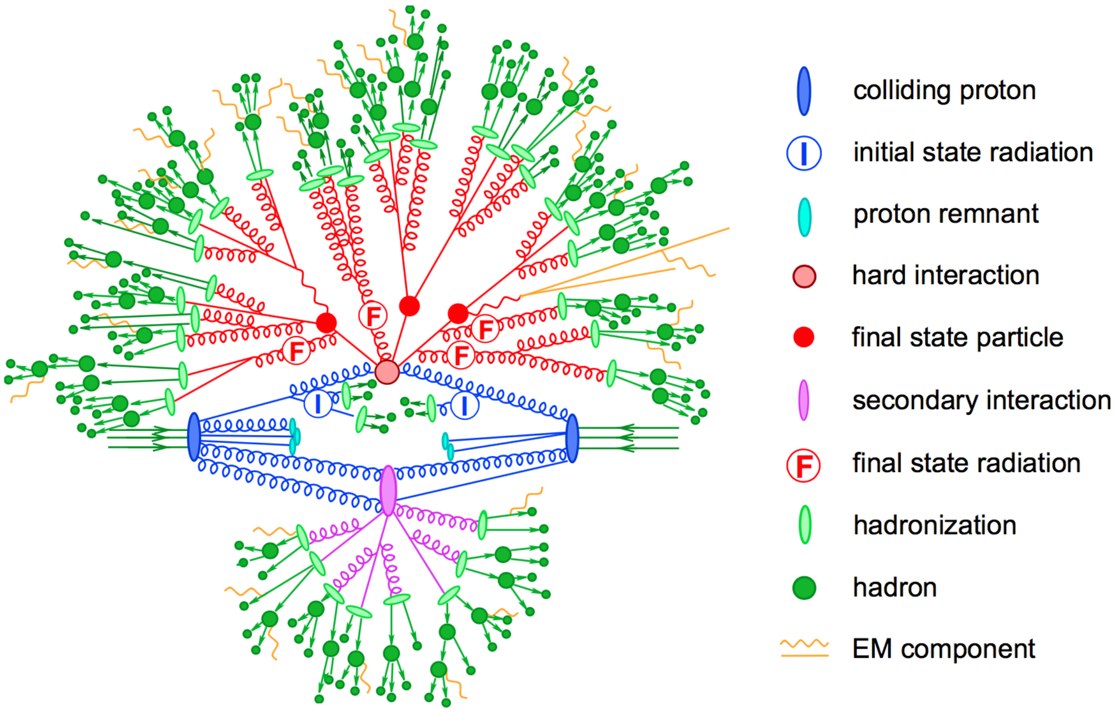

Figure 3.3: Sketch of a hadron collision as simulated by a Monte-Carlo event generator. The red blob in the centre represents the hard collision, surrounded by a tree-like structure representing Bremsstrahlung as simulated by parton showers. The purple blob indicates a secondary hard scattering event. Parton-to-hadron transitions are represented by light green blobs, dark green blobs indicate hadron decays, while yellow lines signal soft photon radiation. Figure taken from [111].

The `MadGraph` program [114] is used to interpret the physics model and calculate the corresponding Feynman diagrams and matrix elements. After this, `MadEvent` [115] is used to calculate the corresponding partons. These generated parton configurations are then merged with `Pythia` [116–118] parton showers using the MLM merging scheme [119].

The `MadGraph5_aMC@NLO` program [120] combines the LO `MadGraph` [114] and the `aMC@NLO` program into a common framework. This combination supports the generation of samples at LO or NLO together with a dedicated matching to parton showers using the MC@NLO [121] or FxFx [122] schemes respectively. The FXFX scheme produces a certain fraction of events with negative weights originating from the subtraction of amplitudes that contain additional emissions from the NLO matrix element to prevent double-counting.

The `POWHEG` box (versions 1 and 2) [123–128] contains predefined implementations of various processes at NLO. It applies the `POWHEG` method for ME- to PS- matching, where the hardest radiation generated from the ME has priority over subsequent PS emission to remove the overlap with the PS simulation.

The `JHU` generator (version 7.02) [129–132] is used to generate the parton level information including full spin and polarization correlations. It is commonly used for studying the spin and parity properties of new resonances such as $ab \to X \to VV$, where $V = Z, W, \gamma$).

The generation of events from processes involving the production and decay of resonances creates a computational heavy load, especially at NLO. The narrow width approximation assumes that the resonant particle is on-shell. This factorizes the production and decay amplitude, allowing to perform the simulation of the production and decay of heavy resonances like top quarks or Higgs bosons to be performed in separate steps. The `MadSpin` program [133] extends this approach and accounts for off-shell effects through a partial reweighting of the events. Additionally, spin correlation effects between production and decay products are taken into account.

The `Pythia` program (versions 6 and 8) [116–118] generates events of various processes at LO. However more commonly it is only used for its PS simulation and is then used after other LO and NLO event generators to perform subsequent parton showering, hadronisation, and simulation of the underlying event. In this thesis the underlying event tunes [134] are the CUETP8M2T4, CUETP8M1 and CUETP8M2.

The detector response is simulated via the `Geant4` [108] program. This program tracks the particles through the detector material via a detailed description of the detector and generates several hits throughout several sensitive layers. In addition, the response of the detector electronics to these hits are simulated.

3.2.3 Generating FCNC top-Z interactions

The FCNC processes are generated by interfacing the Lagrangian in Equation 1.36 with `MadGraph5_aMC@NLO` by means of the `FeynRules` package and its `Universal Feynrules Output` format. The complex chiral parameters are arbitrary chosen to be $f^{L}_{Xq} = 0$ and $f^{R}_{Xq} = 1$. The processes are generated with the `MadGraph5_aMC@NLO` (version 2.2.2) and showered with `Pythia` (version 8.22). The signal consists of two components: events describing the top quark pair production followed by an FCNC decay of one top quark ($t \rightarrow Zq$), and events with the FCNC single top quark production ($Zq \rightarrow t$) for which the top quark decays according the to SM. The leading order generation of the single top quark FCNC process tZ+0,1 jet including a merging technique can not be done since tZ+1 jet also contains contributions from top quark pair FCNC where one quark is decaying in tZ. Therefore, single top quark and top quark pair processes are generated independently, where the single top quark process is generated without the extra hard jet, and the top quark pair FCNC process is generated with up to two extra jets.

NOTE: RH and LH gave the same resulting variables and RH is easier to simulate since those are singlets under SU2 (no doublet with b)

The signal rates are estimated by use of the `MadGraph5_aMC@NLO` program for estimating the partial widths. The anomalous couplings are left free to float for this estimation, and only one coupling is allowed to be non-vanishing at a time. The results are presented in Table 3.1.

The anomalous single top quark cross sections are calculated by convolution of the hard scattering matrix elements with the LO order set of `NN23LO1` [135] partons densities. The NLO effects are modelled by multiplying each LO cross section by a global k-factor. The LO single top quark production cross section and the global k-factors for the top-Zproduction are shown in Table 3.2. The hard scattering events are then matched to parton showers to `Pythia` to account for the simulation of the QCD environment relevant for hadronic collisions.

Table 3.1: Leading order partial widths related to the anomalous decay modes of the top quark, where the new physics scale Λ is given in GeV.

Anomalous coupling	vertex	Partial decay width (GeV)
κ_{tZq}/Λ	tZu	$1.64 \times 10^{4} \times \left(\kappa_{tZu}/\Lambda\right)^2$
	tZc	$1.64 \times 10^{4} \times \left(\kappa_{tZc}/\Lambda\right)^2$
ζ_{tZq}	tZu	$1.69 \times 10^{-1} \times \left(\zeta_{tZu}\right)^2$
	tZc	$1.68 \times 10^{-1} \times \left(\zeta_{tZc}\right)^2$

Table 3.2: Leading order single top quark production cross section at a centre-of-mass of 13 TeV for $pp \to tZ$ or $\bar{t}Z$, where the new physics scale is given in GeV. The NLO *k*—factors [136] are given in the last column.

Anomalous coupling	vertex	Cross section (pb) $pp \to t + pp \to \bar{t}$	$\sigma_{pp\to\bar{t}}/\sigma_{pp\to t}$	NLO *k*—factor
κ_{tZq}/Λ	tZu	$1.92 \times 10^{7} \times \left(\kappa_{tZu}/\Lambda\right)^2$	0.12	1.40
	tZc	$2.65 \times 10^{6} \times \left(\kappa_{tZc}/\Lambda\right)^2$	0.50	1.40
ζ_{tZq}	tZu	$8.24 \times 10 \times \left(\zeta_{tZu}\right)^2$	0.14	1.40
	tZc	$1.29 \times 10 \times \left(\zeta_{tZc}\right)^2$	0.50	1.40

The top quark pair cross sections are derived from the SM $t\bar{t}$ cross section, calculated with `MadGraph5_aMC@NLO` at NLO at a centre-of-mass of 13 TeV ($\sigma_{t\bar{t}}^{SM,NLO} = 6.741 \times 10^2$pb), and considering the decay $t\bar{t} \to (bW^{\pm})(Xqt)$. The branching ratio $\mathcal{B}(t \to bW^{\pm})$ is assumed to be equal to one and the FCNC branching ratio is calculated as

$$\mathcal{B}(t \to qX) = \frac{\Gamma_{t\to qX}}{\Gamma_t^{SM} + \Gamma_t^{FCNC}} \approx \frac{\Gamma_{t\to qX}}{\Gamma_t^{SM}}, \tag{3.5}$$

where $\Gamma_{t\to qX}$ is given in Table 3.1, $\Gamma_t^{SM} = 1.32$GeV [47], and the assumption $\Gamma_t^{FCNC} \ll \Gamma_t^{SM}$ is made. In Table 3.3 the resulting NLO cross sections for the top-Z FCNC interactions are given.

Table 3.3: Next to leading order top quark pair cross section for the top-Z FCNC interactions $t\bar{t} \to (bW^{\pm})(Xqt)$ with with a full leptonic decay at a centre-of-mass of 13 TeV, where $\sigma^{\mathrm{SM,NLO}}_{pp\to t\bar{t}} = 6.741 \times 10^{2}$pb, $\mathscr{B}(Z \to \ell\bar{\ell}) = 3.36 \times 3 \times 10^{-2}$, and $\mathscr{B}(W \to \ell\nu) = 10.80 \times 3 \times 10^{-2}$.

Anomalous coupling	vertex	Process	Cross section (pb)	
κ_{tZq}/Λ	tZu	$t\bar{t} \to (b\ell^{+}\nu)(\bar{u}\ell^{+}\ell^{-})$	2.727×10^{5}	$\times \left(\kappa_{tZu}/\Lambda\right)^{2}$
		$t\bar{t} \to (\bar{b}\ell^{-}\bar{\nu})(u\ell^{+}\ell^{-})$	2.727×10^{5}	$\times \left(\kappa_{tZu}/\Lambda\right)^{2}$
	tZc	$t\bar{t} \to (b\ell^{+}\nu)(\bar{c}\ell^{+}\ell^{-})$	2.726×10^{5}	$\times \left(\kappa_{tZc}/\Lambda\right)^{2}$
		$t\bar{t} \to (\bar{b}\ell^{-}\bar{\nu})(c\ell^{+}\ell^{-})$	2.726×10^{5}	$\times \left(\kappa_{tZc}/\Lambda\right)^{2}$
ζ_{tZq}	tZu	$t\bar{t} \to (b\ell^{+}\nu)(\bar{u}\ell^{+}\ell^{-})$	2.807	$\times \left(\zeta_{tZu}\right)^{2}$
		$t\bar{t} \to (\bar{b}\ell^{-}\bar{\nu})(u\ell^{+}\ell^{-})$	2.807	$\times \left(\zeta_{tZu}\right)^{2}$
	tZc	$t\bar{t} \to (b\ell^{+}\nu)(\bar{c}\ell^{+}\ell^{-})$	2.807	$\times \left(\zeta_{tZc}\right)^{2}$
		$t\bar{t} \to (\bar{b}\ell^{-}\bar{\nu})(c\ell^{+}\ell^{-})$	2.807	$\times \left(\zeta_{tZc}\right)^{2}$

3.2.4 Generating SM background events

The SM tZq sample is generated using the MadGraph5_aMC@NLO generator (version 2.2.2) [137] at leading order accuracy. The $t\bar{t}Z$ and triboson samples were generated using the MadGraph5_aMC@NLO generator (version 2.2.2), interfaced through the dedicated MC@NLO matching scheme [121] The WZ+jets and $t\bar{t}W$, samples are produced with up to one additional parton at next-to-leading order accuracy using MadGraph5_aMC@NLO (version 2.2.2) and using FxFx approach [138] for matching and merging. Other minor background are simulated using different generators. The samples of $t\bar{t}H$, WW, ZZ, and single top quark production channels are generated with the POWHEG box (versions 1 and 2) [123–128]. The JHU generator [129–132] is used for the tqH sample, while the tWZ sample is generated using MadGraph [114] interfaced with the MLM matching scheme [119]. All events are interfaced to Pythia version 8.22 [118] to simulate parton shower, hadronisation, and underlying event. Additionally, MadSpin is used for the tZq, WZ+jets, $t\bar{t}Z$, $t\bar{t}W$, tWZ, and triboson samples

The complete list of SM samples is given in Table 3.4, along with their cross sections at a centre-of-mass of 13 TeV. The cross sections without a reference are coming from the generator with which the sample has been made, for some of them the uncertainties are provided by the Generator Group [139]. For each MC sample, the integrated luminosity that the sample represents is estimated as the number of simulated events divided by the cross section of the generated process. This luminosity is then matched to integrated luminosity of 35.9 fb^{-1} represented by the data used for analysis. For processes generated with MadGraph5_aMC@NLO, the effective number of simulated events is used, taking into account positive and negative event weights. In Figure 3.4, a summary is given of the SM cross section measurements performed by the CMS collaboration. These cross sections are all in agreement with their SM predictions.

Table 3.4: SM MC samples used in this analysis with their corresponding cross section at a centre-of-mass of 13 TeV and `MadGraph5_aMC@NLO` correction C when applicable. The generators used for each sample are indicated and the simulation of the parton shower, hadronisation, and underlying event is done by `Pythia` version 8.22 [118] for all samples.

Process	Generator	Cross section (pb)	C	Ref.
$\mathrm{WZ} \to 3\ell\nu$	MadGraph5_aMC@NLO+MadSpin	5.26	1.61	[139]
tZq with $\mathrm{Z} \to \ell^+\ell^-$	MadGraph5_aMC@NLO+MadSpin	0.0758	3.77	[139]
tqH with $\mathrm{H} \to \mathrm{ZZ} \to \ell^+\ell^-\ell^+\ell^-$	JHU	$8.80\ 10^{-6}$	-	[139]
$\mathrm{t\bar{t}W}$+jets with $\mathrm{W} \to \ell\nu$	MadGraph5_aMC@NLO+MadSpin	0.2043 ± 0.0020	1.94	[139]
$\mathrm{t\bar{t}Z} \to 2\ell + 2\nu +$ other, with $m_{\ell\ell} > 10$ GeV	MadGraph5_aMC@NLO+MadSpin	0.2529 ± 0.0004	2.15	[139]
$\mathrm{t\bar{t}H}$,no $\mathrm{b\bar{b}}$ decays	POWHEG	0.2151	-	[139]
$\mathrm{t\bar{t}H}$, $\mathrm{b\bar{b}}$ decays	POWHEG	0.2934	-	[139]
$\mathrm{WW} \to 2\ell 2\nu$	POWHEG	12.178	-	[140]
$\mathrm{ZZ} \to 4\ell$	POWHEG	0.3366	-	[139]
WZZ	MadGraph5_aMC@NLO+ MadSpin	0.05565	1.14	[139]
ZZZ	MadGraph5_aMC@NLO	0.01398	1.17	[139]
single top quark tWZ, with $\mathrm{Z}_\mu \to \ell^+\ell^-$	MadGraph5_aMC@NLO(LO)+MadSpin	0.001123	-	[139]
single top quark t-channel $\mathrm{\bar{t}}$	POWHEG+MadSpin	$44.33\ ^{+1.76}_{-1.49}$	-	[139]
single top quark t-channel t	POWHEG+MadSpin	$26.38\ ^{+1.32}_{-1.18}$	-	[139]
single top quark $\mathrm{\bar{t}W}$	POWHEG	35.85 ± 0.90 (scale) ± 1.70 (PDF)	-	[139]
single top quark tW	POWHEG	35.85 ± 0.90 (scale) ± 1.70 (PDF)	-	[139]
$\mathrm{t\bar{t}}$	POWHEG	$831.76\ ^{+19.77+35.06}_{-29.20-35.06}$	-	[139]
Z/γ^* + jets, with $m_{\ell\ell} >$ 50GeV	MadGraph5_aMC@NLO	$3 \times (\ 1921.8 \pm 0.6 \pm 33.2\ )$	1.49	[139]
Z/γ^* + jets, with 10 GeV $< m_{\ell\ell} <$ 50 GeV	MadGraph	18610	-	[139]

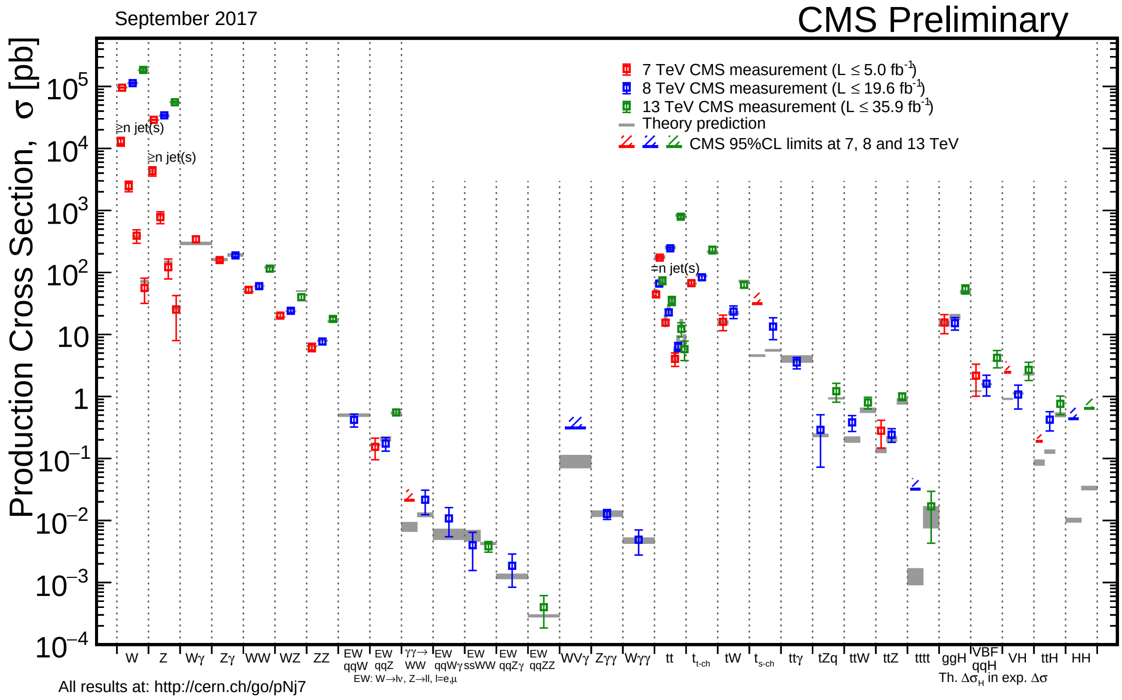

Figure 3.4: Summary of the SM cross section measurements performed by the CMS collaboration. Figure taken from [23]

3.3 Multivariate analysis techniques: Boosted Decision Trees

The need of processing large quantities of data and discriminating between events with largely similar experimental signatures makes multivariate analysis (MVA) a largely used method in the physics community. Multivariate classification methods based on machine learning techniques are a fundamental ingredient to most analyses. The advantage of using a MVA classifier is that it can achieve a better discrimination power with respect to a simpler analysis based on individual selection criteria or poorly discriminating variables. A risk of using MVA classifiers is overtraining. This happens when there are too many model parameters of an algorithm adjusted to too few data points. This leads to an increase in the classification performance over the objectively achievable one.

There are many software tools that exist for MVA. In this thesis the `Tool for Multivariate Analysis` (TMVA) [141] is used. This software is an open source project included into `ROOT` [142]. By training on events for which the classification is known, a mapping function is determined that describes a classification or an approximation of the underlying behaviour defining the target value (regression). In this thesis boosted decision trees (BDT) are employed for the classification of events as implemented in the `TMVA` framework [141]. This multivariate technique is based on a set of decision trees where each tree yields a binary output depending on the fact that an event is signal- or background-like. This has as advantage that several discriminating variables can be combined into a powerful one-dimensional discriminant D.

The decision tree is constructed by training on a dataset for which the outcome is already provided, such as simulation datasets with signal and background processes (supervised learning). Different trees can be combined into a forest where the final output is determined by the majority vote of all trees, so-called boosting. This stabilises the decision trees against statistical fluctuations and makes it possible to keep the decision trees very shallow, making the method more robust against overtraining. Examples of such boosting algorithms are Adaptive Boosting (AdaBoost) and Gradient Boosting [143]. In this thesis Gradient boost is used with a learning rate of 0.2-0.3 and the depth of the tree is set to three. Additionally, the Gradient boost is used in combination with bagging, so-called stochastic gradient boosting. Bagging smears the statistical fluctuations in the training data and therefore stabilises the response of the classifier and increases the performance by eliminating overtraining. More information about stochastic gradient boosting can be found in Ref. [144].

The discriminating power of a BDT is assessed by analysing the receiver operating characteristic (ROC) curve. This curve represents the background rejection over the signal efficiency of the remaining sample. The area under the curve (AUC) is compared to random guessing in order to identify the best classifier can be identified. When the multivariate discriminator has no discriminating power, the resulting AUC will be 0%, while 50% means fully separated event classes. In Figure 3.5 examples of ROC curves are shown.

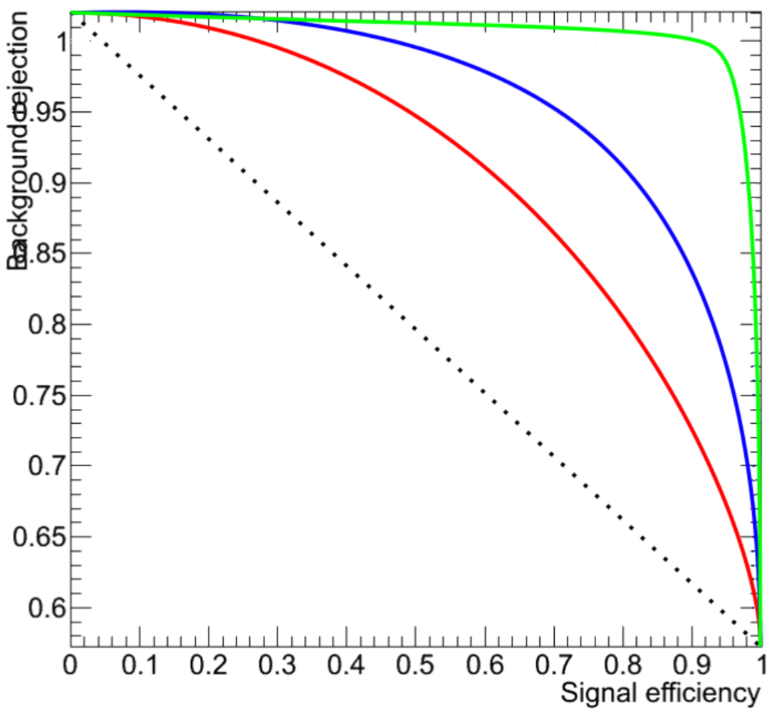

Figure 3.5: Example of ROC curves. In this example, the green method is better than the blue one, which is better than the red one. The dashed line represents a case where there is no separation. Figure taken from [145].

3.4 Statistical methodology

The search performed in the framework of this thesis requires the simultaneous analysis of data from different decay channels. The statistical methodology used for this search is developed by the ATLAS and CMS collaborations in the context of the LHC Higgs Combination group [146–149]. The `Higgs Combined Tool` [150] is a `RooStats` [151] framework which runs different statistical methods. In this section, only the statistical tools necessary for the performed search are described [152].

The event yields of signal and background processes are denoted as s and b respectively. These represent event counts in multiple bins or unbinned probability density functions. By use of simulation, predictions on both signal and background yields are made the multiple uncertainties on these predictions are accounted for by introducing nuisance parameters θ such that $s = s(\theta)$ and $b = b(\theta)$.

The Bayesian and modified classical frequentist statistical approaches are used in high energy physics to characterise the absence of a signal. The level of incompatibility of data with a signal hypothesis is quantified in terms of confidence levels (CL). The convention is to require a 95% CL for excluding a signal. In general limits are not set on the signal cross section directly, but are set on the signal strength modifier μ. The signal strength modifier is defined such that it equally changes all the cross sections of all production mechanisms of the signal by the same scale.

In this thesis, the modified frequentist approach [153, 154] for confidence levels that adopts the classical frequentist method to allow nuisance parameters, is used. Ir constructs a likelihood $\mathfrak{L}(\text{data}|\,\mu,\theta)$ is as

$$\mathfrak{L}(\text{data}|\,\mu,\theta) = \text{Poisson}\big(\text{data}|\,\mu s(\theta) + b(\theta)\big)\ \text{pdf}(\tilde{\theta}|\theta). \tag{3.6}$$

The probability density function $\text{pdf}(\tilde{\theta}|\theta)$ describes all sources of uncertainty. In this thesis, all sources of uncertainties are assumed to be either 100% correlated or uncorrelated. Partially correlated uncertainties are broken down to subcomponents that fit those requirements, allowing to include all constraints in the likelihoods in a clean factorised form.

A systematic uncertainty pdf $\rho(\theta|\tilde{\theta})$ for the nuisance θ with nominal value $\tilde{\theta}$ is used. It reflects the degree of belief of what the true value of the θ is. In this thesis, the approach from the `Higgs Combined Tool` is used where the pdfs $\rho(\theta|\tilde{\theta})$ are re-interpret as posteriors of real or imaginary measurements $\tilde{\theta}$

$$\rho(\theta|\tilde{\theta}) \sim \text{pdf}(\tilde{\theta}|\theta)\ \pi_\theta(\theta), \tag{3.7}$$

where $\pi_\theta(\theta)$ is the hyper prior for the (imaginary) measurements. The the pdfs used by the `Higgs Combine Tool` are described in Ref. [149].

The data in Equation 3.6 represents either the actual observation or pseudo-data to construct sampling distributions. For a binned likelihood, the Poisson probabilities to observe n_i events in bin i is given as

$$\text{Poisson}\big(\text{data}|\,\mu s(\theta) + b(\theta)\big) = \prod_\text{i} \frac{\big(\mu s_\text{i}(\theta) + b_\text{i}(\theta)\big)^{n_\text{i}}}{n_\text{i}!} e^{-\mu s_\text{i}(\theta) - b_\text{i}(\theta)}. \tag{3.8}$$

At the LHC, the test statistic is defined as

$$q_{\mu} = -2 \ln \frac{\mathfrak{L}(\text{data}|\,\mu, \hat{\theta}_{\mu})}{\mathfrak{L}(\text{data}|\,\hat{\mu}, \hat{\theta}_{\mu})}, \tag{3.9}$$

where the likelihood is maximised in the numerator (maximum likelihood estimator, MLE) for a given μ and (pseudo) data at $\hat{\theta}_{\mu}$, while $\hat{\mu}$ combined with $\hat{\theta}$ defines the point for which the likelihood reaches its global maximum. The estimated signal strength modifier $\hat{\mu}$ can not become negative since a signal rate is positive defined by physics. Furthermore, an upper constraint on the MLE $\hat{\mu} \leq \mu$ is imposed.

The signal is excluded at $1 - \alpha$ confidence level when

$$\text{CLs} = \frac{\mathrm{P}\left(q_{\mu} \geq q_{\mu}^{\text{obs}}|\,\mu s + b\right)}{\mathrm{P}\left(q_{\mu} \geq q_{\mu}^{\text{obs}}|\,b\right)} \leq \alpha, \tag{3.10}$$

with $\mathrm{P}\left(q_{\mu} \geq q_{\mu}^{\text{obs}}|\,\mu s + b\right)$ the probability to observe a value of the test statistic at least as large as the one observed in data q_{μ}^{obs}, under the signal plus background ($s + b$) hypothesis, and $\mathrm{P}\left(q_{\mu} \geq q_{\mu}^{\text{obs}}|\,b\right)$ for the background only (b) hypothesis. These probabilities are defined as

$$\begin{aligned} p_{\mu} &= \mathrm{P}\left(q_{\mu} \geq q_{\mu}^{\text{obs}}|\,\mu s + b\right) = \int_{q_{\mu}^{\text{obs}}}^{\infty} f(q_{\mu}|\,\mu, \hat{\theta}_{\mu}^{\text{obs}})\, dq_{\mu}, \\ 1 - p_b &= \mathrm{P}\left(q_{\mu} \geq q_{\mu}^{\text{obs}}|\,b\right) = \int_{q_{\mu=0}^{\text{obs}}}^{\infty} f(q_{\mu}|\,\mu = 0, \hat{\theta}_{\mu=0}^{\text{obs}})\, dq_{\mu}, \end{aligned} \tag{3.11}$$

where p_{μ} and p_b are the p-values associated to the two hypothesis, and $f(q_{\mu}|\,\mu, \hat{\theta}_{\mu}^{\text{obs}})$ and $f(q_{\mu}|\,\mu = 0, \hat{\theta}_{\mu=0}^{\text{obs}})$ are the probability density functions of the signal plus background and background only hypothesis constructed from toy Monte Carlo pseudo data. These are generated with nuisance parameters fixed to $\hat{\theta}_{\mu=0}^{\text{obs}}$ (background only) and $\hat{\theta}_{\mu}^{\text{obs}}$ (signal plus backgound). The 95% CL level upper limit on μ is achieved by adjusting μ until CL$= 0.05$, this is the so-called observe limit. The expected median upper limit and the $\pm 1\sigma$ and $\pm 2\sigma$ bands for a hypothesis is generated by a large set of pseudo data and calculate the CLs and the value of μ at 95% CL for each of them. A cumulative probability distribution can be build by starting the integration from the side corresponding to low event yields. The median expected value, so-called expected limit at 95% CL, is where the cumulative distribution function crosses the 50% quantile. The $\pm 1\sigma$ (68%) and $\pm 2\sigma$ (95%) bands on the expected limit are defined by the crossings of the 16% and 84%, and 2.5% and 97.5% quantiles.

In order to significantly reduce computing time, the Asymptotic CL method is used. This method avoids an ensemble of toy Monte Carlo samples and instead replaces it by one representative dataset, called Asimov dataset. This dataset is constructed such that all observed quantities are set equal to their MLE values ($\hat{\theta}_{\text{Asimov}} = \theta_0$). More information about this procedure can be found in Refs. [147].

4 Event reconstruction and identification

The simulated data after the detector simulation described in Section 3.2, has the exact same format as the real collision data recorded at the CMS experiment. Therefore the same software can be used for the reconstruction of both simulation and real data. In Section 4.1, the object reconstruction is explained. After reconstructing the objects, they are connected to physics objects need to be identified (Section 4.2) and corrected for pileup (Section 4.3). The objects used for physics analysis have extra requirements as shown in Section 4.4. A summary of all the corrections applied to data and simulation is given in Section 4.5.

4.1 Object Reconstruction

In Figure 4.1, the particle interaction in a transverse slice of the CMS detector is shown. When a particle enters the detector, it first enters the tracker where charged particle trajectories, so-called tracks, and origins, so-called vertices, are reconstructed from signals or hits in the sensitive layers. The magnetic field bends the charged particles making it able to measure the electric charges and momenta of charged particles. The electron and photons are absorbed in the ECAL and the corresponding electromagnetic showers are detected as clusters of energy in adjacent cells. From this, the energy and the direction of the particles can be determined. The charged and neutral hadrons can also initiate a hadronic shower in the ECAL that is fully absorbed in the HCAL. The clusters from these showers are also used to estimate the energy and direction. Muons and neutrino's pass through the calorimeters without little to no energy loss and the neutrinos even escape the CMS detector undetected while muons produce hits in the muon detectors.

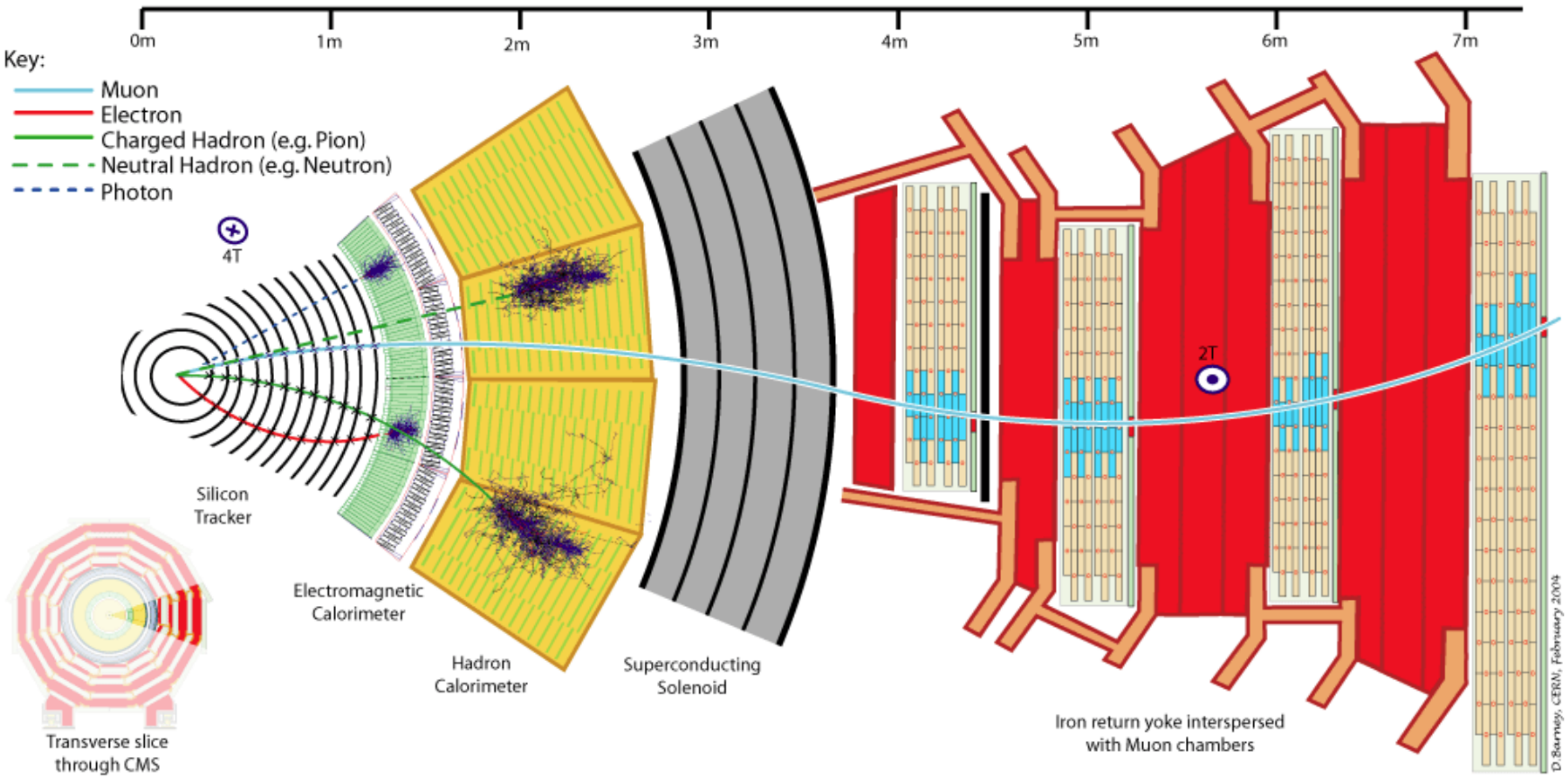

Figure 4.1: Cross-section of the CMS detector with all parts of the detector labelled. This sketch shows the specific particle interactions from a beam interaction reign to the muon detector. The muon and charged pion are positively charged, the electron is negatively charged. Figure taken from [155].

The particle flow (PF) [155] reconstruction algorithm correlates the tracks and clusters from all detector layers with the identification of each final state particle, and combines the corresponding measurements to reconstruct the properties. The muon is identified by a track in the inner tracker connected to a track in the muon detector as described in Section 4.1.2. The electrons are identified by a track and an ECAL cluster, not connected to an HCAL cluster as described in Section 4.1.3. The ECAL and HCAL clusters without a track link identify the photons and neutral hadrons, while the addition of the tracker determines the energy and direction of a charged hadron.

NOTE: Ik kan hier stoppen en 4.1.1, 4.1.2, 4.1.3.4.1.4 volledig schrappen (dus enkel primary vertex houden)

4.1.1 Charged particle tracks

An iterative tracking algorithm is responsible for the reconstruction of the tracks made by charged particles in the inner tracking system. Each iteration consists of four steps [71]: the track-seed generation, the pattern recognition algorithm, removal of track-hit ambiguities and a final track fit. The pattern recognitions done by use a Kalman filter method [156, 157] which into account the magnetic field and multiple scattering effects. All hits that are unambiguously associated to the final track are removed from the list of available hits. In order to associate the remaining hits, the procedure is repeated with looser track reconstruction criteria. The use of the iterative track reconstruction procedure has a high track finding efficiency, where the fake track reconstruction rate is negligible.

4.1.2 Following the Muon's Footsteps

The muon reconstruction [158] has three subdivisions: local reconstruction, regional reconstruction and global reconstruction. The local reconstruction is performed on individual detector elements such as strip and pixel hits in the inner tracking system, and muon hits and/or segments in the muon chambers. Independent tracks are reconstructed in the inner tracker - called tracker tracks - and in the muon system, called standalone muon tracks. Based on these tracks, two reconstructions are considered: Gloval Muon reconstruction and Tracker Muon reconstruction. The first is an outside in approach starting from a standalone muon track while the second uses an inside-out approach starting from tracker tracks. For low transverse momenta ($p_{\mathrm{T}} \lesssim 5$ GeV), the tracker muon reconstruction is more efficient than the global muon approach. This is due to the fact that tracker muons only require a single muon segment in muon system, while the global muon approach requires typically segments in at least two muon stations. These tracker muons are used for identifying muons from the hadronisation of b or c quarks. The global muon approach typically improves the tracker reconstruction for $p_{\mathrm{T}} \gtrsim 200$ GeV.

4.1.3 The path of the Electron

Standard tracking algorithms are based on Kalman filtering which assume that the energy loss is Gaussian distributed. Since the electron tracks are increasingly curved in the magnetic field as a function of its flight distance, these standard tracking algorithms are not suitable to fit the electron tracks and different filtering algorithm, the Gaussian sum filter (GSF) [159] is used instead.

In CMS, the electrons are reconstructed in two ways. The older ECAL based tracking is developed to identify high energetic isolated electrons. This tracking algorithm starts from

ECAL clusters with a transverse energy above 4 GeV and extrapolates from these cluster the position of the hits in the tracker. Another, tracker based algorithm uses all the tracks with a p_{T} higher than 2 GeV found with iterative tracking as seeds. The electron seeds from the ECAL- and tracker-based procedures are merged into a unique collection and are then refitted by using the summed Gaussian distributions as uncertainty per hit in the track fit. The electron efficiency is measured in 8 TeV proton collision data to be better than 93% for electrons with an ECAL supercluster energy of $E_{\mathrm{T}} > 20$ GeV [160]. For electrons with an $E_{\mathrm{T}} > 25$ GeV in 13 TeV proton collision data, the efficiency is about 96%[161].

4.1.4 Primary Vertex Reconstruction

The primary vertex (PV) reconstruction is able to measure the location of all proton interaction vertices in each event consisting of the signal vertex an all vertices from pileup events. First tracks are selected to be consistent with being produced promptly in the primary interaction [81]. Then the tracks are grouped according to the z coordinate of their closest approach to the beam line [162] and a vertex fitting algorithm [163] is performed. The primary vertex is found as the vertex corresponding to the highest sum of squared track transverse momenta and is taken to be the main interaction point. The resolution on the primary vertex is about 14 µm in $r\phi$ and about 19 µm in the z direction for primary vertices with the sum of the track $p_T > 100$ GeV for 2016 data taking.

4.1.5 Calorimeter clusters

The energy and direction of stable neutral particles such as photons and neutral hadron are reconstructed using a cluster algorithm. This algorithm also separates neutral particles from charged hadron energy deposits, and reconstructs and identifies electrons and their bremsstrahlung photons. Furthermore, the cluster algorithm is contributing to the energy measurements of charged hadrons that don't have accurate tracks parameters, e.g. for low quality and high transverse momentum tracks. The clustering is performed separately in each subdetetector: ECAL barrel and endcaps, HCAL barrel and endcaps, and the two preshower layers. The HF has no clustering algorithm since the electromagnetic or hadronic components give rise to an HF EM or HF HAD cluster.

The clustering algorithm consist of different steps. First seeds are identified when cells have an energy larger than the seeding threshold and larger than their neighbouring cells. Then topological clusters are made by accumulating cells that share at least a corner with a cell already in the cluster and an energy above a cell threshold set to twice the noise level. The third step is an expectation maximization algorithm that reconstructs the cluster [155] and assumes that the energy deposits are Gaussian distributed. The calorimeter clusters are used for reconstructing photons and neutral hadrons. The clusters that are not in the vicinity of the extrapolated charged tracks identified as neutral hadrons or photons. If the energy deposits are in vicinity of charged tracks, such is the case for charged hadrons, the neutral particle energy deposit is measured as an excess over the charged particle deposit.

4.2 Particle flow identification

The several PF elements from the various CMS subdetectors are connected through a link algorithm. This algorithm tests any pair of elements in an event, only considering nearest neighbours in the $\eta\phi$-plane. The quality of the link is determined via the distance between the two elements and PF blocks of elements are formed from elements with a direct link or indirect link through common elements. The identification and reconstruction follows a particular order in each PF block. After each identification and reconstruction the corresponding PF elements (tracks and clusters) are removed from the PF block.

The muons are the first to be identified and reconstructed. These are reconstructed if their momenta are compatible with corresponding track only momenta. Then the electron and its corresponding brehmstrahung photons, are identified and reconstructed by using of the GSF tracking. At the same time, the energetic and isolated photons are identified as well. The remaining elements in the PF block are subjected to a cross identification of charged hadrons, neutral hadrons, and photons that arise from parton fragmentation, hadronisation, and decays in jets. The charged hadron candidate is made from the remaining candidates that have a charged particle track associated with them. Then the charged particle energy fraction is subtracted from the calibrated energy of the linked calorimeter clusters and the remaining energy is assigned to the neutral energy. Depending on the excess of neutral energy in the ECAL and HCAL clusters, a photon or a neutral hadron is assigned respectively. The pseudorapidity range of the inner tracker limits the information on the particles charge to $|\eta| < 2.4$. Outside this range a simplified identification is done for hadronic and electromagnetic candidates only.

4.3 Pileup mitigation and luminosity measurement

For the 8 TeV dataset, an average of about 21 pileup interactions happen per bunch cross section. For the dataset taken at 13 TeV, the number of pileup interactions increases to about 27 interactions per bunch crossing. These interactions are spread around the beam axis around the centre of the CMS coordinate system and follow a normal distribution with a standard deviation of about 5 cm [155]. The number of pileup interactions is estimated from the number of interaction vertices reconstructed from charged particle tracks, or from the instantaneous luminosity of the given bunch crossing with dedicated detectors and the inelastic proton-proton crossing. The luminosity of the CMS interaction point is estimated from measuring certain process rates with luminometers such as the pixel detector, HF calorimeter, and the pixel luminosity telescope [164]. The instantaneous luminosity from recorded process rate R is then determined as

$$\mathrm{L}dt = \frac{R dt}{\sigma_{\text{fid}}}, \tag{4.1}$$

where $\sigma_{\text{fid}} = \sigma \times A$ corresponds to the fiducial cross section recorded in the luminometer acceptance A which is determined using van der Meer scans [165]. The overall uncertainty on the luminosity measurement is estimated to be 2.5%.

The luminosity is used to infer to number of pileup interactions in data, which can be used to corrected the predefined pileup interactions in simulation. Then an event weight can be derived from the ratio of the distributions of pileup interactions in data and simulation. For 13 TeV collisions, the inelastic cross section is measured to be 71.3 ± 3.5 mb [166]. However a better agreement in data and simulation for the pileup sensitive variables, such as the number of primary vertices, is found with a lower cross section of 69.2 mb with an uncertainty of 4.6%.

4.4 Physics object reconstruction and identification

The particle flow objects are used for building physics objects that are used for analysis. These objects are jets, muons, electrons, photons, taus and missing transverse momentum $\vec{p}\!\!\!/_{\mathrm{T}}$. They are used to compute other quantities such as particle isolation and have extra requirements that are analysis dependent. In the following section, only the physics objects used throughout this thesis are discussed.

4.4.1 Muons

The muon candidates used for analysis in this thesis correspond to the tight working point (WP). The tight working point yields the most genuine muons and rejects falsely reconstructed ones. Detailed reports on the performance can be found in [168].

In order to reject objects wrongly reconstructed as muons from hadron showers that reach he muon system (punch-throughs), the global muon fit is required to include at least one valid hit in the muon chambers and for which at least two muon segments in two muon stations is present. Additionally, the muon tracks should have a global fit yielding a goodness-of-fit of $\chi^2/\mathrm{ndof} < 10$. The decay of muons in flight is suppressed by requiring at least one pixel hit in the muon track. Furthermore, a minimum of five hits in the tracker is required. Cosmic muons and muons originating from pileup interactions are rejected by constricting the distance of the muon with respect to the primary vertex by putting limits on $d_{\mathrm{x,y}} < 2$ mm and $d_{\mathrm{z}} < 5$ mm. Also muons according to the loose muon working point will be used in the thesis. These are either global muons or tracker muons reconstructed from the particle flow muon object. In Figure 4.2, the muon efficiencies for data and simulation is presented. These efficiencies are estimated from tag-and-probe methods that select $\mathrm{Z} \to \mu^-\mu^+$ and tag one muon that passes the identification criteria. The other muon is used as probe and one measures how many times it passes the identification criteria to get the efficiency. Overall, the efficiency is about 95-100%, with two drops due to the crack between the wheels of the DT system. The differences between data and simulation are corrected by applying p_{T} - and η-dependent scale factors ($\epsilon_{\mathrm{data}}/\epsilon_{\mathrm{MC}}$) to simulated events. In Table 4.1, the muon requirements for the muons used throughout this thesis are summarised.

In addition to the identification criteria, the muons are required to be spatially isolated from EM and hadronic activity. The lepton isolation is defined as estimating the total transverse energy of the particles emitted around the direction of the lepton by defining a cone of radius ΔR in $\eta\phi$ plane around the lepton direction. Then a summed energy is calculated from the charged hadrons (CH), neutral hadrons (NH), photons (γ), excluding the lepton itself. This sum is then corrected to remove the energy coming from pileup interactions. The relative isolation

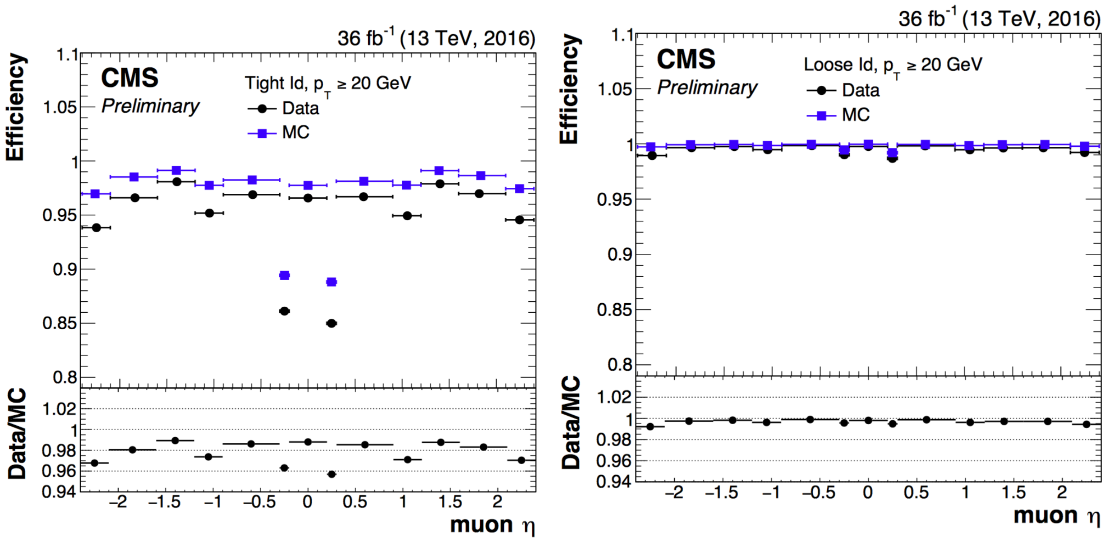

Figure 4.2: Comparison of the muon tight ID (left) and loose ID (right) efficiencies in data and simulation as a function of the pseudorapidity of the muon using the full 2016 dataset. Figure taken from [168].

for muons $\mathscr{I}_{\mu}$ is defined as [155]:

$$\mathscr{I}_{\mu} = \frac{\sum p_{\mathrm{T}}(\mathrm{CH}) + \max\left(0., \sum E_{\mathrm{T}}(\mathrm{NH}), \sum E_{\mathrm{T}}(\gamma) - 0.5 \times \sum E_{\mathrm{T}}(\mathrm{CH})\right)}{p_{\mathrm{T}}(\mu)}, \tag{4.2}$$

where a cone of $\Delta R = 0.4$ is adopted and the pileup mitigation is based on the $\Delta\beta$ correction. The $\Delta\beta$ correction estimates the pileup energy as half of the contribution coming from charged hadrons. For tight ID muons, this relative isolation should $\mathscr{I}_{\mu} < 0.15$, while for loose muons this should be $\mathscr{I}_{\mu} < 0.25$. In Figure 4.3, the isolation efficiencies as a function of the pseudo rapidities using the tag and probe method are shown for the tight muon ID. The efficiencies are 85-100% with a decline for low-p_{T} muons since they are most likely coming from hadronic or heavy flavour decays. The differences between data and simulation are accounted for by applying η- and p_{T} -dependent scale factors on the simulation.

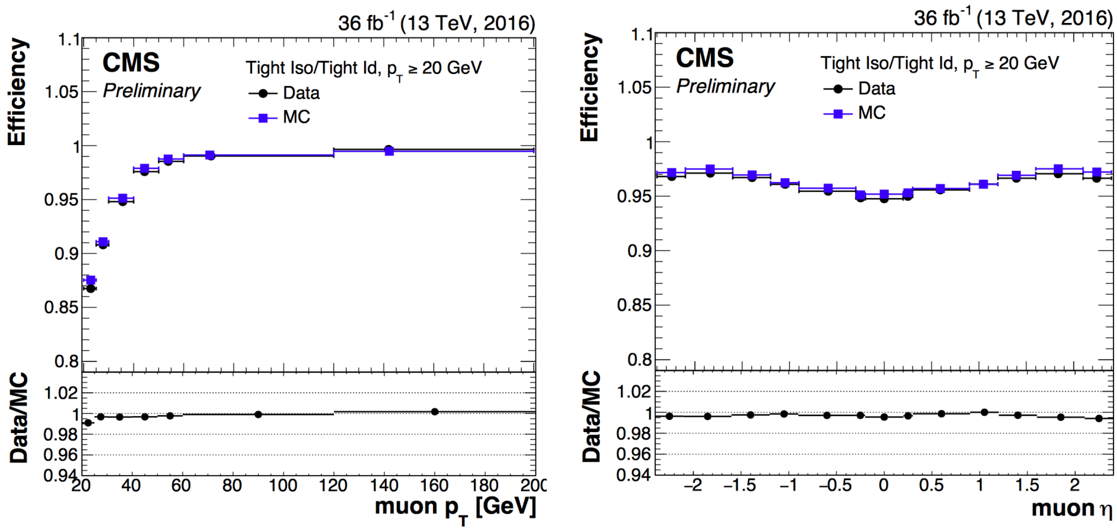

Figure 4.3: Comparison of the muon tight isolation requirement with the muon tight ID efficiencies in data and simulation as a function of the transverse momentum (left) or pseudorapidity (right) of the muon using the full 2016 dataset. Figure taken from [168].

Table 4.1: Muon requirements for the tight and loose working points, used throughout this thesis.

Property	Loose Muons	Tight Muons
Global muon or Tracker Muon	One or the other	Both
Particle Flow muon	Y	Y
$\chi^2/ndof$ of global muon track fit	N/A	< 10
Nb. of hit muon chambers	N/A	> 0
Nb. of muon stations contained in the segment	N/A	> 1
Size of the transverse impact parameter of the track wrt. to the PV	N/A	$d_{xy} < 2$ mm
Longitudinal distance wrt. the PV	N/A	$d_z < 5$ mm
Nb. of pixel hits	N/A	> 0
Nb. of tracker layers with hits	N/A	> 5
Relative Isolation	<0.25	<0.15

4.4.2 Electrons

The electrons candidates used correspond to the tight and veto working points. The study of the electron reconstruction and identification performance can be found in [161].

Starting from an electron PF candidate with a GSF track that is outside the barrel-endcap transition region ($1.4443 < |\eta| < 1.5660$), several requirements are set. The electrons from photon conversions are dismissed by requiring the electron track to have not have more than one (two or three) missing hit in the innermost layer for the tight (veto) working point. Additionally, a photon conversion veto is applied by testing if a pair of electron tracks is originating from a common displaced vertex. For the 8 TeV datasets more refined cuts are placed on the electron object using a multivariate analysis. For the 13 TeV dataset this is replaced with more refined cuts on the shower shape variables such as the difference in η or ϕ between the energy weighted supercluster position in the ECAL and the track direction in at the innermost tracker position ($\Delta\eta_{\mathrm{in}}$, $\Delta\phi_{\mathrm{in}}$), and the ECAL crystal based shower covariance in the η direction ($\sigma_{\eta\eta}$). These cuts also include energy related variables such as the absolute difference between the inverse electron energy measured in the ECAL and the inverse momentum measured in the tracker ($|1/E - 1/p|$), and the ratio of the energy measured in the HCAL and ECAL (H/E). Unlike the muon case, the identification criteria also contain requirements on the isolation of the electrons.

Similar to the muons, the electron relative isolation is determined from the sum of the particles in a cone around the electron itself. The cone radius used for electrons is $\Delta R = 0.3$ and a ρ correction for pileup mitigation is applied. For this correction, the expected pileup energy inside the isolation cone is estimated from the median density energy per area of pileup contamination (ρ), computed event by event, and the effective area ($A_{\mathrm{eff.}}$) [155]. This effective area is estimated from simulation and denotes the expected amount of neutral energy from pileup interactions per ρ within the isolation cone as a function of the pseudo rapidity of the associated ECAL superclusters Table 4.2 shows the values used for 13 TeV data. The relative electron isolation $\mathscr{I}_{\mathrm{e}}$ is calculated as

$$\mathscr{I}_{\mathrm{e}} = \frac{\sum p_{\mathrm{T}}(\mathrm{CH}) + \max\left(0., \sum E_{\mathrm{T}}(\mathrm{NH}), \sum E_{\mathrm{T}}(\gamma) - \rho \times A_{\mathrm{eff.}}\right)}{p_{\mathrm{T}}(\mathrm{e})}. \tag{4.3}$$

The efficiency of electron identification is estimated from $\mathrm{Z} \to \mathrm{e}^{-}\mathrm{e}^{+}$ events via the tag-and-probe method and is shown in Figure 4.4 for the tight working point. The efficiencies reach $95 - 100\%$. The difference between data and simulation are corrected by dedicated p_{T}- and η dependent scale factors as well.

Table 4.2: The effective areas $A_{\mathrm{eff.}}$ used for the electron relative isolation [169].

η region	$A_{\mathrm{eff.}}$
$0 < \|\eta\| < 0.1752$	0.1703
$1.0 < \|\eta\| < 0.1479$	0.1715
$1.479 < \|\eta\| < 2.0$	0.1213
$2.0 < \|\eta\| < 2.2$	0.1230
$2.2 < \|\eta\| < 2.3$	0.1635
$2.3 < \|\eta\| < 2.4$	0.1937
$2.4 < \|\eta\| < 2.5$	0.2393

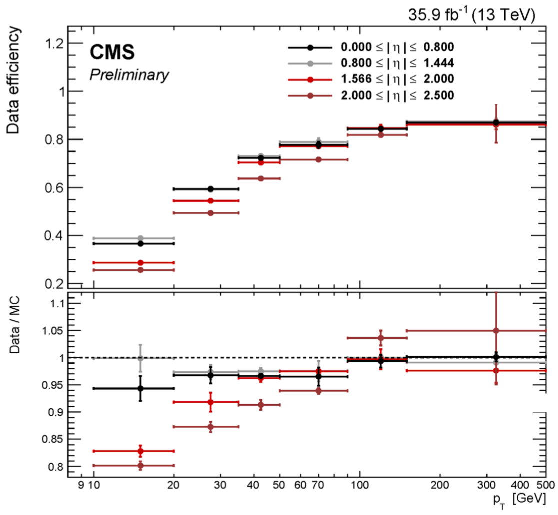

Figure 4.4: Electron identification efficiency as function of the electron transverse momentum from the full 2016 dataset. Figure taken from [161].

4.4.3 Jets

Jets are reconstructed from all reconstructed particles without the charged hadrons associated to pileup vertices (PF+CHS jets). The clustering is done via the anti $-\mathrm{k_T}$ algorithm [170] with a radius parameter for the cone size of the resulting jet of $R = 0.5$ for 8 TeV data and $R = 0.4$ for the more boosted 13 TeV dataset. The initial step of the anti $-\mathrm{k_T}$ algorithm considers all candidates as protojets and starts to calculate the distances for protojets i and j as

$$\begin{aligned} d_{\mathrm{ij}} &= \min\left(\frac{1}{p_{\mathrm{T,i}}^2}, \frac{1}{p_{\mathrm{T,j}}^2}\right), \\ d_{\mathrm{i}} &= \frac{1}{p_{\mathrm{T,i}}^2}. \end{aligned} \tag{4.4}$$

Table 4.3: Electron requirements used in this analysis. The requirements are set in the barrel ($|\eta_{supercluster}| \leq 1.479$) and the endcaps ($|\eta_{supercluster}| > 1.479$).

Properties	$\lvert\eta_{supercluster}\rvert \leq 1.479$		$\lvert\eta_{supercluster}\rvert > 1.479$	
	Veto electron	Tight electron	Veto electron	Tight electron
$\sigma_{\eta\eta}$	< 0.0115	< 0.00998	< 0.037	< 0.0292
$\lvert\Delta\eta_{\text{in}}\rvert$	< 0.00749	< 0.00308	< 0.00895	< 0.00605
$\lvert\Delta\phi_{\text{in}}\rvert$	< 0.228	< 0.0816	< 0.213	< 0.0394
H/E	< 0.356	< 0.0414	< 0.211	< 0.0641
relative isolation	< 0.175	< 0.0588	< 0.159	< 0.0571
$\lvert 1/E - 1/p\rvert$	< 0.299 GeV^{-1}	< 0.0129 GeV^{-1}	< 0.15 GeV^{-1}	< 0.0129 GeV^{-1}
expected missing inner hits	≤ 2	≤ 1	≤ 3	≤ 1
pass conversion veto	Y	Y	Y	Y

For each iteration the two distances are calculated. When $d_{\text{ij}} < d_{\text{i}}$, the two protojets are merged and their four momentum is summed. If d_{i} is the smallest distance, the protojet is renamed as final jet and ignored in the subsequent steps. More information about the jet algorithm performance can be found in [171].

The jets used for the analysis discussed in this thesis uses the loose identification working point given. The criteria on the constituents of the jets are given in Table 4.4. These requirements find their origin on the assumption that a proper jet originating from the hadronisation of a quark or gluon consists of multiple PF particles and types. The jet should consists of more than one constituent and the neutral hadron fraction and neutral EM energy fractions should be less than 99%. For the jets within the tracker acceptance ($|\eta| < 2.4$), at least one constituent has to be a charged hadron resulting in a charged hadron energy fraction above 0%. Additionally the charged EM energy fraction should be less than 99%. On top of these requirements, objects that are labelled as jets and found in vicinity of any isolated lepton, $\Delta R < 0.3$, are removed from the jet collection in that event.

The energy of the reconstructed jets deviate from the energies of the corresponding jets clustered from the hadronisation products of true partons from simulations due to non linear subdetetector response and efficiencies. The jet energy corrections (JEC) calibrate the jets in order to have the correct energy scale and resolution. Jet energy scale corrections (JES) are determined as a function of pseudorapidity ant the transverse momentum from data and simulated events by combining several channels and methods. This is extensively described in [172]. These corrections account for the effects of pileup, the uniformity of the detector response, and residual data-simulation jet energy scale differences. Furthermore, the jet energy resolution (JER) is measured in data and simulation as function of pileup, jet size and jet flavour. A detailed understanding of both the energy scale and the transverse momentum resolution

Table 4.4: Jet criteria used throughout the thesis. The last three requirements are only for jets within the tracker acceptance.

Properties	Loose Jet ID
Neutral hadron fraction	< 0.99
Neutral EM fraction	< 0.99
Number of constituents	> 1
Charged hadron fraction	> 0
Charged multiplicity	> 0
Charged EM fraction	< 0.99

of the jets is crucial for many physics analysis, and these are commonly the main source of systematic uncertainty. The performance of the jet energy corrections for the 13 TeV dataset can be found in [173].

The JEC are factorised and subsequently correct for the offset energy due to pileup, the detector response to hadrons, and residual differences between data and simulation as a function of the jet pseudorapidity and transverse momentum. The consecutive steps of JEC are shown in Figure 4.5. The off set corrections remove the dependence of the jet energy response of additional pileup

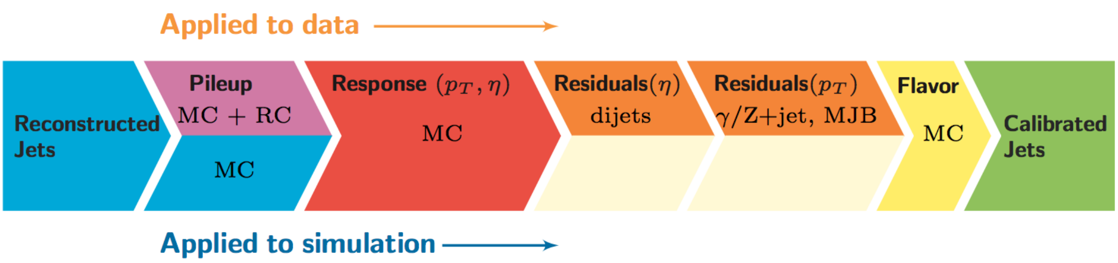

Figure 4.5: The sequence of the JEC for data and simulations The corrections marked with MC are derived from simulation studies, while RC stands for random cone, and MJB for the analysis of multi-jet events. Figure taken from [172].

activity. It is based on the jet area method, which uses the effective area of the jets multiplied by the average density in the event to calculated the offset energy to be subtracted of the jets. The correction factors are derived by comparing the jet response with and without pileup events overlaid. The residual differences between data and detector simulation are determined using the random cone method (RC). For this method, many jets are reconstructed in each event by clustering particles through placing random cones. This provides a mapping of the $\eta\phi$-space and the average p_T of those jets gives the average energy offset due to pileup [172]. The next level of corrections have as goal to have an uniform energy response independent of the transverse momentum or pseudorapidity of the jet. These corrections are determined from simulated events by matching the reconstructed to true particle jets and comparing there momenta. The residual corrections between data and simulation are determined by comparing the transverse momentum balance in various types of events (multi-jet, Z + jets, and γ + jets), using a reference jet in the barrel region. The jet flavour corrections are optional and not used for this thesis. More information on the jet flavour corrections can be found in [172]. For jets with a transverse momentum above 30 GeV, the uncertainties from the various corrections are 3-5% for the 13 TeV dataset [173].

After applying JEC, the transverse momentum resolution of the jet is extracted from data and simulated events. There are two methods used to rescale the reconstructed four momentum chosen based on whether or not the simulated jet can be matched to a true jet in simulation. The factors are defined as

$$\begin{aligned} c_{\text{matched}} &= 1 + \frac{p_{\text{T}}^{\text{reco.}} - p_{\text{T}}^{\text{true}}}{p_{\text{T}}^{\text{reco.}}}\left(s_{\text{JER}} - 1\right), \\ c_{\text{unmatched}} &= 1 + \text{N}(0, \sigma_{\text{JER}})\sqrt{\max\left(s_{\text{JER}}^2 - 1, 0\right)}, \end{aligned} \tag{4.5}$$

where $\text{N}(0, \sigma_{\text{JER}})$ denotes a sample value from a normal distribution centred at zero with as standard deviation the relative resolution in simulation σ_{JER}, and s_{JER} the η-dependent resolution scale factors. These scale factors are derived from data from di-jet or γ + jets events and analysing the p_{T} balance. The resolution scale factors (data/simulation) are found to be 1.1-1.2 except for the transition regions around $|\eta| = 3$ and $|\eta| = 1.4$ [173] and given in Table 4.5.

Table 4.5: Jet energy scale factors in bins of η with uncertainty

$\lvert\eta\rvert$	SF	Uncertainty (±)
0-0.5	1.109	0.008
0.5-0.8	1.138	0.013
0.8-1.1	1.114	0.013
1.1-1.3	1.123	0.024
1.3-1.7	1.084	0.011
1.7-1.9	1.082	0.035
1.9-2.1	1.140	0.047
2.1-2.3	1.067	0.053
2.3-2.5	1.177	0.041

4.4.4 Jets from b fragmentation

Jets originating from the hadronisation of bottom quarks can be discriminated from jets from gluons and light-flavour quarks as well as charm quark fragmentation through the use of b-tagging. There are a multitude of algorithms developed within CMS to perform b-tagging [174, 175] on jets that fall within the pseudorapidity acceptance of the trackers. These algorithms exploit the properties of the b quark to identify the jets formed by its fragmentation. These hadrons have relative large masses, long lifetimes and daughter particles with hard momentum spectra. Additionally, their semi-leptonic decays can be exploited as well. To use b-jet identification in an analysis, one needs to know its efficiency and misidentification probability. In general these are function of the pseudorapidity and transverse momentum of the considered jet. Their performances are directly measured from data by use of b-jet enriched jet samples (multi-jet or top-quark decays).

This thesis uses b-jets identified by the Combined Secondary Vertex version 2 (CSVv2) algorithm [174]. This algorithm combines secondary vertices together with track based lifetime information by use of a multivariate technique. The secondary vertex is reconstructed from displaced tracks within a jet, as illustrated in Figure 4.6. The final state b quark is encapsulated in a B meson (e;g. $B^{\pm}$, B_0, B_S) after the hadronisation. This B meson has relatively long lifetime and can travel a measurable distance from the primary vertex before decaying[1]. After reconstruction, the secondary vertices are required to be in accordance with the B meson hypothesis bases an the amount of shared tracks with the primary vertex, the invariant vertex mass to reject kaon decays, and the direction of the tracks compared to the jet axis.

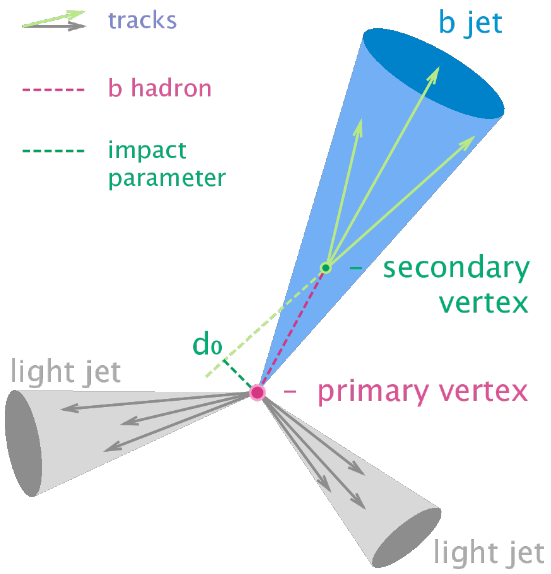

Figure 4.6: Sketch showing the common principle of the identification of b-jets. Figure taken from [176]

The b-tagging algorithm performances are evaluated taking into account two cases: discrimination of b-tagged jets originating from charm quarks, and discrimination of b-tagged jets against jets coming from gluons or light (u, d, s) quarks.In Figure 4.7, the misidentification probabilities for different b-tagging algorithms within CMS are shown. Based on the misidentification probabilities for a certain threshold on the CSVv2 discriminator, different working

[1] For example, $B^{\pm}$ mesons have a lifetime of about 1.6 ps [6] and travel 4-9 mm before decaying if their momenta is 40-100 GeV.

points (WP) are defined. These are shown in Table 4.6. The analysis presented in this thesis uses the loose working point which has an average efficiency of 81% and a misidentification rate of 10%.

NOTE: Find reason why I am not using cMVA, omdat CVSv2 op ttbar events is gemeten en cMVA op multijet?

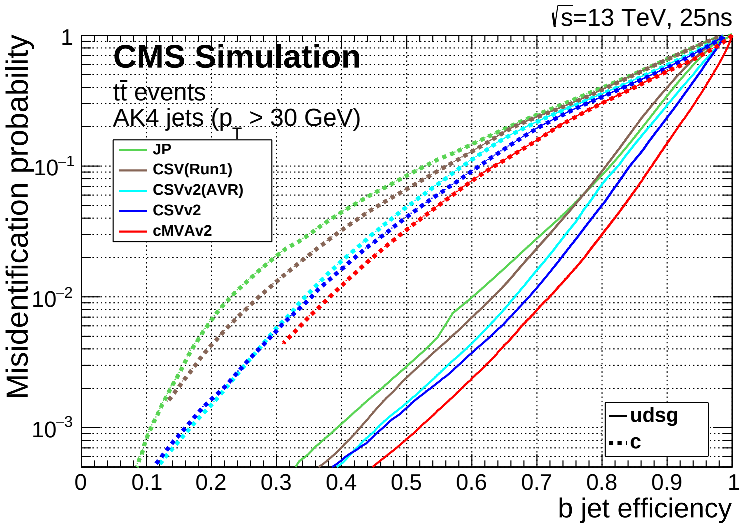

Figure 4.7: Misidentification probabilities of various b-tagging algorithm in simulation. Figure taken from [175].

Table 4.6: Working points used for tagging jets as coming from b quarks for the CSVv2 discriminant.

WP	CSVv2 discr cut	b-tag eff.	misid. prob.
Loose (L)	> 0.5426	$\approx 81\%$	$\approx 10\%$
Medium (M)	> 0.8484	$\approx 66\%$	$\approx 1\%$
Tight (T)	> 0.9535	$\approx 46\%$	$\approx 0.1\%$

The efficiency of tagging a jet as coming from a bottom quark in simulation typically deviates somewhat from data. Efficiency scale factors $\epsilon_b^{data}/\epsilon_b^{MC}$ are derived from data to account for those differences. These scale factors are η-, p_T-, and flavour dependent, where the flavour of the jet is determined from matched generated hadrons. For cut based analyses these scale factors are applied to the b-tagging efficiencies and mistag rates according to the chosen working point [175]. For shape based analysis however, such as the one presented in this thesis, the scale factor are applied on the distribution of the b-tagging discriminator. This is the so-called IterativeFit method [177]. It uses a tag and probe method to measure the scale factors for both b, c, and light flavoured jets simultaneously. The scale factors to account for the differences in simulation and data for the probe jet are determined iteratively to account for the impact of the b-, c-flavour, and light flavour scale factors on eachother. In a fist step, no scale factors are applied. Then the scale factor is measured by applying the scale factors of the previous iteration to simulation until the scale factors become stable. Throughout the procedure, the scale factor for charm jets are set unity with an uncertainty that is twice the one of the b scale factor. The scale factors obtained in η-, p_{T} -, and CSVv2 discriminant values are determined with the bin content N of the considered (η,p_{T} ,discriminant) bin as

$$
\begin{aligned}
\mathrm{SF}_{\mathrm{b}} &= \frac{N_{\mathrm{b}}^{\mathrm{data}} - N_{\mathrm{b}}^{\mathrm{MC}}}{N_{\mathrm{b}}^{\mathrm{MC}}}, \\
\mathrm{SF}_{\mathrm{g,u,d,s}} &= \frac{N_{\mathrm{g,u,d,s}}^{\mathrm{data}} - N_{\mathrm{g,u,d,s}}^{\mathrm{MC}}}{N_{\mathrm{g,u,d,s}}^{\mathrm{MC}}}, \\
\mathrm{SF}_{\mathrm{c}} &= 1.
\end{aligned}
\tag{4.6}
$$

The uncertainties related to the IterativeFit method cover possible shape discrepancies between data and simulation. The uncertainty coming from the purity of the sample is subdivided into two uncorrelated uncertainties based on the purity of the light flavoured (lf) and heavy flavoured (hf) jet contributions in the sample. Furthermore, the jet energy scale results in jets migrating from one p_{T} bin to an other, having an influence on bin dependent scale factors. The statistical fluctuations of the limited amount of entries in each bin are also accounted for and have an influence on the scale factor uncertainties. These have four uncorrelated sources: two for heavy flavour and two for light flavour jets. Since the uncertainty on the scale factors for the jets originating from a charm quark (cf) is determined from the uncertainty on the b scale factors resulting in two independent uncertainties [177].

4.4.5 Missing transverse energy

The missing transverse momentum $\vec{\not{p}}_{\mathrm{T}}$ and energy $E_{\mathrm{T}}^{\mathrm{miss}}$ resulting from particles that do not interact with the detector material, are calculated to balance the vectorial sum of the transverse momenta of all particles:

$$
\begin{aligned}
E_{\mathrm{T}} &= \left|\vec{\not{p}}_{\mathrm{T}}\right|, \\
\vec{\not{p}}_{\mathrm{T}} &= -\sum_{\mathrm{i}=1}^{\mathrm{N_{particles}}} \vec{p}_{\mathrm{T,i}}.
\end{aligned}
\tag{4.7}
$$

The z-component can not be calculated from the momentum imbalance since the boost along the z-axis, determined by the momentum fraction, can not be reconstructed.

The missing transverse energy is influenced by the minimum thresholds in calorimeters, the inefficiencies in the tracker, and the non-linear response of the calorimeter to hadronic particles. The bias is reduced by correcting the transverse momentum of the jets too particle jet p_{T} via the JEC and propagating it to the missing transverse momentum taking into account the energy

$$
\begin{aligned}
\vec{\not{p}}_{\mathrm{T}}^{\mathrm{corr}} &= -\sum_{\mathrm{i}=1}^{\mathrm{N_{jets}}} \vec{p}_{\mathrm{T,i}}^{\mathrm{corr.}} - \sum_{\mathrm{i}=1}^{\mathrm{N_{unclustered}}} \vec{p}_{\mathrm{T,i}}^{\mathrm{raw}}, \\
\vec{\not{p}}_{\mathrm{T}}^{\mathrm{corr}} &= \vec{\not{p}}_{\mathrm{T}}^{\mathrm{raw}} - \sum_{\mathrm{i}=1}^{\mathrm{N_{jets}}} \left(\vec{p}_{\mathrm{T,i}}^{\mathrm{JEC}} - \vec{p}_{\mathrm{T,i}}^{\mathrm{PU-only}}\right).
\end{aligned}
\tag{4.8}
$$

The $\vec{p}_{\mathrm{T,i}}^{\mathrm{PU-only}}$ denotes the transverse momentum of the jet, where only the pileup related corrections are applied. The performance of the missing transverse energy reconstruction can be found in [178].

4.5 Summary of corrections

Throughout the chapter several corrections are introduced to improve the agreement between data and simulation. These corrections are sources of systematic uncertainties for the analysis presented in this thesis. Therefore a summary of the corrections and their associated uncertainties is provided.

Lepton scale factors The systematic uncertainty on the lepton scale factors consist of three sources: identification, isolation and tracking. The applied scale factors are varied independently within one standard deviation of their measured uncertainties to account for their systematic impact on the measurements.

Jet energy corrections The momenta of the reconstructed jets are corrected to match the expected true energy derived from the hadronisation products of partons in simulation. Furthermore, residual corrections and smearing is applied to match the overall energy scale and resolution for simulation and data. These corrections are also propagated to the missing transverse energy. The systematic uncertainties due to these scale factors are estimated by varying them within their uncertainties and repeating the measurements with recalibrated jets and missing transverse energy.

CSVv2 discriminant shape reweighting There are three sources of uncertainty contributing to the measurement of the scale factors: statistical uncertainties, jet energy scale and the purity of the sample. The jet energy scale uncertainty is 100% correlated to the jet energy uncertainties and is evaluated simultaneously. The uncertainty coming from the purity of the sample is subdivided into two uncorrelated uncertainties based on the purity of the light flavoured (lf) and heavy flavoured (hf) jet contributions in the sample. A one sigma shift in each of the two purity contributions corresponds to a higher/lower contribution in the purity of the considered flavours. The statistical uncertainties has four uncorrelated sources, two for heavy flavour and two for light flavour jets. One of the uncertainties correspond to the shift consistent with the statistical uncertainties of the sample, while the other is propagated in a way that the upper and lower ends of the distribution are affected with respect to the centre of the distribution. The uncertainty on the charm jet scale factors (cf) is obtained from the uncertainty on the heavy flavour scale factors, doubling it in size and constructing two nuisance parameters to control the charm flavour scale factors and treating them as independent uncertainties.

Pileup Varying the minimum bias cross section, used to calculate the pileup distribution by $\pm 4.6\%$, results in a systematic shift in the pileup distribution. The uncertainty is estimated by recalculating the pileup weights to the distributions associated to the minimum bias cross sections.

Luminosity The luminosity is measured with a global uncertainty of 2.5%, affecting the expected number of events.

Event selection and categorisation 5

A basic event selection is made for selecting signal like events. The necessary event requirement are discussed in Section 5.2.

The analysis uses signal and background regions to constrain the huge SM background compared to the expected signal. Section 5.4 discusses each region that is entering the analysis. On top of the use of background estimation from control regions, backgrounds that have prompt leptons contaminated by real leptons either from decays of tau leptons or from hadronized mesons or baryons (collectively commonly referred as “non-prompt leptons") as well as by hadrons or jets misidentified as leptons[1] are evaluated with a data-driven method discussed in Section 5.3.

5.1 Baseline event selection and filters

The CMS collaboration recorded in the course of 2016 proton at 13 TeV collisions data with a total recorded integrated luminosity of $35.9 \pm 2.5\%$ fb^{-1}. The baseline event selection has a goal to substantially reject SM background events, whilst maintaining a high signal efficiency. In this analysis a search is performed in a final state made up of a Z boson and a top quark, associated or not with a jet, in the leptonic decay of the Z boson and the top quark. The leading order Feynman diagrams can be seen in Figure 5.1.

NOTE: adapt to leptonic decay

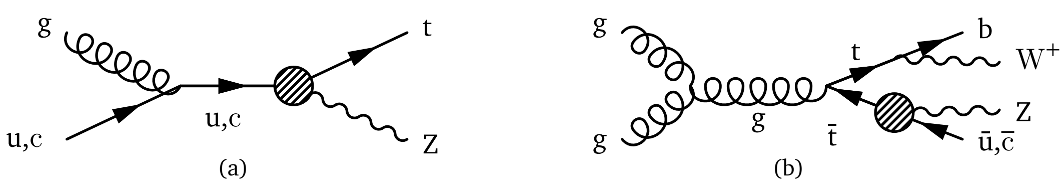

Figure 5.1: Feynman diagrams for the tZq FCNC interaction with a fully leptonic decay, where the FCNC interaction is indicated with the shaded dot. (a) Single top production through an FCNC interaction. (b) Top pair production with an FCNC induced decay.

[1] These two classes of contamination will be referred to as not prompt-lepton (NPL) samples.

The signal considers both the single top quark FCNC (tZ in the final state) and the top quark pair FCNC (tZq in the final state) events. Their final state signatures consist of three leptons, considering electrons or muons in our analysis, and a jet originating from a b quark. For FCNC tZq, there is an additional up or charm jet. Leptons from tau decays are not vetoed and are entering the analysis. Four different lepton channels based on lepton flavour are considered (eee, eeμ, e$\mu\mu$, and $\mu\mu\mu$).

The CMS trigger system, described in Section 2.2.3, filters out the main of the collision events from uninteresting processes and dedicated trigger paths are define to single out the events with our required detector signature. The trigger paths are chosen based on on-line triggering objects with at least one muon (M), at least one electron (E), at least two muons (MM), at least two electrons (EE), at least one muon and an electron (ME), at least three muons (MMM), at least three electrons (EEE), at least two muons and one electron (MME), or at least two electrons and one muon (EEM). For the MC simulation a simple *or* of all triggers is taken and the event is taken if it passes one of the trigger paths. For data however, double counting of the same event has to be taken into account and a procedure to avoid double counting has been put into place. It consists of vetoing in a given dataset the events that are already selected in another, as given in Table 5.1.

Table 5.1: Trigger logic used to select data events in order to avoid double counting

Dataset	Trigger Logic
eμ	EM || EEM || MME
$\mu\mu$	(MM || MMM) && !(EM || EEM || MME)
ee	(EE || EEE) && !(MM || MMM) && !(EM || EEM || MME)
single μ	M && !(EE || EEE) && !(MM || MMM) && !(EM || EEM || MME)
single e	E && !M && !(EE || EEE) && !(MM || MMM) && !(EM || EEM || MME)

This trigger selection strategy is to allow the maximum statistics on the signal region since it does not discard events from any dataset. For the single lepton triggers, at least one electron (muon) with a transverse momentum p_{T} higher than 32 GeV (24 GeV) is required. The dilepton triggers require an electron (muon) with $p_{\mathrm{T}} > 23$ GeV and a muon (electron) with $p_{\mathrm{T}} > 8$ GeV, or an electron (muon) with $p_{\mathrm{T}} > 23$ GeV (17 GeV) and an electron (muon) with $p_{\mathrm{T}} > 12$ GeV (8 GeV). Events collected by the trilepton triggers require an electron (muon) with $p_{\mathrm{T}} > 16$ GeV (12 GeV), a second electron (muon) of $p_{\mathrm{T}} > 12$ GeV (10 GeV), and a third electron (muon) with $p_{\mathrm{T}} > 8$ GeV (5 GeV). The mixed trilepton trigger events require two electrons (muons) with $p_{\mathrm{T}} > 12$ GeV (9 GeV) and a third muon (electron) with $p_{\mathrm{T}} > 8$ GeV (9 GeV). The HLT trigger paths used in data and simulation are summarised in Table 5.2.

In order to ensure a full trigger efficiency, the offline p_{T} treshodls are siet higher than the on-lon etrigger thresholds. Selected electrons (muons) are required to have $p_{\mathrm{T}} > 35$ (30) GeV and $|\eta| < 2.1(2.4)$. A quantity for evaluating lepton isolation is calculated as the summed energy of

Table 5.2: HLT trigger paths used to select data and simulation events.

Trigger path name	Trigger type
HLT_Mu23_TrkIsoVVL_Ele8_CaloIdL_TrackIdL_IsoVL_v	ME
HLT_Mu23_TrkIsoVVL_Ele8_CaloIdL_TrackIdL_IsoVL_DZ_v	ME
HLT_Mu8_TrkIsoVVL_Ele23_CaloIdL_TrackIdL_IsoVL_v	ME
HLT_Mu8_TrkIsoVVL_Ele23_CaloIdL_TrackIdL_IsoVL_DZ_v	ME
HLT_DiMu9_Ele9_CaloIdL_TrackIdL_v	MME
HLT_Mu8_DiEle12_CaloIdL_TrackIdL_v	EEM
HLT_IsoMu24_v	M
HLT_IsoTkMu24_v	M
HLT_Ele32_eta2p1_WPTight_Gsf_v	E
HLT_Mu17_TrkIsoVVL_Mu8_TrkIsoVVL_v	MM
HLT_Mu17_TrkIsoVVL_TkMu8_TrkIsoVVL_v	MM
HLT_Mu17_TrkIsoVVL_Mu8_TrkIsoVVL_DZ_v	MM
HLT_Mu17_TrkIsoVVL_TkMu8_TrkIsoVVL_DZ_v	MM
HLT_TripleMu_12_10_5_v	MMM
HLT_Ele23_Ele12_CaloIdL_TrackIdL_IsoVL_DZ_v	EE
HLT_Ele16_Ele12_Ele8_CaloIdL_TrackIdL_v	EEE

all particles (charged hadrons, neutral hadrons, photons) in a cone of radius $\Delta R < 0.3$ (0.4) around the electron (muon), excluding the electron (muon) itself, and divided by the lepton p_T . An electron candidate is selected if this isolation quantity is below 0.059 in the barrel region and below 0.057 in the end caps. A muon candidate is selected if this isolation quantity is below 0.15. Other lepton selection criteria are applied in analysis based on the values of various quantities determined during the reconstruction, such as number of missing track hits or the electromagnetic shower created by the particles. These are given in Section 4.4.1 (Table 4.1) and Section 4.4.2 (Table 4.3). The trigger efficiency estimation is described in Section 5.1.2.

The samples are pre-selected off-line to ensure that all reconstructed particles considered for the analysis are corresponding to a proton interaction and that signals from beam halo particles as well as detector noise is removed. For this reason, several filters are used. These are described in Section 5.1.1.

On top of leptons, jets and missing transverse energy are expected from the signal signature. The jets are reconstructed using the anti $-\mathrm{k_T}$ algorithm with a distance parameter of 0.4 using the particle flow particles that are not identified as isolated leptons as input. The jet momentum is determined as the vectorial sum of the particles contained in the jet. Additional selection criteria are applied to each event to remove spurious jet-like features originating from isolated noise patterns in certain hadron calorimeter regions. More information about the jets used for this analysis can be found in Section 4.4.3. The jets are calibrated in simulation and in data separately, accounting for deposits from pileup and the non-linear detector response. Calibrated jets with $p_{\mathrm{T}} > 30$ GeV and $|\eta| < 2.4$ are selected. A selected jet may still overlap with the selected leptons leading to a double-counting. To prevent such cases, jets that are found within a cone of $R = 0.3$ around any of the signal electrons (muons) are removed from the set of selected jets.

The jets originating from b quarks are tagged using the CSVv2 algorithm, which combines the information of displaced tracks with information of secondary vertices associated with the jet using a multivariate technique. The jets are tagged as a jet coming from a b quark (b-tagged) if the CSVv2 discriminator is above a certain threshold. This analysis uses a threshold that results in an average b-tagging efficiency of 81% and a misidentification rate of 10%. More information about b-tagging can be found in Section 4.4.4.

The missing transverse momentum vector $\vec{p}\!\!\!/_{\mathrm{T}}$ is defined as the projection on the plane perpendicular to the beams of the negative vector sum of the momenta of all reconstructed particles in an event. Its magnitude is denoted by $E_{\mathrm{T}}^{\mathrm{miss}}$ as shown in Section 4.4.5. Its longitudinal component is calculated by limiting the lepton + neutrino to the W boson mass. In case two solutions arise, the mass closest to the known top quark mass is used. The events and their corresponding object collections reconstructed using the reconstruction criteria described in Section 4.1, are used as input for the analysis. Further requirements on the momenta and the pseudo rapidities are made to fulfil the trigger requirements and reconstruction algorithms.

5.1.1 Event cleaning

Some events arising from instrumental noise and beam backgrounds might end up in the data [178, 179]. Spurious deposits may appear in the ECAL from non collision origins such as beam halo particles, or from particles striking the sensors in the ECAL photo detectors. Conjointly, dead ECAL cells can cause artificial missing transverse energy. The HCAL can cause spurious energy from particle interactions with the light guides and the photomultiplier tubes of the HF, as well as noisy hybrid photo diodes. In CMS, different algorithms, so-called filters, are developed to identify and suppress these events.

The ECAL electronics noise and spurious signals from particle interactions with photo detectors are mostly removed via topological and timings based selection using ECAL information only. THe remaining effects such as anomalously high energy crystals and the lack of information for channels due to inefficiencies in the read out are removed through dedicated events filters. Five ECAL endcap supercrystal have been identified for giving anomalously high energies due to high amplitude pulses in several channels at once, and are masked. Furthermore, the crystal read out from a small amount of ECAL towers is not available. However, their trigger primitive information is still available making it possible to estimate the magnitude of unmeasured energy and when the value is too large, the event is filtered out.

The machine induced particles, via beam-gas / beam-pipe/... interactions, that are flying with the beam affect the physics analysis. They leave a calorimeter deposit along a line at constant ϕ in the calorimeter, and interactions in the CSCs will often line up with this deposit. This can be seen in Figure 5.2. Therefore, events containing such beam halo particles are removed from the selection with the CSC Beam Halo Filter. This filter uses information related to the geometric quantities, energy deposits, and timing signatures. For 2016, the filter rejects 85% in a halo-enriched sample, whereas the mistag probability determined from simulation if found te be less than 0.01%.

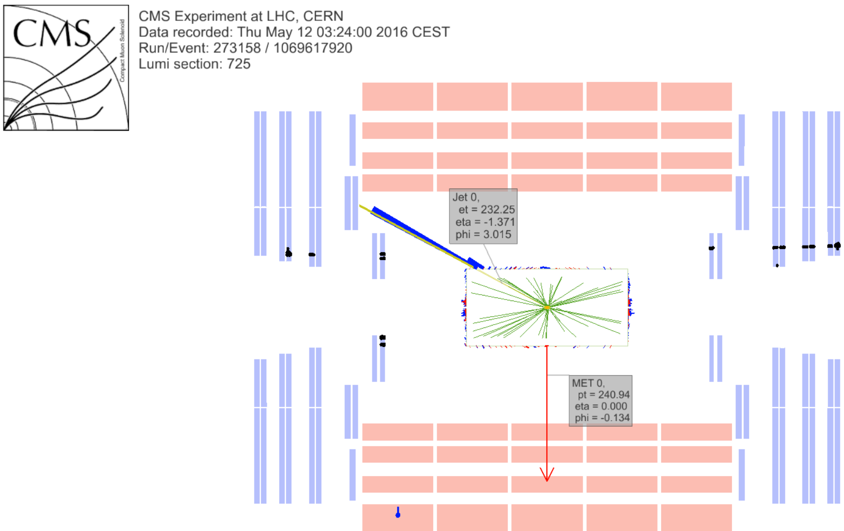

Figure 5.2: Event display of a beam halo event with collinear hits in the CSC (black), missing transverse energy of 250 GeV and a jet of 232 GeV. The hadronic deposit is spread in η, but narrow in ϕ. Figure taken from [178].

Furthermore, there is anomalous high missing transverse energy coming from low quality muons that lead to high-p_T tracks, but are considered not good by the particle flow algorithm. These low quality tracks will be mislabelled as charged hadrons and will therefore be used in the calculation of the missing transverse energy. By investigation the purity of the reconstructed tracks and the relative transverse momentum error of the muons, these events can be filtered out.

Supplementary to previous filters, only events with where the first primary vertex is a well reconstructed primary vertex are selected. The reconstructed primary vertex should have at least five degrees of freedom, the longitudinal distance from the beam spot is maximally 24 cm ($d_z < 24$ cm), and the transversal distance from the beam spot is maximally 2 cm ($d_{xy} < 2$ cm).

5.1.2 Estimation of the trigger efficiency

The trigger efficiency in data is estimated using a data sample collected using unprescaled $E_{\mathrm{T}}^{\mathrm{miss}}$ triggers. These allow events with a missing transverse energy higher then 110 GeV(120 GeV) and that the scalar sum of the transverse momenta of the reconstructed PF jets $H_{\mathrm{T}}^{\mathrm{trig.}}$ is at least 300 GeV (120 GeV), or a calorimeter/PF $E_{\mathrm{T}}^{\mathrm{miss}}$ higher than 200 GeV/300 GeV. For an HB-HE cleaned event the PF missing transverse energy threshold is lowered to 170 GeV. These trigger paths are summarised in Table 5.3 and chosen to be completely uncorrelated with the lepton triggers given in Table 5.2.

Table 5.3: Unprescaled $E_{\mathrm{T}}^{\mathrm{miss}}$ HLT trigger paths for estimating the trigger efficiency. An *or* of the triggers is used to select events.

Trigger path	Requirement
HLT_PFHT300_PFMET110_v*	PF $E_{\mathrm{T}}^{\mathrm{miss}} > 110$ GeV, PF $H_{\mathrm{T}}^{\mathrm{trig.}} > 300$ GeV
HLT_MET200_v*	calorimeter $E_{\mathrm{T}}^{\mathrm{miss}} > 200$ GeV
HLT_PFMET300_v*	PF $E_{\mathrm{T}}^{\mathrm{miss}} > 300$ GeV
HLT_PFMET120_PFHT120_IDTight_v*	PF $E_{\mathrm{T}}^{\mathrm{miss}} > 120$ GeV, PF $H_{\mathrm{T}}^{\mathrm{trig.,tightWP}} > 120$ GeV
HLT_PFMET170_HBHECleaned_v*	PF $E_{\mathrm{T}}^{\mathrm{miss}} > 170$ GeV, cleaned for HB/HE anomalous signals

The studied simulation sample is the main background, WZ+jets, with all corrections applied. For this study, the events passing a three lepton cut and at least one jet are being used. The corresponding efficiencies are then calculated as

$$\epsilon_{data} = \frac{\text{Nb. of events passing lepton and MET triggers}}{\text{Nb. of events passing MET triggers}} \tag{5.1}$$

$$\epsilon_{MC} = \frac{\text{Nb. of events passing lepton triggers}}{\text{Nb. of total events}} \tag{5.2}$$

The resulting efficiencies and scale factors can be found in Table 5.4, where the scale factors are defined as

$$SF = \frac{\epsilon_{data}}{\epsilon_{MC}}. \tag{5.3}$$

More detailed scale factors and efficiencies can be found in Appendix A.

Table 5.4: Trigger scale factors for each channel, after three lepton + jets cut, in the Z mass window. by counting number of events.

all	μμμ	eee	eeμ	eμμ
1.0000	1.0000	0.9541	1.0006	1.0004%

The trigger efficiencies are also measured in function of the p_{T} of the leptons for which the distributions can be found in Appendix A. The resulting scale factors in can be found in Figure Figure 5.3. The trigger efficiencies are measured to be nearly 100% for both simulation and data. The results are dominated by statistics and assigning a large uncertainty to the trigger efficiency based on the dataset collected by $E_{\mathrm{T}}^{\mathrm{miss}}$ triggers would be over conservative. A one percent uncertainty on the trigger selection for the eeμ and μμμ final states, and 5% for the eee and eμμ final states is assigned instead. No scale factors will be applied on simulation as they are close to unity. Control plots are made in the dilepton region to validate all corrections applied to simulation and can be found in Appendix B .

NOTE: Make sure this is the case

5.1.3 Corrections

Mismatches between data and simulation are corrected for via the use of scale frcators. These are elaboratly discussed in Section 4.4. In this section a short overview of the applied corrections is given and their effect on a dilepton selection is shown.

Pile up reweighting

In data, the number of interactions per bunch crossing (pile up) is calculated with a minimum bias cross section of 69.2 mb. The number of simulated pile up events is then reweighed to match the expected number of pile up events in data. Pile up reweighting manifests itself as an altered shape of the number of reconstructed primary vertices as can be seen in Figure 5.4.

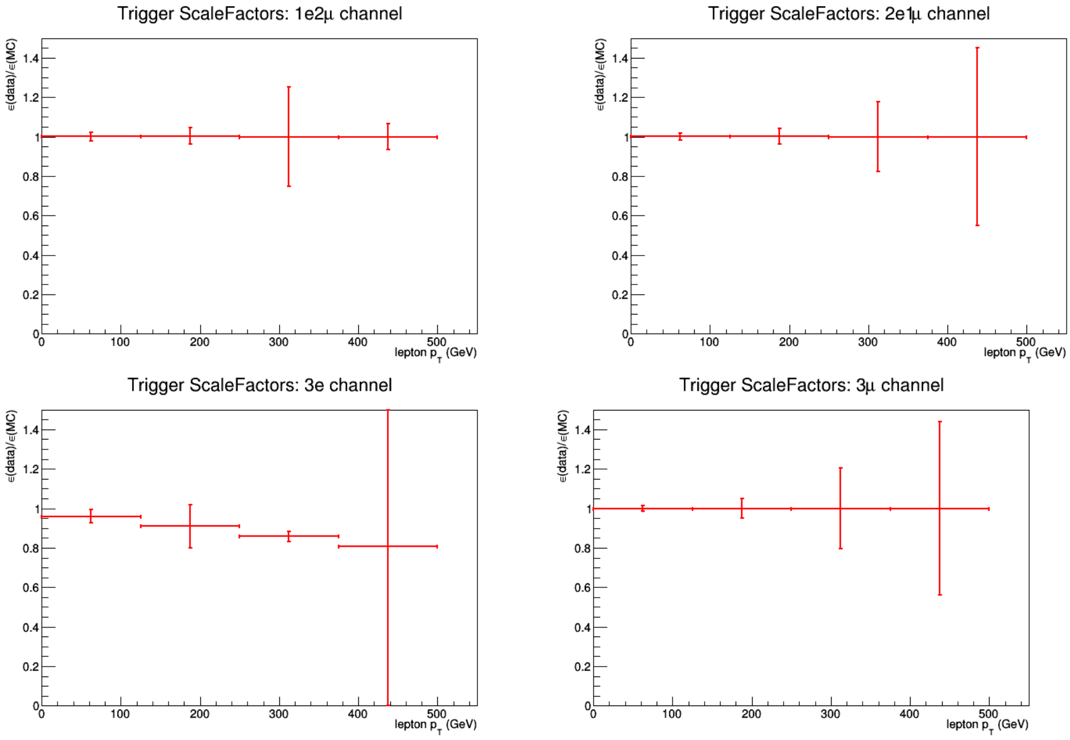

Figure 5.3: The trigger scale factors measured as a function of lepton p_{T} , using the dataset collected by $E_{\mathrm{T}}^{\mathrm{miss}}$ triggers and WZ simulation, after a 3 lepton and jets selection, in the Z mass window. All corrections to simulation are applied. Left, upper: eμμ channel. Right, upper: eeμ channel. Left, lower: eee channel. Right, lower: μμμ channel

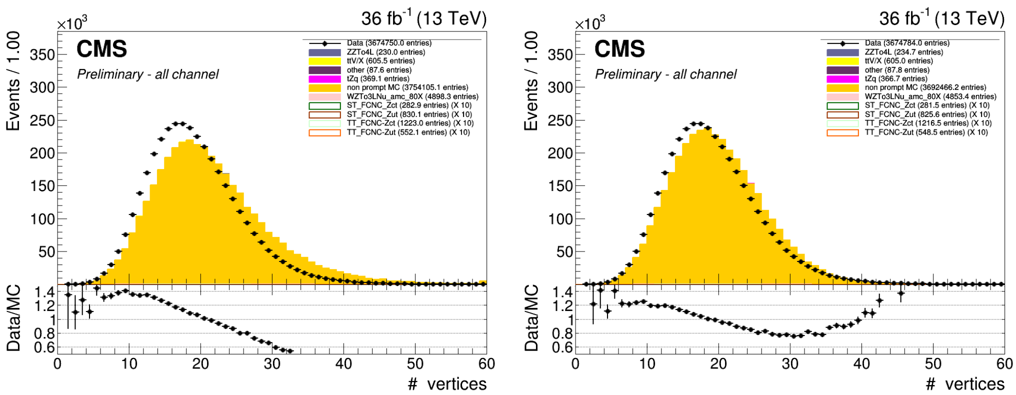

Figure 5.4: The number of primary vertices before (left) and after (right) pile up reweighting. After a 2 lepton plus jets selection, in the Z mass window.

Note that Figure 5.4 indicates that even after pile up reweighting, the primary vertex multiplicity is not well described by simulation. This is a known effect, and using a minimum bias cross section with a slightly lower value is found to better describe the data. However, the b tagging scale factors are only provided for the nominal inelastic cross section, and thus this value is used.

Lepton scale factors

The efficiency to select leptons is different in simulation (ϵ_{MC}) compared to the data (ϵ_{data}) . This is corrected for by applying lepton scale factors (SF) to the simulation that are defined as

$$SF = \frac{\epsilon_{\mathrm{data}}}{\epsilon_{\mathrm{MC}}}. \tag{5.4}$$

These scale factors are measured for the identification, isolation, tracking and trigger efficiencies of the objects as a function of p_{T} and η (see Section 4.4.1 and Section 4.4.2). Multiplying these scale factors for each lepton provides an overall efficiency:

$$SF^{\mu}_{\mathrm{global}} = \prod_{\mathrm{i}}^{\#\mu} SF^{\mu}_{\mathrm{ID}}(p_{\mathrm{T}},\eta) SF^{\mu}_{\mathrm{Iso.}}(p_{\mathrm{T}},\eta) SF^{\mu}_{\mathrm{Trig.}}(p_{\mathrm{T}},\eta) SF^{\mu}_{track}(p_{\mathrm{T}},\eta), \tag{5.5}$$

$$SF^{\mathrm{e}}_{\mathrm{global}} = \prod_{\mathrm{i}}^{\#e} SF^{\mathrm{e}}_{\mathrm{ID}}(p_{\mathrm{T}},\eta) SF^{\mathrm{e}}_{\mathrm{Iso.}}(p_{\mathrm{T}},\eta) SF^{\mathrm{e}}_{\mathrm{Trig.}}(p_{\mathrm{T}},\eta) SF^{\mathrm{e}}_{track}(p_{\mathrm{T}},\eta). \tag{5.6}$$

The effect of the scale factors can be found in Figure 5.6 for the electron scaling and Figure 5.5 for the muons. The trigger efficiencies are estimated in Section 5.1.2.

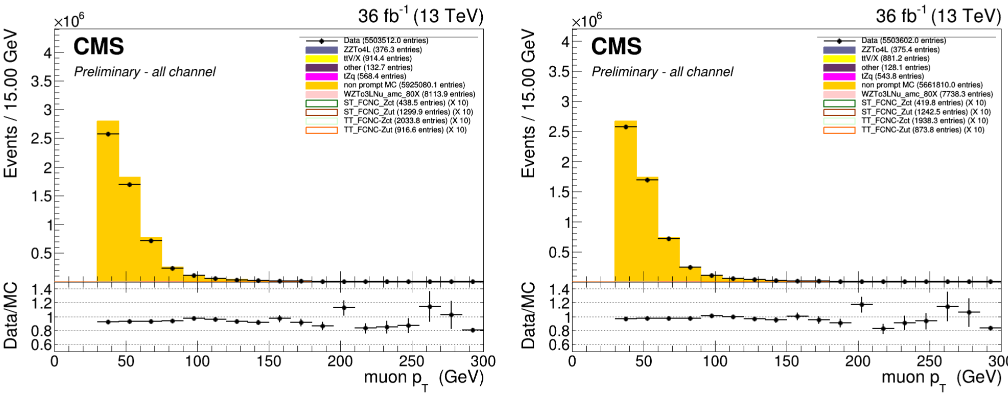

Figure 5.5: The p_{T} of the muons before (left) and after (right) muon scale factors. After a 2 lepton plus jets selection, in the Z mass window. Both after the Rochester correction.

Additionally, corrections are made for the energy resolution of the leptons. For the electrons, energy smearing and regression is applied [180]. The energy regression uses the detector information to correct the electron energy in order to have the best energy resolution by correcting local energy containment, material effects, etc.. The energy scale and smearing

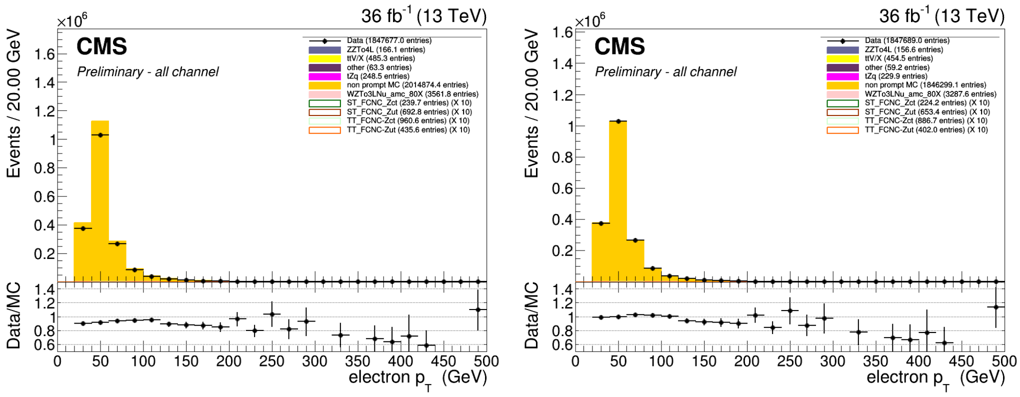

Figure 5.6: The p_T of the electrons before (left) and after (right) electron scale factors. After a 2 lepton plus jets selection, in the Z mass window. Both after energy scale corrections and smearing.

is done in order to bring the data energy scale to simulation level. It smears the simulation energies to have identical energy resolution in simulation and data. For the muons, the p_T is corrected using the Rochester method [181, 182]. This correction removes the bias of the muon p_T from any detector misalignment or any possible error of the magnetic field. The effect of the Rochester correction can be found in Figure 5.7.

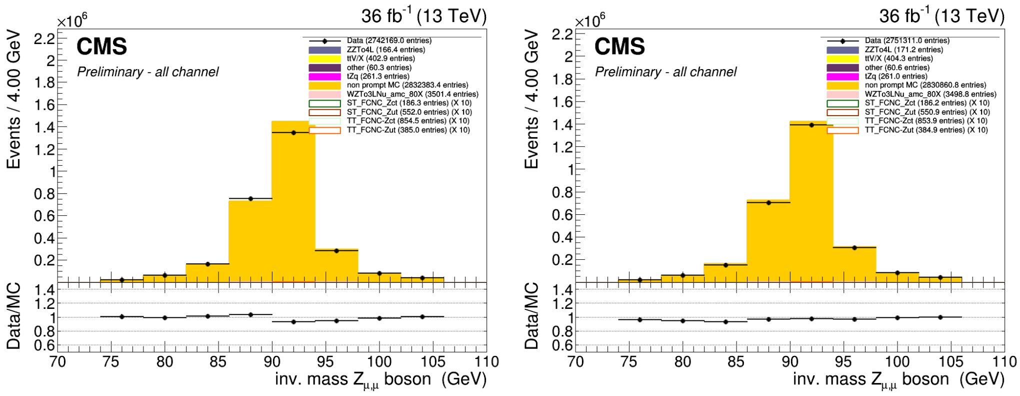

Figure 5.7: The mass of the Z boson consisting of the muons before (left) and after (right) the rochester correction. After a 2 lepton plus jets selection, in the Z mass window.

CSVv2 shape correction

In order to make the shape of the CSVv2 b-tagging discriminant in simulation agree with data, jet-by-jet based scale factors are applied. These scale factors are a function of the p_{T} , η and CSVv2 value of the jet as discussed in Section 4.4.4. The effect of these scale factors can be found in Figure 5.8.

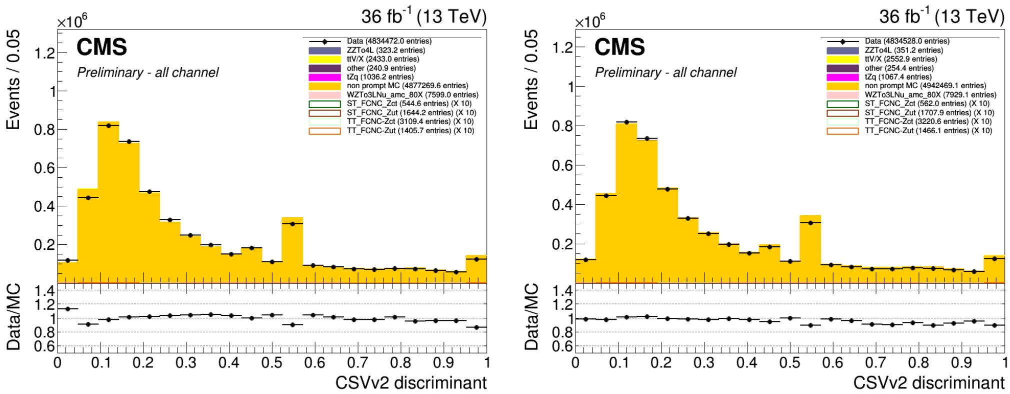

Figure 5.8: The CSVv2 discriminant of the jets before (left) and after (right) b-tag scale factors. After a 2 lepton plus jets selection, in the Z mass window.

Jet energy

The jet energy in data and simulation is corrected by the measured energy response of the detector. This provides p_T- η dependent scale factors and are directly taken from the frontier condition database as discussed in Section 4.4.3. The effect of the jet energy corrections can be found in Figure 5.9 and Figure 5.10.

NOTE: Fix jer plot

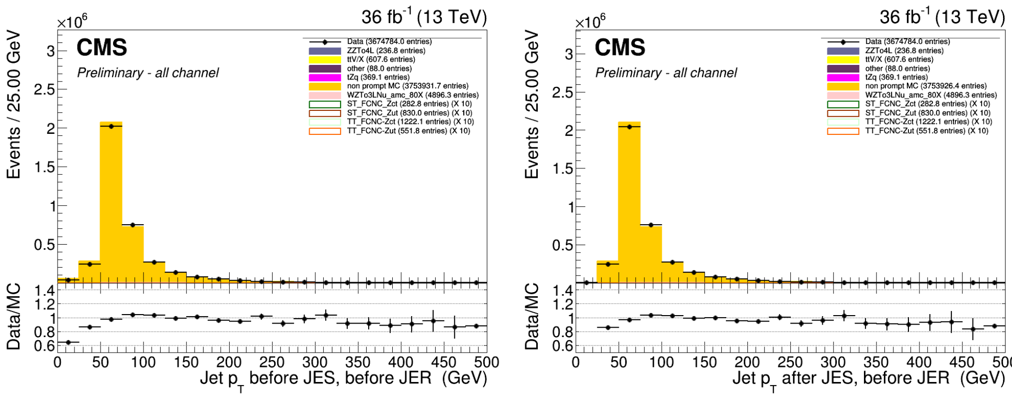

Figure 5.9: The p_{T} of the jets before (left) and after (right) jet energy scale corrections. After a 2 lepton plus jets selection, in the Z mass window.

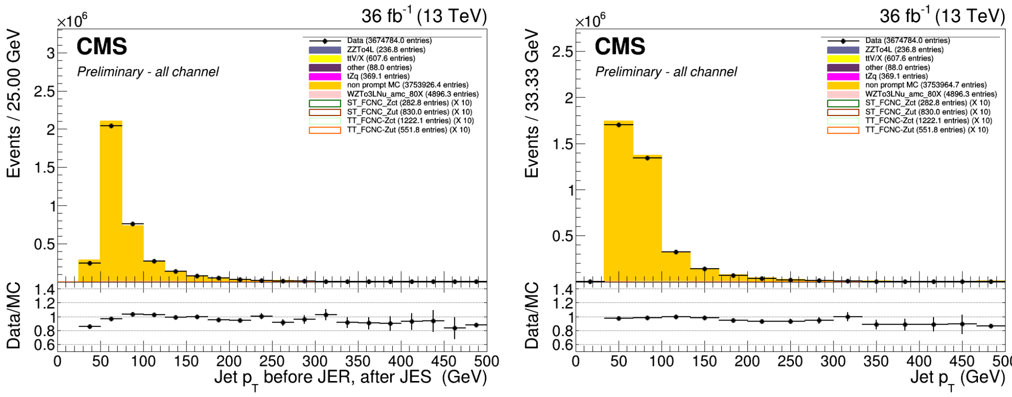

Figure 5.10: The p_{T} of the jets before (left) and after (right) jet energy resolution smearing. After a 2 lepton plus jets selection, in the Z mass window.

Missing transverse energy

The energy scale and resolution corrections applied to the jets are propagated back to the missing transverse energy (smeared Type I correction). This rebalances the transverse net momentum of the event and improves the missing transverse energy resolution itself.

5.2 Analysis Strategy

The analysis strategy uses five statistically independent regions to extract limits using a likelihood fit of various observables. Two signal regions, the tZ (STSR) and tZq (TTSR) signal region, are constructed using the jet multiplicity, focussed on each signal signature (see Tab. 5.7). In order to constrain the rate of WZ+jet events as well as that of NPL backgrounds three control regions are defined. The WZ control region (WZCR) focusses on NPLsoriginating from $Z/\gamma^* +$jets and simultaneously constrains the WZ+jets background rate. The NPL backgrounds coming from $t\bar{t}$, are constrained by two control regions, TTCR and STCR, one for each signal region (TTSR and STSR). In the STSR and TTSR multivariate discriminants based on Boosted Decision Trees (BDT) are used to respectively discriminate FCNC tZ and FCNC tZq from backgrounds. In the WZCR a discriminating variable between the two backgrounds, WZ+jets and NPLs, is used. In TTCR and STCR the dominating process is $t\bar{t}$+jets, and its rate is estimated by subtracting all other background predictions from data. A simultaneous global fit is performed taking into account each region (STSR, TTSR, WZCR, TTCR and STCR) for the four different leptonic channels.

5.3 Data driven NPL background simulation

The MC samples are used to model the backgrounds as well as for training the boosted decision trees for signal to background separation. One of the most important background consist of events with not prompt leptons. These are mostly instrumental background and are therefore very difficult to model. The NPL background is estimated from data for both its shape and its normalisation.

The NPL sources are

- hadronic objects wrongly reconstructed as leptons,
- real leptons coming from the semi leptonic decay of a b or c hadron,
- real leptons coming from the conversion of photons,

that pass the identification and isolation requirements. The dominant source of these NPLs depend on the flavour of the lepton and therefore the events with a noy prompt muon (NPμ) are treated differently than those with a not prompt electron (NPE). For muons, the dominant source is the semi leptonic decay of heavy flavour hadrons. For electrons, the dominant sources are hadrons and photon conversions.

The backgrounds causing NPL contributions are mostly $Z/\gamma^* + \text{jets}$(Drell–Yan) and $t\bar{t}$+jets dilepton processes, and in a smaller amount WW and tWZ. All of these backgrounds contain two real leptons and one NPLḊue to the fact that the probability for a lepton to be a NPL is small, backgrounds containing two or more NPL s are neglected. The assumption is made that for DY the two leptons compatible with a Z boson decay are the real leptons, and the additional lepton is coming from a NPL source, while for $t\bar{t}$+jets the NPL is associated to the Z boson.

The NPL sample is constructed from data by requiring exactly three leptons, from which two are considered real, isolated leptons and the third is a NPL. This NPL is created by loosening its identification and inverting its isolation criteria. The full requirements on the not prompt leptons are given in Table 5.5 and Table 5.6. For NPEs, a large fraction is coming from misidentified photons. These are removed by applying a tighter cut on the $1/E - 1/p$ variable, and by limiting the isolation values to be smaller than one.

The NPL samples are defined in a given control region and are used to describe their contribution in the other regions.

5.4 Regions and channels

The regions are defined as in Table 5.7 after a common selection of

- exactly 3 leptons containing one opposite sign, same flavour pair that are assigned to the Z boson,
- at least 1 jet and at the most 3 jets,
- the transverse mass of the W boson to be maximal 300 GeV,

The cut on the transverse mass of the W boson is done to remove events that are passing the events cleaning elading to anomalous large missing transverse energy. The transverse mass $m_\mathrm{T}(\mathrm{W})$ is reconstructed using

$$m_\mathrm{T}(\mathrm{W}) = \sqrt{(p_\mathrm{T}(l_\mathrm{W}) + p_\mathrm{T}(\nu_\mathrm{W}))^2 - (p_\mathrm{x}(l_\mathrm{W}) + p_\mathrm{x}(\nu_\mathrm{W}))^2 - (p_\mathrm{y}(l_\mathrm{W}) + p_\mathrm{y}(\nu_\mathrm{W}))^2} \tag{5.7}$$

Table 5.5: Non prompt electron requirements used in this analysis. The requirements are set in the barrel ($|\eta_{supercluster}| \leq 1.479$) and the end caps ($|\eta_{supercluster}| > 1.479$).

	$|\eta_{supercluster}| \leq 1.479$	$|\eta_{supercluster}| > 1.479$
$\sigma_{\eta\eta}$	< 0.011	< 0.0314
$|\Delta\eta_{\mathrm{in}}|$	< 0.00477	< 0.00868
$|\Delta\phi_{\mathrm{in}}|$	< 0.222	< 0.212
H/E	< 0.298	< 0.101
relative isolation	≥ 0.0588 && < 1	≥ 0.0571 && < 1
$|1/E - 1/p|$	< 0.0129 GeV^{-1}	< 0.0129 GeV^{-1}
expected missing inner hits	≤ 1	≤ 1
pass conversion veto	Y	Y
p_{T}	> 35 GeV	> 35 GeV

Table 5.6: Non prompt muon requirements used in the analysis.

	modified Loose Muon WP
Global muon or Tracker Muon	Both
Particle Flow muon	Y
$\chi^2/ndof$ of global muon track fit	N/A
Nb. of hit muon chambers	N/A
Nb. of muon stations contained in the segment	N/A
Size of the transverse impact parameter of the track wrt. PV	N/A
Longitudinal distance wrt. PV	N/A
Nb. of pixel hits	N/A
Nb. of tracker layers with hits	N/A
Relative Isolation	≥ 0.15
p_{T}	> 30 GeV

Table 5.7: The statistically independent regions used in the analysis.

	WZCR	STSR	TTSR	STCR	TTCR
Number of jets	$\geqslant 1$	1	$\geqslant 2$	1	$\geqslant 2$
Number of b jets	0	1	$\geqslant 1$	1	$\geqslant 1$
$\lvert m_{\mathrm{Z}}^{\mathrm{reco}} - m_{\mathrm{Z}} \rvert < 7.5$ GeV	Yes	Yes	Yes	No	No

Additional leptons are vetoed in order to reduce the contamination of backgrounds with four or more leptons in the final state, e.g. ZZ, $\mathrm{t\bar{t}Z}$, and $\mathrm{t\bar{t}H}$. The most important backgrounds are the ones that contain three prompt leptons in the final state. These are mainly WZ+jets, $\mathrm{t\bar{t}Z}$ and SM tZq. For these backgrounds, the three lepton topology is identical to the FCNC signal: two opposite sign leptons of the same flavour decaying from the Z boson, and a third additional, high p_{T} lepton coming from the W boson decay.

For the FCNC tZ final state, one b jet coming from the SM top decay is expected. For the FCNC tZq, an additional light jet is expected. In the $\mathrm{t\bar{t}Z}$ final state, two b jets are present in the final state. However, due to inefficiencies of the b-tagging algorithm, one of the two b jets may be identified as a light quark jet, giving the same final state as the FCNC tZq final state. For the WZ+jets final states, one of the b jets produced by gluon splitting can be b-tagged or light flavour jets coming from the WZ+jets production can be mis-tagged as b jets. The SM tZq final state expects the same signal as FCNC tZq.

The NPL events give a significant background contribution. This background is coming mainly from Z/γ^* +jets and $\mathrm{t\bar{t}}$+jets processes (in a less significant way, also WW and tWZ contributes), which have very high cross sections and causes a large number of NPL background events compared to signal.

In order to reduce the large uncertainties in backgrounds, five independent regions are used as defined in Table 5.7.

5.4.1 WZ control region

In this region, a fit is performed on the transverse mass of the W boson, in order to estimate the NPL yield coming from Z/γ^* +jets and the WZ+jets backgrounds.

A transfer factor is used to account for going from a region without b-tagged jets to a region with exactly one b-tagged jet, or at least one b-tagged jet. For this the probability of tagging at least one jet with the CSVv2 loose working point is used to calculate the expected number of events, N_b, after b tagging:

$$N_b = \frac{\sum\limits_{\text{events}} \mathscr{P}_b}{\text{total nb of events}}, \tag{5.8}$$

where $\mathscr{P}_b$ is the probability that an event survives the b-tagging requirement

$$\begin{aligned}\mathscr{P}_b =& 1 - \mathrm{P}(\text{event doesn't survive b tag}) \\ =& 1 - \left(\prod_b \mathrm{P}(\text{b not tagged}) \prod_c \mathrm{P}(\text{c not tagged}) \prod_{udsg} \mathrm{P}(\text{light not tagged}) \right)\end{aligned} \tag{5.9}$$

with the products going over all b-, c-, and light jets. The jet flavour is determined by means of matching the reconstructed jet to the generated quark based on the distance in the $\eta\phi$ plane. In order to estimate the probablity for exactly one b-tagged jet, the expected number of events is corrected by the fraction of events with exactly one jet in the WZCR. The resulting transfer factors are given in Appendix C . One can see that the yield of WZ+jets events in the signal region estimated using the above described transfer factor and the yield calculated with simulated events are in agreement.

NOTE: make appendix

5.4.2 TTCR and STCR

The TTCR and STCRhave the same selection criteria as TTSR and STSR but are outside the Z mass window (sidebands):

$$7.5\,GeV < |m_{\mathrm{Z}}^{\mathrm{reco}} - m_{\mathrm{Z}}| < 30\,GeV. \tag{5.10}$$

where $M(Z_{reco})$ is the reconstructed mass of the Z boson in the event, and $M(Z)$ the mass of the Z boson. These regions are dominated by $t\bar{t}$+jets (see Appendix C) and are used to estimate the NPL coming from $t\bar{t}$+jets in the STSR and TTSR. Since there aren't enough events entering these regions, no shapes are used in the fit. The distribution of the mass of the Z boson is flat for $t\bar{t}$+jets events, as shown in Fig. Figure 5.11, and thus the number of expected events, N_s, in the signal regions estimated from the number of expected events, N_c, in the control region is obtained as

$$N_s = \frac{15}{60-15} N_c. \tag{5.11}$$

The resulting transfer factors are given in Appendix C. The expected yield in the signal region estimated from the TTCR (STCR) is in agreement with the yield calculated from simulated events.

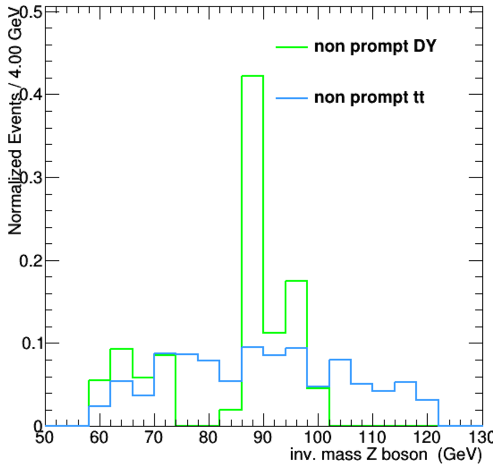

Figure 5.11: The normalized distribution for $Z/\gamma^* +$jets and $t\bar{t}$+jets events before dividing the events in to regions, after $|m_Z^{\text{reco}} - m_Z| < 30$ GeV. All leptonic channels combined.

5.4.3 TTSR and STSR

The TTSR is defined to target top quark pair FCNC (tZq), while the STSR focusses on single top quark FCNC (tZ). They have NPL contributions coming from $Z/\gamma^* +$jets and $t\bar{t}$+jets events. In this region, the data driven NPL template is split into two templates based on the presence of the NPL in the Z boson:

- NPL associated with W boson is assigned to $Z/\gamma^* +$jets and estimated in the WZCR.
- NPL associated with Z boson is assigned to $t\bar{t}$+jets and estimated in the TTCR and STCR.

6 The search for FCNC involving a top quark and a Z boson

6.1 Construction of template distributions

6.2 Systematic uncertainties

6.3 Limit setting procedure

6.4 Result and discussion

7 Denouement of the top-Z FCNC hunt at 13 TeV

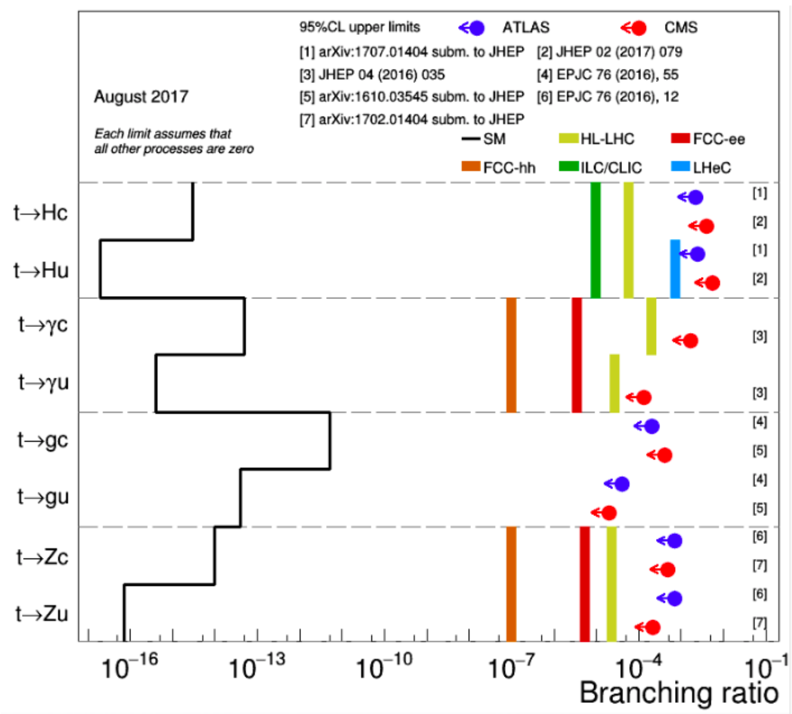

Figure 7.1:

A Trigger scale factors

The trigger scale factors measured as a function of lepton p_{T} , using the dataset collected by $E_{\mathrm{T}}^{\mathrm{miss}}$ triggers and WZ simulation, after a 3 lepton and jets selection, in the Z mass window. All corrections to simulation are applied.

Table A.1: Trigger efficiencies on data events selected with $E_{\mathrm{T}}^{\mathrm{miss}}$ triggers and WZ simulation for all leptonic channels together. The unweighed number of events is quoted. When there are no events passing the cuts, it is indicated with N/A. The uncertainties are statistical uncertainties.

ALL CHANNEL	data		WZ simulations	
	Efficiency	unc.	Efficiency	unc.
3 lep, at least one jet	117/118 = 99.15 %	12.94%	18047/18055 = 99.96%	1.05%
STSR	6/6 = 100.00%	57.74%	1541/1541 = 100.00%	3.60%
TTSR	26/27 = 96.30%	26.46%	1791/1792 = 99.94%	3.34%
WZCR	69/69 = 100.00 %	17.03%	14405/14412=99.95%	1.18%

Table A.2: Trigger efficiencies on data events selected with $E_{\mathrm{T}}^{\mathrm{miss}}$ triggers and WZ simulation for $\mu\mu\mu$ leptonic channel together. The unweighed number of events is quoted. When there are no events passing the cuts, it is indicated with N/A. The uncertainties are statistical uncertainties.

$\mu\mu\mu$ CHANNEL	data		WZ simulations	
	Efficiency	unc.	Efficiency	unc.
3 lep, at least one jet	40/40 = 100.00 %	22.36 %	7814/7814 = 100.00%	1.60%
STSR	N/A	N/A	687/687 = 100%	5.40%
TTSR	13/13 = 100.00%	39.22%	763/763 = 100.00%	5.12%
WZCR	22/22 = 100.00 %	30.15%	6238/6238=100.00%	1.79%

Table A.3: Trigger efficiencies on data events selected with $E_{\mathrm{T}}^{\mathrm{miss}}$ triggers and WZ simulation for eee leptonic channel together. The unweighed number of events is quoted. When there are no events passing the cuts, it is indicated with N/A. The uncertainties are statistical uncertainties.

eee CHANNEL	data		WZ simulations	
	Efficiency	unc.	Efficiency	unc.
3 lep, at least one jet	20/21 = 95.24%	29.76%	2211/2215 = 99.82 %	3.00%
STSR	4/4 = 100.00%	70.71%	176/176 = 100.00%	10.66%
TTSR	2/3 = 66.67%	60.86%	242/242 = 100.00%	9.09%
WZCR	14/14 = 100.00 %	37.80%	1744/1748=99.77%	3.38%

Table A.4: Trigger efficiencies on data events selected with $E_{\mathrm{T}}^{\mathrm{miss}}$ triggers and WZ simulation for $ee\mu$ leptonic channel together. The unweighed number of events is quoted. When there are no events passing the cuts, it is indicated with N/A. The uncertainties are statistical uncertainties.

$ee\mu$ CHANNEL	data		WZ simulations	
	Efficiency	unc.	Efficiency	unc.
3 lep, at least one jet	32/32 = 100.00 %	25.00 %	3116/3118 = 99.94%	2.53%
STSR	1/1 = 100.00%	141.42%	255/255 = 100%	8.86%
TTSR	9/9 = 100.00%	47.14%	291/291 = 100.00%	8.29%
WZCR	14/14 = 100.00 %	37.80%	2529/2531=99.92%	2.81%

Table A.5: Trigger efficiencies on data events selected with $E_{\mathrm{T}}^{\mathrm{miss}}$ triggers and WZ simulation for $e\mu\mu$ leptonic channel together. The unweighed number of events is quoted. When there are no events passing the cuts, it is indicated with N/A. The uncertainties are statistical uncertainties.

$e\mu\mu$ CHANNEL	data		WZ simulations	
	Efficiency	unc.	Efficiency	unc.
3 lep, at least one jet	25/25 = 100.00%	28.28%	4906/4908 = 99.96 %	2.02%
STSR	1/1 = 100.00%	141.42%	423/423 = 100.00%	6.88%
TTSR	2/2 = 100.00%	100.00%	495/496 = 99.80%	6.34%
WZCR	19/19 = 100.00 %	32.44%	3894/3895 =99.97%	2.27%

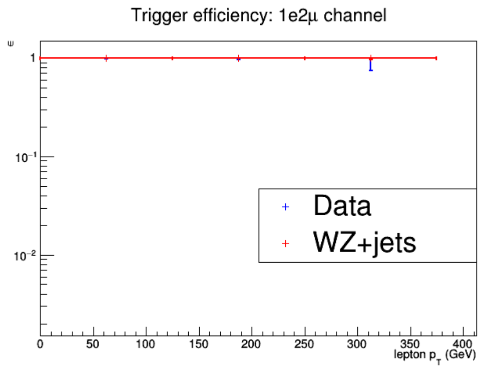

[In function of lepton p_T]

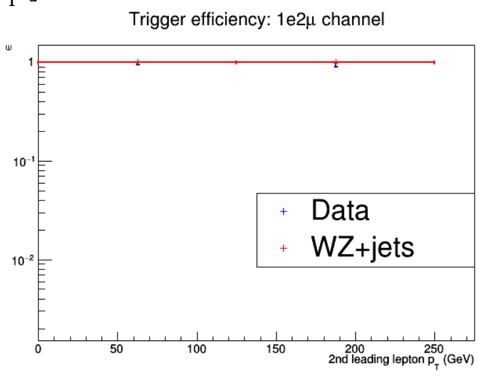

[In function of 2nd leading lepton in p_T]

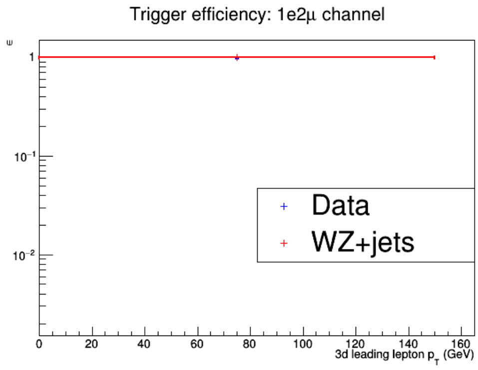

[In function of 3d leading lepton in p_T]

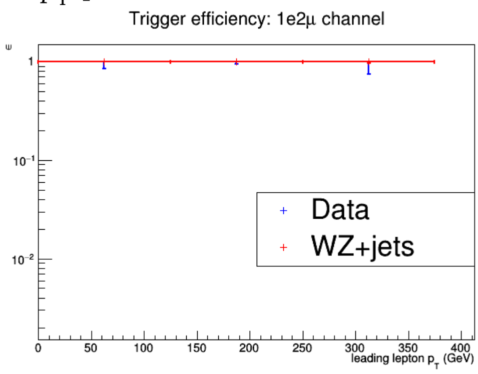

[In function of leading lepton in p_T]

Figure A.1: The trigger efficiencies measured as a function of lepton p_T , using the dataset collected by E_T^{miss} triggers and WZ simulation, after a 3 lepton and jets selection, in the Z mass window. All corrections to simulation are applied. 1e2μ channel.

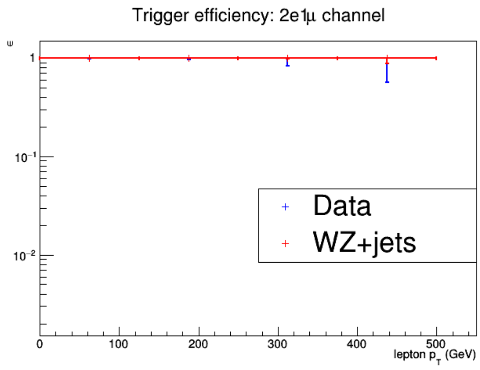

[In function of lepton p_T] [In function of 2nd

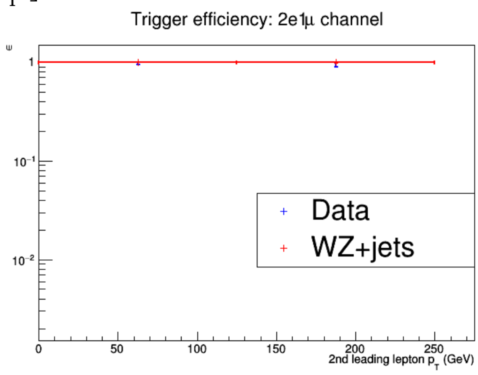

leading lepton in p_T]

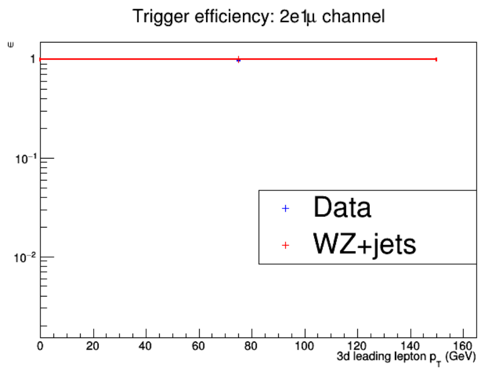

[In function of 3d leading lepton in p_T] [In

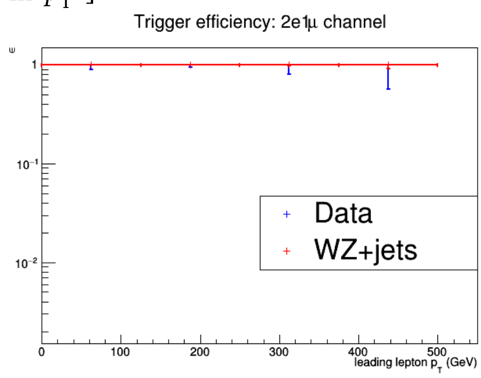

function of leading lepton in p_T]

Figure A.2: The trigger efficiencies measured as a function of lepton p_T , using the dataset collected by E_T^{miss} triggers and WZ simulation, after a 3 lepton and jets selection, in the Z mass window. All corrections to simulation are applied. 2e1μ channel.

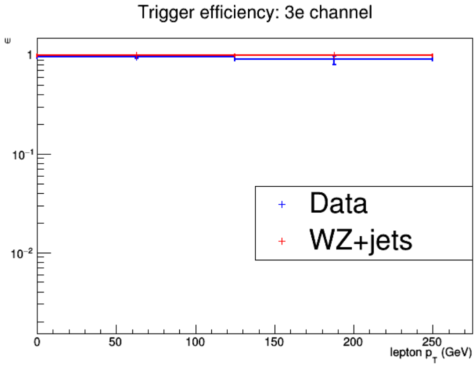

[In function of lepton p_T]

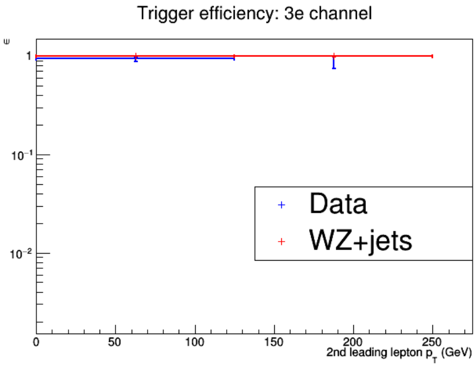

[In function of 2nd leading lepton in p_T]

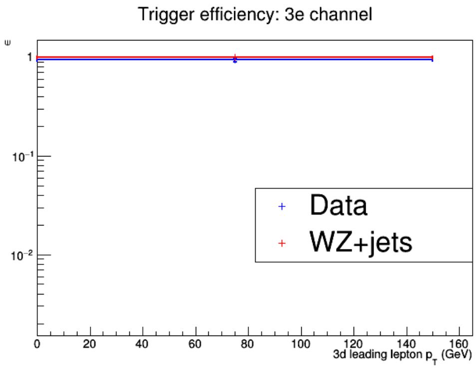

[In function of 3d leading lepton in p_T]

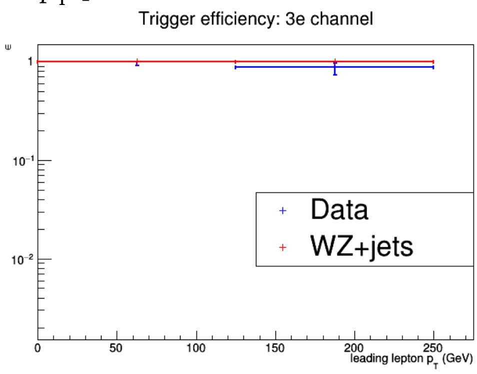

[In function of leading lepton in p_T]

Figure A.3: The trigger efficiencies measured as a function of lepton p_T , using the dataset collected by E_T^{miss} triggers and WZ simulation, after a 3 lepton and jets selection, in the Z mass window. All corrections to simulation are applied. 3e channel.

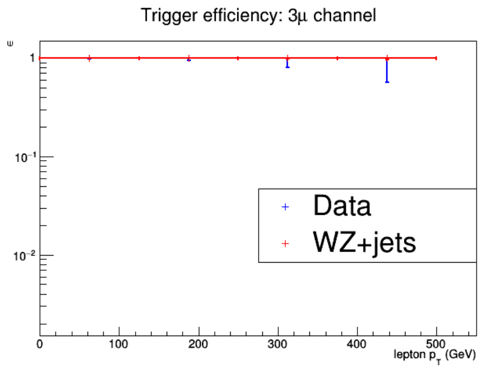

[In function of lepton p_T] [In function of 2nd

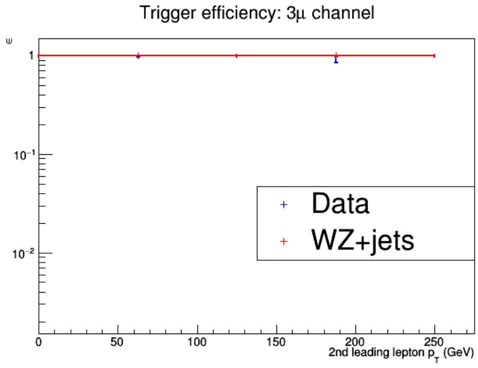

leading lepton in p_T]

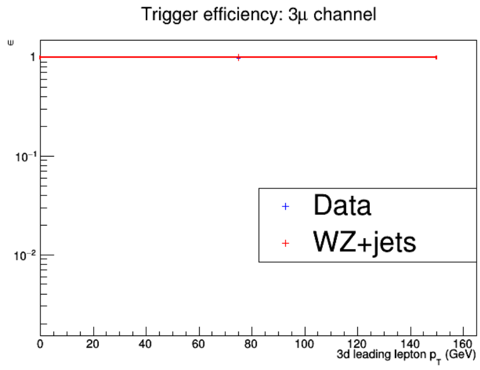

[In function of 3d leading lepton in p_T] [In

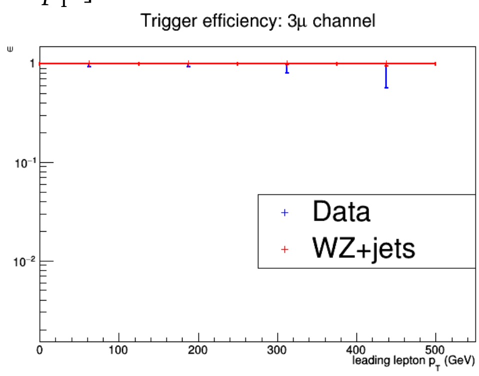

function of leading lepton in p_T]

Figure A.4: The trigger efficiencies measured as a function of lepton p_T , using the dataset collected by E_T^{miss} triggers and WZ simulation, after a 3 lepton and jets selection, in the Z mass window. All corrections to simulation are applied. 3μ channel.

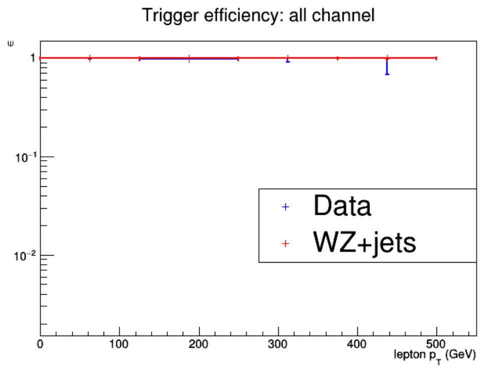

[In function of lepton p_T]

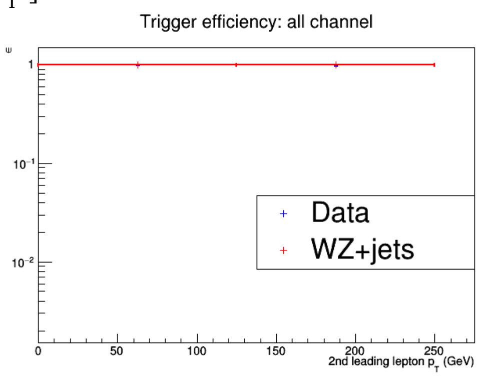

[In function of 2nd leading lepton in p_T]

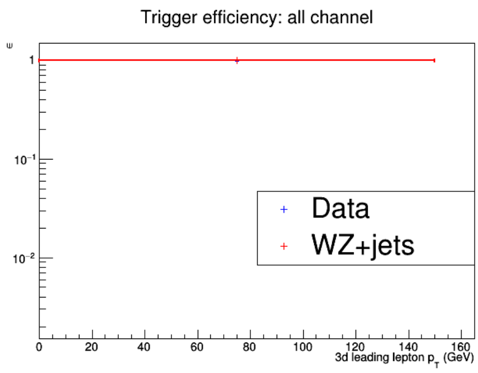

[In function of 3d leading lepton in p_T]

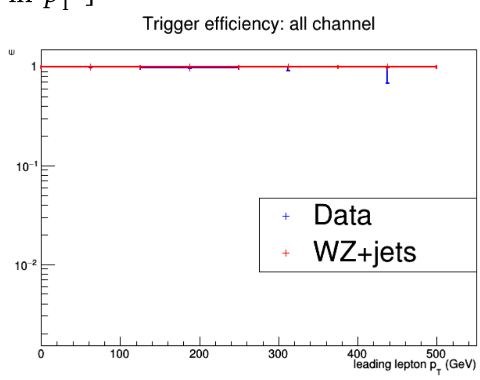

[In function of leading lepton in p_T]

Figure A.5: The trigger efficiencies measured as a function of lepton p_T , using the dataset collected by E_T^{miss} triggers and WZ simulation, after a 3 lepton and jets selection, in the Z mass window. All corrections to simulation are applied. All channel.

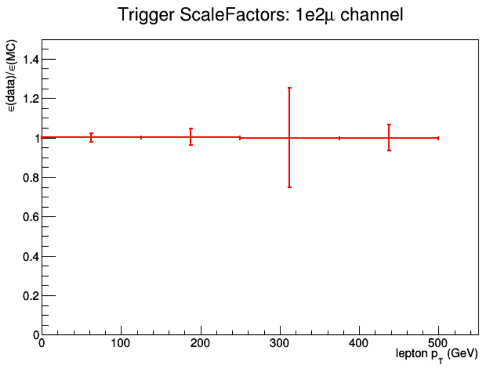

[In function of lepton p_T]

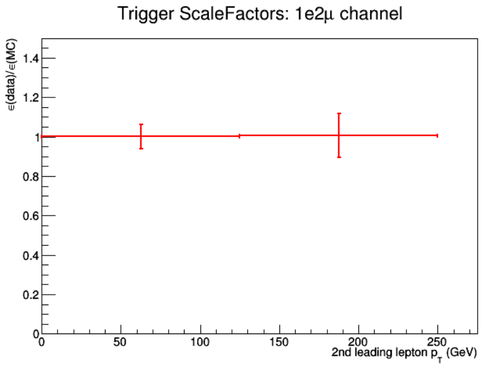

[In function of 2nd leading lepton in p_T]

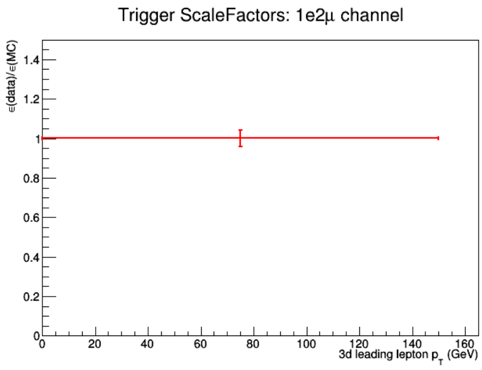

[In function of 3d leading lepton in p_T]

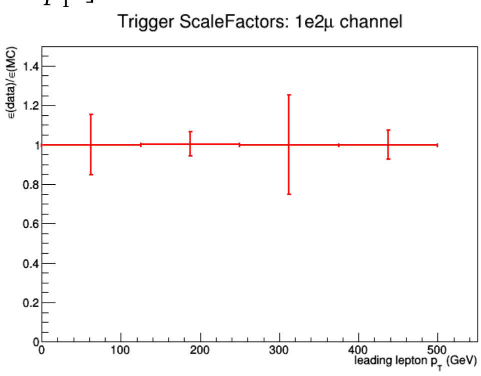

[In function of leading lepton in p_T]

Figure A.6: The trigger scale factors measured as a function of lepton p_T , using the dataset collected by E_T^{miss} triggers and WZ simulation, after a 3 lepton and jets selection, in the Z mass window. All corrections to simulation are applied. 1e2μ channel.

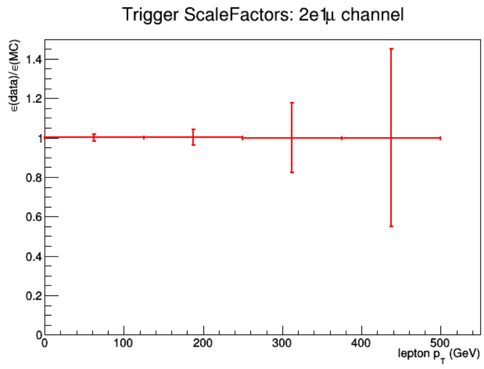

[In function of lepton p_T]

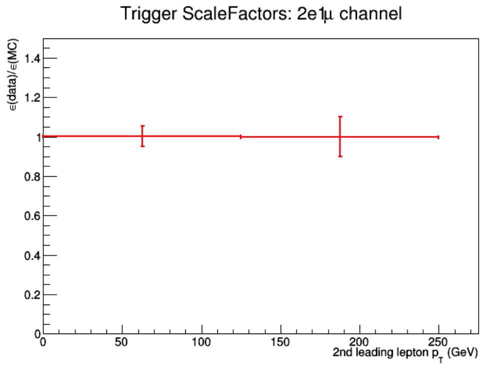

[In function of 2nd leading lepton in p_T]

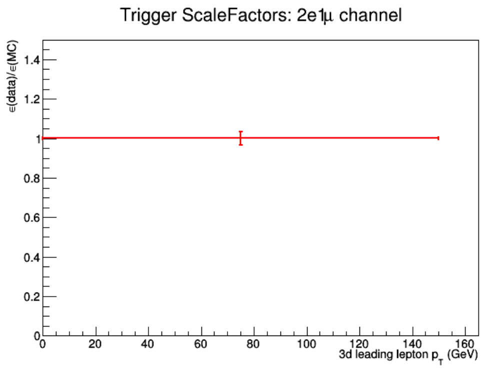

[In function of 3d leading lepton in p_T]

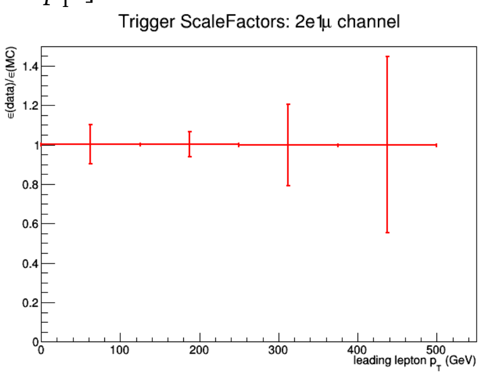

[In function of leading lepton in p_T]

Figure A.7: The trigger scale factors measured as a function of lepton p_T , using the dataset collected by E_T^{miss} triggers and WZ simulation, after a 3 lepton and jets selection, in the Z mass window. All corrections to simulation are applied. 2e1μ channel.

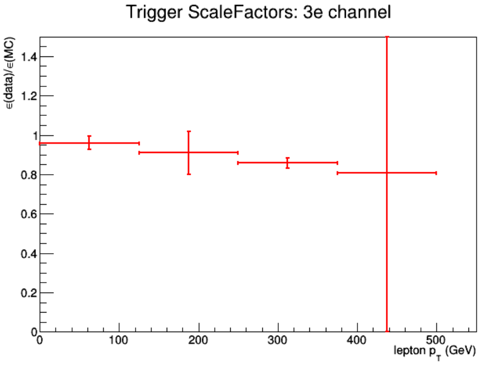

[In function of lepton p_T]

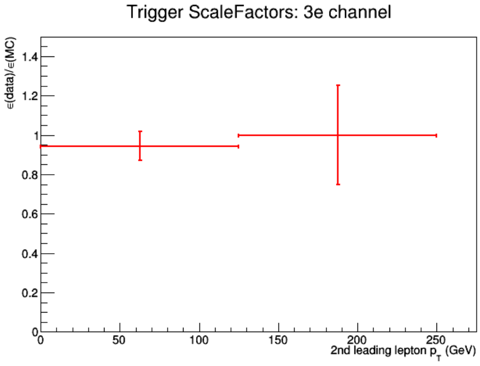

[In function of 2nd leading lepton in p_T]

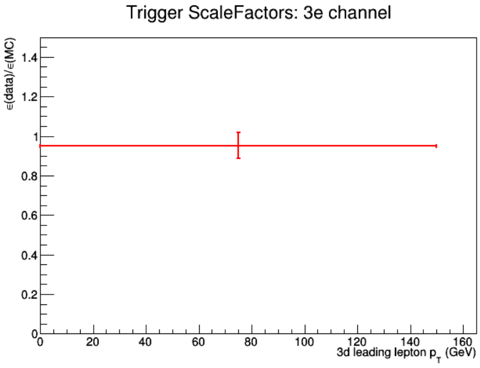

[In function of 3d leading lepton in p_T]

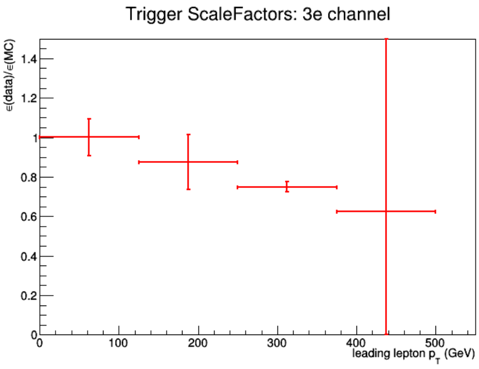

[In function of leading lepton in p_T]

Figure A.8: The trigger scale factors measured as a function of lepton p_T , using the dataset collected by E_T^{miss} triggers and WZ simulation, after a 3 lepton and jets selection, in the Z mass window. All corrections to simulation are applied. 3e channel.

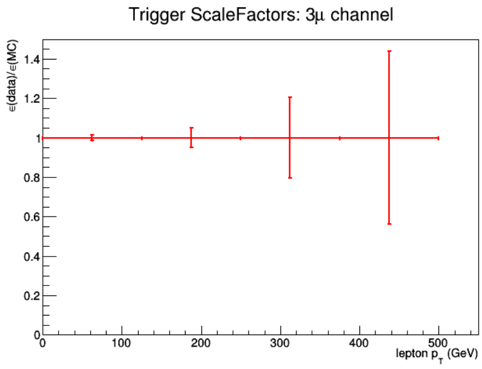

[In function of lepton p_T] [In function of 2nd

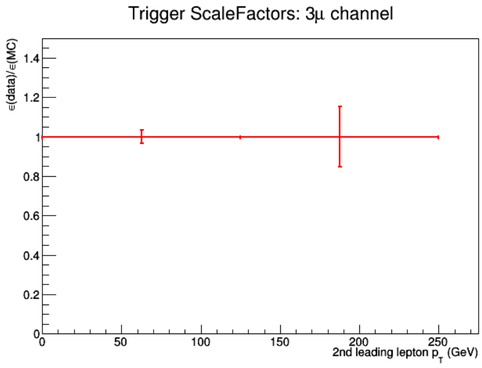

leading lepton in p_T]

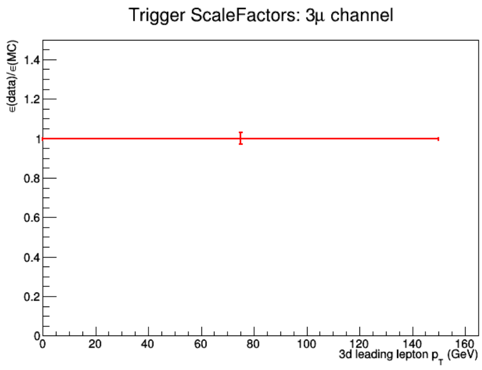

[In function of 3d leading lepton in p_T] [In

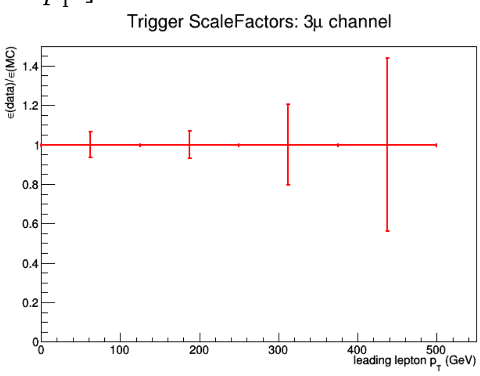

function of leading lepton in p_T]

Figure A.9: The trigger scale factors measured as a function of lepton p_T , using the dataset collected by E_T^{miss} triggers and WZ simulation, after a 3 lepton and jets selection, in the Z mass window. All corrections to simulation are applied. 3μ channel.

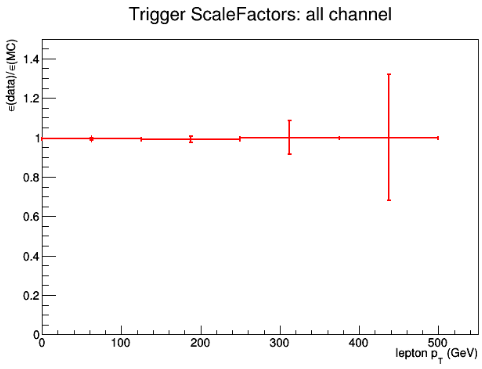

[In function of lepton p_T]

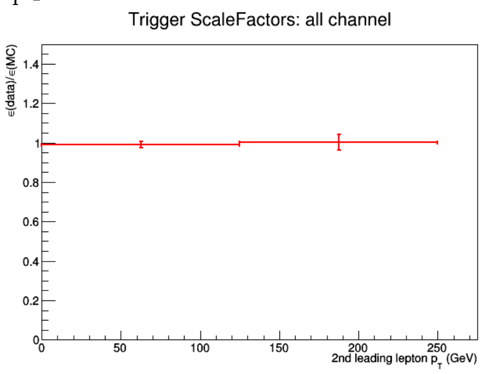

[In function of 2nd leading lepton in p_T]

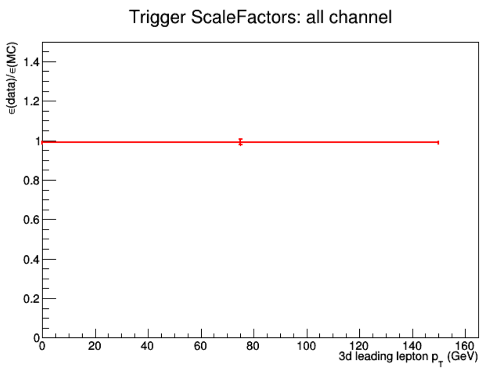

[In function of 3d leading lepton in p_T]

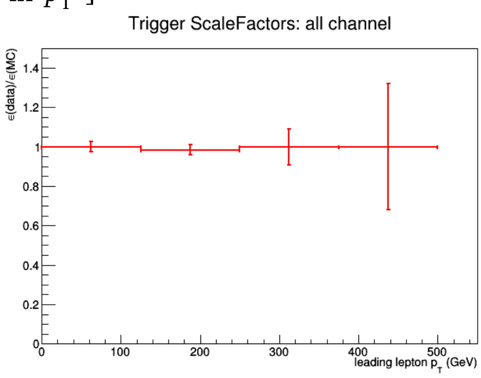

[In function of leading lepton in p_T]

Figure A.10: The trigger scale factors measured as a function of lepton p_T , using the dataset collected by E_T^{miss} triggers and WZ simulation, after a 3 lepton and jets selection, in the Z mass window. All corrections to simulation are applied. All channel.

B Dilepton controlplots

C Statistical independent regions

Bibliography

[1] Michael E Peskin and Daniel V Schroeder: **An introduction to quantum field theory; 1995 ed.** Includes exercises. Boulder, CO: Westview, 1995. URL: https://cds.cern.ch/record/257493 (see pp. 1, 5, 11, 16).

[2] C. P. Burgess: **Introduction to Effective Field Theory**. In: *Ann. Rev. Nucl. Part. Sci.*, **57**: (2007), pp. 329–362. DOI: 10.1146/annurev.nucl.56.080805.140508. arXiv: hep-th/0701053 [hep-th] (see p. 1).

[3] Nadia Robotti: **The discovery of the electron: I**. In: *European Journal of Physics*, **18**:3 (1997), p. 133. URL: http://stacks.iop.org/0143-0807/18/i=3/a=002 (see p. 2).

[4] Y. Fukuda et al.: **Evidence for oscillation of atmospheric neutrinos**. In: *Phys. Rev. Lett.*, **81**: (1998), pp. 1562–1567. DOI: 10.1103/PhysRevLett.81.1562. arXiv: hep-ex/9807003 [hep-ex] (see pp. 2, 14).

[5] Y. Abe et al.: **Indication of Reactor $\overline{\nu}_e$ Disappearance in the Double Chooz Experiment**. In: *Phys. Rev. Lett.*, **108**: (13 Mar. 2012), p. 131801. DOI: 10.1103/PhysRevLett.108.131801 (see pp. 2, 14).

[6] C. Patrignani et al.: **Review of Particle Physics**. In: *Chin. Phys.*, **C40**:10 (2016), p. 100001. DOI: 10.1088/1674-1137/40/10/100001 (see pp. 2–3, 6–9, 42–43, 68).

[7] S. Abachi et al.: **Observation of the top quark**. In: *Phys. Rev. Lett.*, **74**: (1995), pp. 2632–2637. DOI: 10.1103/PhysRevLett.74.2632. arXiv: hep-ex/9503003 [hep-ex] (see p. 2).

[8] F. Abe et al.: **Observation of top quark production in $\bar{p}p$ collisions**. In: *Phys. Rev. Lett.*, **74**: (1995), pp. 2626–2631. DOI: 10.1103/PhysRevLett.74.2626. arXiv: hep-ex/9503002 [hep-ex] (see p. 2).

[9] **First combination of Tevatron and LHC measurements of the top-quark mass**. In: (2014). arXiv: 1403.4427 [hep-ex] (see p. 2).

[10] Serguei Chatrchyan et al.: **Observation of a new boson at a mass of 125 GeV with the CMS experiment at the LHC**. In: *Phys. Lett.*, **B716**: (2012), pp. 30–61. DOI: 10.1016/j.physletb.2012.08.021. arXiv: 1207.7235 [hep-ex] (see pp. 2, 23).

[11] Georges Aad et al.: **Observation of a new particle in the search for the Standard Model Higgs boson with the ATLAS detector at the LHC**. In: *Phys. Lett.*, **B716**: (2012), pp. 1–29. DOI: 10.1016/j.physletb.2012.08.020. arXiv: 1207.7214 [hep-ex] (see pp. 2, 23).

[12] Nicola Cabibbo: **Unitary Symmetry and Leptonic Decays**. In: *Phys. Rev. Lett.*, **10**: (12 June 1963), pp. 531–533. doi: 10.1103/PhysRevLett.10.531 (see p. 5).

[13] S. L. Glashow, J. Iliopoulos, and L. Maiani: **Weak Interactions with Lepton-Hadron Symmetry**. In: *Phys. Rev. D*, **2**: (7 Oct. 1970), pp. 1285–1292. doi: 10.1103/PhysRevD.2.1285 (see p. 5).

[14] B.J. Bjørken and S.L. Glashow: **Elementary particles and SU(4)**. In: *Physics Letters*, **11**:3 (1964), pp. 255–257. doi: https://doi.org/10.1016/0031-9163(64)90433-0 (see p. 5).

[15] Luciano Maiani: **The GIM Mechanism: origin, predictions and recent uses**. In: *Proceedings, 48th Rencontres de Moriond on Electroweak Interactions and Unified Theories: La Thuile, Italy, March 2-9, 2013*. 2013, pp. 3–16. arXiv: 1303.6154 [hep-ph]. url: https://inspirehep.net/record/1225307/files/arXiv:1303.6154.pdf (see p. 5).

[16] Patrick Koppenburg and Sebastien Descotes-Genon: **The CKM Parameters**. In: (2017). arXiv: 1702.08834 [hep-ex] (see p. 6).

[17] J. A. Aguilar-Saavedra: **Top flavor-changing neutral interactions: Theoretical expectations and experimental detection**. In: *Acta Phys. Polon.*, **B35**: (2004), pp. 2695–2710. arXiv: hep-ph/0409342 [hep-ph] (see pp. 6, 15–17).

[18] S. Abachi et al.: **Observation of the top quark**. In: *Phys. Rev. Lett.*, **74**: (1995), pp. 2632–2637. doi: 10.1103/PhysRevLett.74.2632. arXiv: hep-ex/9503003 [hep-ex] (see p. 6).

[19] F. Abe et al.: **Observation of top quark production in $\bar{p}p$ collisions**. In: *Phys. Rev. Lett.*, **74**: (1995), pp. 2626–2631. doi: 10.1103/PhysRevLett.74.2626. arXiv: hep-ex/9503002 [hep-ex] (see p. 6).

[20] LHCTop working group: **LHCTopWG Summary plots**. Sept. 2017. url: https://twiki.cern.ch/twiki/bin/view/LHCPhysics/LHCTopWGSummaryPlots (see pp. 8, 21).

[21] Andrea Giammanco and Jeannine Wagner-Kuhr: **Measurement of the t-channel single Top-quark production rates in pp collisions at 7 TeV**. Sept. 2011. url: http://cms.web.cern.ch/news/measurement-t-channel-single-top-quark-production-rates-pp-collisions-7-tev (see p. 9).

[22] LHCTop working group: **ATLAS-CMS recommended predictions for single top cross sections using the Hathor v2.1 program.** Sept. 2017. url: https://twiki.cern.ch/twiki/bin/view/LHCPhysics/SingleTopRefXsec#Predictions_at_7_8_13_and_14_TeV (see p. 9).

[23] CMS collaboration: **Summaries of CMS cross section measurements**. Oct. 2017. url: https://twiki.cern.ch/twiki/bin/view/CMSPublic/PhysicsResultsCombined (see pp. 10, 20, 22, 50).

[24] Céline Degrande: **Effective field theories in the Standard Model and beyond**. Thesis. Université Catholique de Louvain, Sept. 2011. url: https://cp3.irmp.ucl.ac.be/upload/theses/phd/degrande.pdf (see pp. 10–11).

[25] Enrico Fermi: **Tentativo di una Teoria Dei Raggi β**. In: *Il Nuovo Cimento (1924-1942)*, **11**:1 (Sept. 20, 2008), p. 1. doi: 10.1007/BF02959820 (see p. 10).

[26] B. Grzadkowski, M. Iskrzynski, M. Misiak, and J. Rosiek: **Dimension-Six Terms in the Standard Model Lagrangian**. In: *JHEP*, **1010**: (2010), p. 085. doi: 10.1007/JHEP10(2010)085. arXiv: 1008.4884 [hep-ph] (see pp. 12–13, 16).

[27] J.A. Aguilar Savvedra, C. Degrande, G. Durieux, et al.: **Constraining the MSMEFT in the top sector at the LHC**. Working document for the TOP LHC WG. June 2017. url: http://www.desy.de/~durieux/topbasis/basis_note.pdf (see p. 12).

[28] Andy Buckley, Christoph Englert, James Ferrando, et al.: **Constraining top quark effective theory in the LHC Run II era**. In: *JHEP*, **04**: (2016), p. 015. doi: 10.1007/JHEP04(2016)015. arXiv: 1512.03360 [hep-ph] (see p. 13).

[29] Yorikiyo Nagashima: **Beyond the standard model of elementary particle physics**. Weinheim, Germany: Wiley-VCH Verlag, 2014. url: http://www-spires.fnal.gov/spires/find/books/www?cl=QC793.2.N34::2014 (see p. 14).

[30] P. A. R. Ade et al.: **Planck 2015 results. XIII. Cosmological parameters**. In: *Astron. Astrophys.*, **594**: (2016), A13. doi: 10.1051/0004-6361/201525830. arXiv: 1502.01589 [astro-ph.CO] (see p. 14).

[31] P. J. E. Peebles and Bharat Ratra: **The Cosmological constant and dark energy**. In: *Rev. Mod. Phys.*, **75**: (2003), pp. 559–606. doi: 10.1103/RevModPhys.75.559. arXiv: astro-ph/0207347 [astro-ph] (see p. 14).

[32] A. D. Sakharov: **Violation of CP Invariance, c Asymmetry, and Baryon Asymmetry of the Universe**. In: *Pisma Zh. Eksp. Teor. Fiz.*, **5**: (1967). [Usp. Fiz. Nauk161,61(1991)], pp. 32–35. doi: 10.1070/PU1991v034n05ABEH002497 (see p. 14).

[33] Gustavo Burdman: **New solutions to the hierarchy problem**. In: *Braz. J. Phys.*, **37**: (2007), pp. 506–513. doi: 10.1590/S0103-97332007000400006. arXiv: hep-ph/0703194 [hep-ph] (see p. 14).

[34] T. et al. Aaltonen: **Search for the Flavor-Changing Neutral-Current Decay $t \to Zq$ in $p\overline{p}$ Collisions at $\sqrt{s} = 1.96$ TeV**. In: *Phys. Rev. Lett.*, **101**: (19 Nov. 2008), p. 192002. doi: 10.1103/PhysRevLett.101.192002 (see p. 15).

[35] Victor Mukhamedovich Abazov et al.: **Search for flavour changing neutral currents via quark-gluon couplings in single top quark production using 2.3 fb^{-1} of $p\bar{p}$ collisions**. In: *Phys. Lett.*, **B693**: (2010), pp. 81–87. doi: 10.1016/j.physletb.2010.08.011. arXiv: 1006.3575 [hep-ex] (see p. 15).

[36] Georges Aad et al.: **Search for flavour-changing neutral current top-quark decays to qZ in pp collision data collected with the ATLAS detector at $\sqrt{s} = 8$ TeV**. In: *Eur. Phys. J.*, **C76**:1 (2016), p. 12. doi: 10.1140/epjc/s10052-015-3851-5. arXiv: 1508.05796 [hep-ex] (see p. 15).

[37] Georges Aad et al.: **Search for single top-quark production via flavour-changing neutral currents at 8 TeV with the ATLAS detector**. In: *Eur. Phys. J.*, **C76**:2 (2016), p. 55. doi: 10.1140/epjc/s10052-016-3876-4. arXiv: 1509.00294 [hep-ex] (see pp. 15, 19).

[38] Georges Aad et al.: **Search for flavour-changing neutral current top quark decays $t \to Hq$ in pp collisions at $\sqrt{s} = 8$ TeV with the ATLAS detector**. In: *JHEP*, **12**: (2015), p. 061. doi: 10.1007/JHEP12(2015)061. arXiv: 1509.06047 [hep-ex] (see p. 15).

[39] Morad Aaboud et al.: **Search for top quark decays $t \to qH$, with $H \to \gamma\gamma$, in $\sqrt{s} = 13$ TeV pp collisions using the ATLAS detector**. In: (2017). arXiv: 1707.01404 [hep-ex] (see pp. 15, 19).

[40] **Search for flavour-changing neutral current top quark decays $t \to qZ$ in proton-proton collisions at $\sqrt{s} = 13$ TeV with the ATLAS Detector**. Tech. rep. ATLAS-CONF-2017-070. Geneva: *CERN*, Sept. 2017. URL: https://cds.cern.ch/record/2285808 (see pp. 15, 19).

[41] Albert M Sirunyan et al.: **Search for associated production of a Z boson with a single top quark and for tZ flavour-changing interactions in pp collisions at $\sqrt{s}$ = 8 TeV**. In: (2017). arXiv: 1702.01404 [hep-ex] (see pp. 15, 19).

[42] Serguei Chatrchyan et al.: **Search for Flavor-Changing Neutral Currents in Top-Quark Decays $t \to Zq$ in pp Collisions at $\sqrt{s} = 8$TeV**. In: *Phys. Rev. Lett.*, **112**:17 (2014), p. 171802. DOI: 10.1103/PhysRevLett.112.171802. arXiv: 1312.4194 [hep-ex] (see p. 15).

[43] Vardan Khachatryan et al.: **Search for anomalous single top quark production in association with a photon in pp collisions at $\sqrt{s} = 8$ TeV**. In: *JHEP*, **04**: (2016), p. 035. DOI: 10.1007/JHEP04(2016)035. arXiv: 1511.03951 [hep-ex] (see pp. 15, 19).

[44] Vardan Khachatryan et al.: **Search for top quark decays via Higgs-boson-mediated flavor-changing neutral currents in pp collisions at $\sqrt{s} = 8$ TeV**. In: *JHEP*, **02**: (2017), p. 079. DOI: 10.1007/JHEP02(2017)079. arXiv: 1610.04857 [hep-ex] (see p. 15).

[45] **Search for the flavor-changing interactions of the top quark with the Higgs boson in $H \to b\bar{b}$ channel at $\sqrt{s} = 13$ TeV**. Tech. rep. CMS-PAS-TOP-17-003. Geneva: *CERN*, 2017. URL: https://cds.cern.ch/record/2284743 (see p. 15).

[46] M. Beneke et al.: **Top quark physics**. In: *1999 CERN Workshop on standard model physics (and more) at the LHC, CERN, Geneva, Switzerland, 25-26 May: Proceedings*. 2000, pp. 419–529. arXiv: hep-ph/0003033 [hep-ph]. URL: http://weblib.cern.ch/abstract?CERN-TH-2000-100 (see p. 17).

[47] Jun Gao, Chong Sheng Li, and Hua Xing Zhu: **Top Quark Decay at Next-to-Next-to Leading Order in QCD**. In: *Phys. Rev. Lett.*, **110**:4 (2013), p. 042001. DOI: 10.1103/PhysRevLett.110.042001. arXiv: 1210.2808 [hep-ph] (see pp. 18, 47).

[48] Stephen Myers: **The LEP Collider, from design to approval and commissioning**. John Adams' Lecture. Delivered at CERN, 26 Nov 1990. Geneva: CERN, 1991. URL: http://cds.cern.ch/record/226776 (see p. 23).

[49] Stephen Holmes, Ronald S Moore, and Vladimir Shiltsev: **Overview of the Tevatron collider complex: goals, operations and performance**. In: *Journal of Instrumentation*, **6**:08 (2011), T08001. URL: http://stacks.iop.org/1748-0221/6/i=08/a=T08001 (see p. 23).

[50] R. Barate et al.: **Search for the standard model Higgs boson at LEP**. In: *Phys. Lett.*, **B565**: (2003), pp. 61–75. DOI: 10.1016/S0370-2693(03)00614-2. arXiv: hep-ex/0306033 [hep-ex] (see p. 23).

[51] Kenneth Herner: **Higgs Boson Studies at the Tevatron**. In: *Nucl. Part. Phys. Proc.*, **273-275**: (2016), pp. 852–856. doi: 10.1016/j.nuclphysbps.2015.09.131 (see p. 23).

[52] Abdelhak Djouadi: **The Anatomy of electro-weak symmetry breaking. I: The Higgs boson in the standard model**. In: *Phys. Rept.*, **457**: (2008), pp. 1–216. doi: 10.1016/j.physrep.2007.10.004. arXiv: hep-ph/0503172 [hep-ph] (see p. 23).

[53] Lyndon Evans and Philip Bryant: **LHC Machine**. In: *Journal of Instrumentation*, **3**:08 (2008), S08001. url: http://stacks.iop.org/1748-0221/3/i=08/a=S08001 (see p. 23).

[54] Thomas Sven Pettersson and P Lefèvre: **The Large Hadron Collider: conceptual design**. Tech. rep. CERN-AC-95-05-LHC. Oct. 1995, p. 20 and 22. url: https://cds.cern.ch/record/291782 (see p. 23).

[55] Jorg Wenninger and Ezio Todesco: **Large Hadron Collider momentum calibration and accuracy**. Tech. rep. CERN-ACC-2017-0007. Geneva: *CERN*, Feb. 2017. url: https://cds.cern.ch/record/2254678 (see p. 24).

[56] Cinzia De Melis: **The CERN accelerator complex. Complexe des accélérateurs du CERN**. In: (July 2016). General Photo. url: https://cds.cern.ch/record/2197559 (see p. 24).

[57] Antonella Del Rosso: **HL-LHC updates in Japan. Projet HL-LHC : une réunion fait le point au Japon**. In: BUL-NA-2014-272. 51/2014 (Dec. 2014), p. 4. url: https://cds.cern.ch/record/1975962 (see p. 25).

[58] Oliver Sim Brüning, Paul Collier, P Lebrun, et al.: **LHC Design Report**. CERN Yellow Reports: Monographs. Geneva: CERN, 2004. url: https://cds.cern.ch/record/782076 (see p. 25).

[59] G. Aad et al.: **The ATLAS Experiment at the CERN Large Hadron Collider**. In: *JINST*, **3**: (2008), S08003. doi: 10.1088/1748-0221/3/08/S08003 (see p. 25).

[60] S. Chatrchyan et al.: **The CMS Experiment at the CERN LHC**. In: *JINST*, **3**: (2008), S08004. doi: 10.1088/1748-0221/3/08/S08004 (see pp. 25, 33–35).

[61] K. Aamodt et al.: **The ALICE experiment at the CERN LHC**. In: *JINST*, **3**: (2008), S08002. doi: 10.1088/1748-0221/3/08/S08002 (see p. 25).

[62] A. Augusto Alves Jr. et al.: **The LHCb Detector at the LHC**. In: *JINST*, **3**: (2008), S08005. doi: 10.1088/1748-0221/3/08/S08005 (see p. 25).

[63] M. Bongi et al.: **Astroparticle physics at LHC: The LHCf experiment ready for data taking**. In: *Nucl. Instrum. Meth.*, **A612**: (2010), pp. 451–454. doi: 10.1016/j.nima.2009.08.039 (see p. 26).

[64] G. Anelli et al.: **The TOTEM experiment at the CERN Large Hadron Collider**. In: *JINST*, **3**: (2008), S08007. doi: 10.1088/1748-0221/3/08/S08007 (see p. 26).

[65] B. Acharya et al.: **The Physics Programme Of The MoEDAL Experiment At The LHC**. In: *Int. J. Mod. Phys.*, **A29**: (2014), p. 1430050. doi: 10.1142/S0217751X14300506. arXiv: 1405.7662 [hep-ph] (see p. 26).

[66] by James Gillies: **Luminosity? Why don't we just say collision rate?** In: (Mar. 2011). url: http://cds.cern.ch/record/1997001 (see p. 26).

[67] BY HARRIET JARLETT and HARRIET KIM JARLETT: **LHC pushes limits of performance**. In: (Aug. 2016). URL: http://cds.cern.ch/record/2212301 (see p. 26).

[68] CMS COLLABORATION. Okt 2017. URL: https://twiki.cern.ch/twiki/bin/view/CMSPublic/LumiPublicResults#Online_Luminosity_AN2 (see p. 27).

[69] **Technical proposal**. LHC Tech. Proposal. Cover title : CMS, the Compact Muon Solenoid : technical proposal. Geneva: CERN, 1994. URL: https://cds.cern.ch/record/290969 (see p. 27).

[70] G. L. BAYATIAN et al.: **CMS physics: Technical design report**. In: (2006) (see p. 27).

[71] G L BAYATIAN, S CHATRCHYAN, G HMAYAKYAN, et al.: **CMS Physics: Technical Design Report Volume 1: Detector Performance and Software**. Technical Design Report CMS. There is an error on cover due to a technical problem for some items. Geneva: CERN, 2006. URL: https://cds.cern.ch/record/922757 (see pp. 27, 32, 57).

[72] CMS COLLABORATION: **Detector Drawings**. CMS Collection. Mar. 2012. URL: https://cds.cern.ch/record/1433717 (see p. 28).

[73] S CHATRCHYAN, V KHACHATRYAN, A M SIRUNYAN, et al.: **Performance of the CMS Drift Tube Chambers with Cosmic Rays**. In: *J. Instrum.*, **5**:arXiv:0911.4855. CMS-CFT-09-012 (Nov. 2009), T03015 . 47 p. URL: http://cds.cern.ch/record/1223944 (see pp. 30–31).

[74] TOM DODINGTON: **News from the CMS experimental site: 22 November 2013.** Nov. 2013. URL: http://cms.web.cern.ch/news/news-point-5-22-november-2013 (see p. 31).

[75] INSTITUTE OF RESEARCH INTO THE FUNDAMENTAL LAWS THE UNIVERSE: **The CMS detector superconducting solenoid**. Jan. 2006. URL: http://irfu.cea.fr/en/Phocea/Vie_des_labos/Ast/ast_visu.php?id_ast=839 (see p. 33).

[76] FERGUS WILSON: **Experimental Particle Physics**. Apr. 2012. URL: http://slideplayer.com/slide/794631/ (see p. 33).

[77] EMRAH TIRAS, BURAK BILKI, and YASAR ONEL: **Commissioning of CMS Forward Hadron Calorimeters with Upgraded Multi-anode PMTs and μTCA Readout**. In: (2016). arXiv: 1611.05232 [physics.ins-det] (see p. 34).

[78] LUCAS TAYLOR: **Experimental Particle Physics**. Nov. 2011. URL: http://cms.web.cern.ch/news/electromagnetic-calorimeter (see p. 34).

[79] **Proceedings, 34th International Conference on High Energy Physics (ICHEP 2008)** URL: http://www.slac.stanford.edu/econf/C080730 (see p. 34).

[80] L. BRIANZA: **Precision crystal calorimetry in LHC Run II with the CMS ECAL**. In: *Journal of Instrumentation*, **12**:01 (2017), p. C01069. URL: http://stacks.iop.org/1748-0221/12/i=01/a=C01069 (see pp. 35, 38).

[81] SERGUEI CHATRCHYAN, KHACHATRYAN, et al.: **Description and performance of track and primary-vertex reconstruction with the CMS tracker**. In: *J. Instrum.*, **9**:arXiv:1405.6569 CERN-PH-EP-2014-070. CMS-TRK-11-001 (May 2014). Comments: Replaced with published version. Added journal reference and DOI, P10009. 80 p. URL: http://cds.cern.ch/record/1704291 (see pp. 35, 58).

[82] by Christine Sutton: **Chronicles of CMS: the saga of LS1**. In: (May 2015). url: http://cds.cern.ch/record/2024986 (see p. 36).

[83] **A beautiful barrel for CMS**. In: (Mar. 2014). url: http://cds.cern.ch/record/1998635 (see p. 36).

[84] Vardan Khachatryan et al.: **The CMS trigger system**. In: *JINST*, **12**:01 (2017), P01020. doi: 10.1088/1748-0221/12/01/P01020. arXiv: 1609.02366 [physics.ins-det] (see p. 37).

[85] by Corinne Pralavorio and Corinne Pralavorio: **Major work to ready the LHC experiments for Run 2**. In: (May 2015). url: http://cds.cern.ch/record/2024977 (see p. 37).

[86] Luigi Guiducci: **CMS muon system towards LHC Run 2 and beyond**. Tech. rep. CMS-CR-2014-333. Geneva: *CERN*, Oct. 2014. url: https://cds.cern.ch/record/1966038 (see p. 38).

[87] Carlo Battilana: **The CMS muon system status and upgrades for LHC run-2 and performance of muon reconstruction with 13 TeV data**. Tech. rep. CMS-CR-2016-437. Geneva: *CERN*, Dec. 2016. url: http://cds.cern.ch/record/2239185 (see p. 38).

[88] Serguei Chatrchyan et al.: **Energy Calibration and Resolution of the CMS Electromagnetic Calorimeter in pp Collisions at $\sqrt{s} = 7$ TeV**. In: *JINST*, **8**: (2013). [JINST8,9009(2013)], P09009. doi: 10.1088/1748-0221/8/09/P09009. arXiv: 1306.2016 [hep-ex] (see p. 38).

[89] **Cool running for CMS tracker**. In: (Mar. 2014). url: http://cds.cern.ch/record/1998606 (see p. 38).

[90] L. Cadamuro: **The CMS Level-1 trigger system for LHC Run II**. In: *Journal of Instrumentation*, **12**:03 (2017), p. C03021. url: http://stacks.iop.org/1748-0221/12/i=03/a=C03021 (see p. 38).

[91] David Aaron Matzner Dominguez, D. Abbaneo, K. Arndt, et al.: **CMS Technical Design Report for the Pixel Detector Upgrade**. In: (2012) (see p. 39).

[92] Hanno Christopher Perrey: **Plans and Status of the Phase I Upgrade of the CMS Pixel Tracker**. Tech. rep. CMS-CR-2014-005. Geneva: *CERN*, Jan. 2014. url: http://cds.cern.ch/record/1644757 (see p. 39).

[93] Claudio Grandi, David Stickland, Lucas Taylor, Achille Petrilli, and Alain Hervé: **CMS Computing Model: The "CMS Computing Model RTAG"**. Tech. rep. CMS-NOTE-2004-031. CERN-LHCC-2004-035. LHCC-G-083. Geneva: *CERN*, Dec. 2004. url: http://cds.cern.ch/record/814248 (see p. 39).

[94] Christoph Eck, J Knobloch, Leslie Robertson, et al.: **LHC computing Grid: Technical Design Report. Version 1.06 (20 Jun 2005)**. Technical Design Report LCG. Geneva: CERN, 2005. url: https://cds.cern.ch/record/840543 (see p. 39).

[95] Worldwide LHC Computing Grid: **WorldWide LHC Computing Gird - 2017**. Oct. 2017. url: http://wlcg-public.web.cern.ch (see p. 40).

[96] John C. Collins, Davison E. Soper, and George F. Sterman: **Factorization of Hard Processes in QCD**. In: *Adv. Ser. Direct. High Energy Phys.*, **5**: (1989), pp. 1–91. doi: 10.1142/9789814503266_0001. arXiv: hep-ph/0409313 [hep-ph] (see p. 41).

[97] Ringaile Placakyte: **Parton Distribution Functions**. In: *Proceedings, 31st International Conference on Physics in collisions (PIC 2011): Vancouver, Canada, August 28-September 1, 2011*. 2011. arXiv: 1111.5452 [hep-ph]. url: https://inspirehep.net/record/954990/files/arXiv:1111.5452.pdf (see p. 41).

[98] Richard D. Ball, Valerio Bertone, Stefano Carrazza, et al.: **Parton distributions for the LHC run II**. In: *Journal of High Energy Physics*, **2015**:4 (2015), p. 40. doi: 10.1007/JHEP04(2015)040 (see p. 41).

[99] Jon Butterworth et al.: **PDF4LHC recommendations for LHC Run II**. In: *J. Phys.*, **G43**: (2016), p. 023001. doi: 10.1088/0954-3899/43/2/023001. arXiv: 1510.03865 [hep-ph] (see pp. 41–42).

[100] H. Abramowicz and A. Caldwell: **HERA collider physics**. In: *Rev. Mod. Phys.*, **71**: (1999), pp. 1275–1410. doi: 10.1103/RevModPhys.71.1275. arXiv: hep-ex/9903037 [hep-ex] (see p. 42).

[101] Stephen Holmes, Ronald S. Moore, and Vladimir Shiltsev: **Overview of the Tevatron Collider Complex: Goals, Operations and Performance**. In: *JINST*, **6**: (2011), T08001. doi: 10.1088/1748-0221/6/08/T08001. arXiv: 1106.0909 [physics.acc-ph] (see p. 42).

[102] Juan Rojo et al.: **The PDF4LHC report on PDFs and LHC data: Results from Run I and preparation for Run II**. In: *J. Phys.*, **G42**: (2015), p. 103103. doi: 10.1088/0954-3899/42/10/103103. arXiv: 1507.00556 [hep-ph] (see p. 42).

[103] Alan D. Martin: **Proton structure, Partons, QCD, DGLAP and beyond**. In: *Acta Phys. Polon.*, **B39**: (2008), pp. 2025–2062. arXiv: 0802.0161 [hep-ph] (see p. 42).

[104] J. Pumplin, D. Stump, R. Brock, et al.: **Uncertainties of predictions from parton distribution functions. 2. The Hessian method**. In: *Phys. Rev.*, **D65**: (2001), p. 014013. doi: 10.1103/PhysRevD.65.014013. arXiv: hep-ph/0101032 [hep-ph] (see p. 42).

[105] Franz Mandl and Graham G Shaw: **Quantum field theory; 2nd ed.** New York, NY: Wiley, 2010. url: https://cds.cern.ch/record/1236742 (see p. 44).

[106] S Banerjee: **CMS Simulation Software**. In: *Journal of Physics: Conference Series*, **396**:2 (2012), p. 022003. url: http://stacks.iop.org/1742-6596/396/i=2/a=022003 (see p. 44).

[107] M Hildreth, V N Ivanchenko, D J Lange, and M J Kortelainen: **CMS Full Simulation for Run-2**. In: *Journal of Physics: Conference Series*, **664**:7 (2015), p. 072022. url: http://stacks.iop.org/1742-6596/664/i=7/a=072022 (see p. 44).

[108] S. Agostinelli, J. Allison, K. Amako, et al.: **Geant4-a simulation toolkit**. In: *Nuclear Instruments and Methods in Physics Research Section A: Accelerators, Spectrometers, Detectors and Associated Equipment*, **506**:3 (2003), pp. 250–303. doi: https://doi.org/10.1016/S0168-9002(03)01368-8 (see pp. 44, 46).

[109] Michael H. Seymour and Marilyn Marx: **Monte Carlo Event Generators**. In: *Proceedings, 69th Scottish Universities Summer School in Physics : LHC Phenomenology (SUSSP69): St.Andrews, Scotland, August 19-September 1, 2012*. 2013, pp. 287–319. doi: 10.1007/978-3-319-05362-2_8. arXiv: 1304.6677 [hep-ph] (see p. 44).

[110] Torbjorn Sjöstrand: **Monte Carlo Tools**. In: *Proceedings, 65th Scottish Universities Summer School in Physics: LHC Physics (SUSSP65): St. Andrews, UK, August 16-29, 2009*. 2009, pp. 309–339. doi: 10.1201/b11865-14. arXiv: 0911.5286 [hep-ph] (see p. 44).

[111] Stefan Höche: **Introduction to parton-shower event generators**. In: *Proceedings, Theoretical Advanced Study Institute in Elementary Particle Physics: Journeys Through the Precision Frontier: Amplitudes for Colliders (TASI 2014): Boulder, Colorado, June 2-27, 2014*. 2015, pp. 235–295. doi: 10.1142/9789814678766_0005. arXiv: 1411.4085 [hep-ph] (see pp. 44–45).

[112] Adam Alloul, Neil D. Christensen, Céline Degrande, Claude Duhr, and Benjamin Fuks: **FeynRules 2.0 - A complete toolbox for tree-level phenomenology**. In: *Comput. Phys. Commun.*, **185**: (2014), pp. 2250–2300. doi: 10.1016/j.cpc.2014.04.012. arXiv: 1310.1921 [hep-ph] (see p. 44).

[113] Celine Degrande, Claude Duhr, Benjamin Fuks, et al.: **UFO - The Universal FeynRules Output**. In: *Comput. Phys. Commun.*, **183**: (2012), pp. 1201–1214. doi: 10.1016/j.cpc.2012.01.022. arXiv: 1108.2040 [hep-ph] (see p. 44).

[114] Johan Alwall, Michel Herquet, Fabio Maltoni, Olivier Mattelaer, and Tim Stelzer: **MadGraph 5 : Going Beyond**. In: *JHEP*, **06**: (2011), p. 128. doi: 10.1007/JHEP06(2011)128. arXiv: 1106.0522 [hep-ph] (see pp. 45, 48).

[115] Michelangelo L. Mangano, Mauro Moretti, Fulvio Piccinini, and Michele Treccani: **Matching matrix elements and shower evolution for top-quark production in hadronic collisions**. In: *JHEP*, **01**: (2007), p. 013. doi: 10.1088/1126-6708/2007/01/013. arXiv: hep-ph/0611129 [hep-ph] (see p. 45).

[116] Torbjorn Sjostrand, Stefan Ask, Jesper R. Christiansen, et al.: **An introduction to {PYTHIA} 8.2**. In: *Computer Physics Communications*, **191**: (2015), pp. 159–177. doi: http://dx.doi.org/10.1016/j.cpc.2015.01.024 (see pp. 45–46).

[117] Torbjorn Sjostrand, Stephen Mrenna, and Peter Z. Skands: **PYTHIA 6.4 Physics and Manual**. In: *JHEP*, **0605**: (2006), p. 026. doi: 10.1088/1126-6708/2006/05/026. arXiv: hep-ph/0603175 [hep-ph] (see pp. 45–46).

[118] Torbjorn Sjostrand, Stefan Ask, Jesper R. Christiansen, et al.: **An Introduction to PYTHIA 8.2**. In: *Comput. Phys. Commun.*, **191**: (2015), pp. 159–177. doi: 10.1016/j.cpc.2015.01.024. arXiv: 1410.3012 [hep-ph] (see pp. 45–46, 48–49).

[119] Johan Alwall et al.: **Comparative study of various algorithms for the merging of parton showers and matrix elements in hadronic collisions**. In: *Eur. Phys. J.*, **C53**: (2008), pp. 473–500. doi: 10.1140/epjc/s10052-007-0490-5. arXiv: 0706.2569 [hep-ph] (see pp. 45, 48).

[120] J. Alwall, R. Frederix, S. Frixione, et al.: **The automated computation of tree-level and next-to-leading order differential cross sections, and their matching to parton shower simulations**. In: *JHEP*, **07**: (2014), p. 079. doi: 10.1007/JHEP07(2014)079. arXiv: 1405.0301 [hep-ph] (see p. 45).

[121] Stefano Frixione and Bryan R. Webber: **Matching NLO QCD computations and parton shower simulations**. In: *JHEP*, **06**: (2002), p. 029. doi: 10.1088/1126-6708/2002/06/029. arXiv: hep-ph/0204244 [hep-ph] (see pp. 45, 48).

[122] Rikkert Frederix and Stefano Frixione: **Merging meets matching in MC@NLO**. In: *JHEP*, **12**: (2012), p. 061. doi: 10.1007/JHEP12(2012)061. arXiv: 1209.6215 [hep-ph] (see p. 45).

[123] Simone Alioli, Paolo Nason, Carlo Oleari, and Emanuele Re: **A general framework for implementing NLO calculations in shower Monte Carlo programs: the POWHEG BOX**. In: *Journal of High Energy Physics*, **2010**:6 (2010), p. 43. doi: 10.1007/JHEP06(2010)043 (see pp. 45, 48).

[124] Simone Alioli, Paolo Nason, Carlo Oleari, and Emanuele Re: **NLO single-top production matched with shower in POWHEG: s - and t -channel contributions**. In: *Journal of High Energy Physics*, **2009**:09 (2009), p. 111. url: http://stacks.iop.org/1126-6708/2009/i=09/a=111 (see pp. 45, 48).

[125] Stefano Frixione, Paolo Nason, and Carlo Oleari: **Matching NLO QCD computations with parton shower simulations: the POWHEG method**. In: *Journal of High Energy Physics*, **2007**:11 (2007), p. 070. url: http://stacks.iop.org/1126-6708/2007/i=11/a=070 (see pp. 45, 48).

[126] Simone Alioli, Paolo Nason, Carlo Oleari, and Emanuele Re: **A general framework for implementing NLO calculations in shower Monte Carlo programs: the POWHEG BOX**. In: *JHEP*, **06**: (2010), p. 043. doi: 10.1007/JHEP06(2010)043. arXiv: 1002.2581 [hep-ph] (see pp. 45, 48).

[127] Stefano Frixione, Paolo Nason, and Carlo Oleari: **Matching NLO QCD computations with Parton Shower simulations: the POWHEG method**. In: *JHEP*, **11**: (2007), p. 070. doi: 10.1088/1126-6708/2007/11/070. arXiv: 0709.2092 [hep-ph] (see pp. 45, 48).

[128] Paolo Nason: **A New method for combining NLO QCD with shower Monte Carlo algorithms**. In: *JHEP*, **11**: (2004), p. 040. doi: 10.1088/1126-6708/2004/11/040. arXiv: hep-ph/0409146 [hep-ph] (see pp. 45, 48).

[129] Andrei V. Gritsan, Raoul Röntsch, Markus Schulze, and Meng Xiao: **Constraining anomalous Higgs boson couplings to the heavy flavor fermions using matrix element techniques**. In: *Phys. Rev.*, **D94**:5 (2016), p. 055023. doi: 10.1103/PhysRevD.94.055023. arXiv: 1606.03107 [hep-ph] (see pp. 45, 48).

[130] Ian Anderson et al.: **Constraining anomalous HVV interactions at proton and lepton colliders**. In: *Phys. Rev.*, **D89**:3 (2014), p. 035007. doi: 10.1103/PhysRevD.89.035007. arXiv: 1309.4819 [hep-ph] (see pp. 45, 48).

[131] Sara Bolognesi, Yanyan Gao, Andrei V. Gritsan, et al.: **On the spin and parity of a single-produced resonance at the LHC**. In: *Phys. Rev.*, **D86**: (2012), p. 095031. doi: 10.1103/PhysRevD.86.095031. arXiv: 1208.4018 [hep-ph] (see pp. 45, 48).

[132] Yanyan Gao, Andrei V. Gritsan, Zijin Guo, et al.: **Spin determination of single-produced resonances at hadron colliders**. In: *Phys. Rev.*, **D81**: (2010), p. 075022. doi: 10.1103/PhysRevD.81.075022. arXiv: 1001.3396 [hep-ph] (see pp. 45, 48).

[133] Pierre Artoisenet, Rikkert Frederix, Olivier Mattelaer, and Robbert Rietkerk: **Automatic spin-entangled decays of heavy resonances in Monte Carlo simulations**. In: *JHEP*, **03**: (2013), p. 015. doi: 10.1007/JHEP03(2013)015. arXiv: 1212.3460 [hep-ph] (see p. 46).

[134] V. Khachatryan and etal: **Event generator tunes obtained from underlying event and multiparton scattering measurements**. In: *The European Physical Journal C*, **76**:3 (Mar. 17, 2016), p. 155. doi: 10.1140/epjc/s10052-016-3988-x (see p. 46).

[135] Richard D. Ball et al.: **Parton distributions with LHC data**. In: *Nucl. Phys.*, **B867**: (2013), pp. 244–289. doi: 10.1016/j.nuclphysb.2012.10.003. arXiv: 1207.1303 [hep-ph] (see p. 46).

[136] Yue Zhang, Bo Hua Li, Chong Sheng Li, Jun Gao, and Hua Xing Zhu: **Next-to-leading order QCD corrections to the top quark associated with γ production via model-independent flavor-changing neutral-current couplings at hadron colliders**. In: *Phys. Rev.*, **D83**: (2011), p. 094003. doi: 10.1103/PhysRevD.83.094003. arXiv: 1101.5346 [hep-ph] (see p. 47).

[137] J Alwall, R Frederix, S Frixione, et al.: **The automated computation of tree-level and next-to-leading order differential cross sections, and their matching to parton shower simulations**. In: *JHEP*, **07**:arXiv:1405.0301. CERN-PH-TH-2014-064. CP3-14-18. LPN14-066. MCNET-14-09. ZU-TH 14-14 (May 2014), 079. 158 p. url: http://cds.cern.ch/record/1699128 (see p. 48).

[138] Rikkert Frederix and Stefano Frixione: **Merging meets matching in MC@NLO**. In: *JHEP*, **12**:arXiv:1209.6215. CERN-PH-TH-2012-247. ZU-TH 21-12 (Sept. 2012). Comments: 40 pages, 14 figures, 061. 40 p. url: http://cds.cern.ch/record/1481985 (see p. 48).

[139] **CMS Monte Carlo Generator Group** (see pp. 48–49).

[140] T. Gehrmann, M. Grazzini, S. Kallweit, et al.: **W^+W^- Production at Hadron Colliders in Next to Next to Leading Order QCD**. In: *Phys. Rev. Lett.*, **113**:21 (2014), p. 212001. doi: 10.1103/PhysRevLett.113.212001. arXiv: 1408.5243 [hep-ph] (see p. 49).

[141] A. Hoecker, P. Speckmayer, J. Stelzer, et al.: **TMVA - Toolkit for Multivariate Data Analysis**. In: *ArXiv Physics e-prints*, (Mar. 2007). eprint: physics/0703039 (see p. 50).

[142] R. Brun and F. Rademakers: **ROOT: An object oriented data analysis framework**. In: *Nucl. Instrum. Meth.*, **A389**: (1997), pp. 81–86. doi: 10.1016/S0168-9002(97)00048-X (see p. 50).

[143] A. Mayr, H. Binder, O. Gefeller, and M. Schmid: **The Evolution of Boosting Algorithms - From Machine Learning to Statistical Modelling**. In: *ArXiv e-prints*, (Mar. 2014). arXiv: 1403.1452 [stat.ME] (see p. 51).

[144] Olaf Behnke, Kevin Kroninger, Gregory Schott, and Thomas Schorner-Sadenius **Data Analysis in High Energy Physics: A Practical Guide to Statistical Methods**. 1st. Wiley-VCH, 2013 (see p. 51).

[145] Christian Böser, Simon Fink, and Steffen Röcker: **Introduction to Boosted Decision Trees: A multivariate approach to classification problems.** Presented at the 'KSETA Doktoranden' workshop, Lauterbad. July 2014. URL: https://indico.scc.kit.edu/indico/event/48/session/4/contribution/35/material/slides/0.pdf (see p. 51).

[146] Serguei Chatrchyan et al.: **Combined results of searches for the standard model Higgs boson in pp collisions at $\sqrt{s} = 7$ TeV**. In: *Phys. Lett.*, **B710**: (2012), pp. 26–48. DOI: 10.1016/j.physletb.2012.02.064. arXiv: 1202.1488 [hep-ex] (see p. 52).

[147] Glen Cowan, Kyle Cranmer, Eilam Gross, and Ofer Vitells: **Asymptotic formulae for likelihood-based tests of new physics**. In: *Eur. Phys. J.*, **C71**: (2011). [Erratum: Eur. Phys. J.C73,2501(2013)], p. 1554. DOI: 10.1140/epjc/s10052-011-1554-0, 10.1140/epjc/s10052-013-2501-z. arXiv: 1007.1727 [physics.data-an] (see pp. 52–53).

[148] **Observation of a new boson with a mass near 125 GeV**. Tech. rep. CMS-PAS-HIG-12-020. Geneva: *CERN*, 2012. URL: https://cds.cern.ch/record/1460438 (see p. 52).

[149] **Procedure for the LHC Higgs boson search combination in Summer 2011**. Tech. rep. CMS-NOTE-2011-005. ATL-PHYS-PUB-2011-11. Geneva: *CERN*, Aug. 2011. URL: http://cds.cern.ch/record/1379837 (see p. 52).

[150] Higgs working group: **Documentation of the RooStats based statistics tools for Higgs PAG**. Aug. 2017. URL: https://twiki.cern.ch/twiki/bin/viewauth/CMS/SWGuideHiggsAnalysisCombinedLimit (see p. 52).

[151] Lorenzo Moneta, Kevin Belasco, Kyle S. Cranmer, et al.: **The RooStats Project**. In: *PoS*, **ACAT2010**: (2010), p. 057. arXiv: 1009.1003 [physics.data-an] (see p. 52).

[152] Glen Cowan, Kyle Cranmer, Eilam Gross, and Ofer Vitells: **Asymptotic formulae for likelihood-based tests of new physics**. In: *The European Physical Journal C*, **71**:2 (Feb. 2011). DOI: 10.1140/epjc/s10052-011-1554-0. arXiv: 1007.1727 [hep-ph] (see p. 52).

[153] Thomas Junk: **Confidence level computation for combining searches with small statistics**. In: *Nuclear Instruments and Methods in Physics Research Section A: Accelerators, Spectrometers, Detectors and Associated Equipment*, **434**:2 (1999), pp. 435–443. DOI: https://doi.org/10.1016/S0168-9002(99)00498-2 (see p. 52).

[154] A L Read: **Presentation of search results: the CL s technique**. In: *Journal of Physics G: Nuclear and Particle Physics*, **28**:10 (2002), p. 2693. URL: http://stacks.iop.org/0954-3899/28/i=10/a=313 (see p. 52).

[155] A. M. Sirunyan et al.: **Particle-flow reconstruction and global event description with the CMS detector**. In: *JINST*, **12**: (2017), P10003. DOI: 10.1088/1748-0221/12/10/P10003. arXiv: 1706.04965 [physics.ins-det] (see pp. 56–59, 61, 63).

[156] R. Frühwirth: **Application of Kalman filtering to track and vertex fitting**. In: *Nuclear Instruments and Methods in Physics Research Section A: Accelerators, Spectrometers, Detectors and Associated Equipment*, **262**:2 (1987), pp. 444–450. DOI: http://dx.doi.org/10.1016/0168-9002(87)90887-4 (see p. 57).

[157] Pierre Billoir: **Progressive track recognition with a Kalman like fitting procedure**. In: *Comput. Phys. Commun.*, **57**: (1989), pp. 390–394. doi: 10.1016/0010-4655(89)90249-X (see p. 57).

[158] Serguei Chatrchyan et al.: **Performance of CMS muon reconstruction in pp collision events at $\sqrt{s} = 7$ TeV**. In: *JINST*, **7**: (2012), P10002. doi: 10.1088/1748-0221/7/10/P10002. arXiv: 1206.4071 [physics.ins-det] (see p. 57).

[159] W Adam, R Frühwirth, A Strandlie, and T Todorov: **Reconstruction of electrons with the Gaussian-sum filter in the CMS tracker at the LHC**. In: *Journal of Physics G: Nuclear and Particle Physics*, **31**:9 (2005), N9. url: http://stacks.iop.org/0954-3899/31/i=9/a=N01 (see p. 57).

[160] **Performance of electron reconstruction and selection with the CMS detector in proton-proton collisions at $\sqrt{s} = 8TeV$**. In: *Journal of Instrumentation*, **10**:06 (2015), P06005. url: http://stacks.iop.org/1748-0221/10/i=06/a=P06005 (see p. 58).

[161] **Electron and photon performance in CMS with the full 2016 data sample.** In: (Mar. 2017). url: http://cds.cern.ch/record/2255497 (see pp. 58, 63–64).

[162] K. Rose: **Deterministic annealing for clustering, compression, classification, regression, and related optimization problems**. In: *Proceedings of the IEEE*, **86**:11 (Nov. 1998), pp. 2210–2239. doi: 10.1109/5.726788 (see p. 58).

[163] Wolfgang Waltenberger: **Adaptive Vertex Reconstruction**. Tech. rep. CMS-NOTE-2008-033. Geneva: *CERN*, July 2008. url: https://cds.cern.ch/record/1166320 (see p. 58).

[164] Andreas Kornmayer: **The CMS Pixel Luminosity Telescope**. Tech. rep. CMS-CR-2015-121. Geneva: *CERN*, June 2015. url: https://cds.cern.ch/record/2039978 (see p. 59).

[165] **CMS Luminosity Measurements for the 2016 Data Taking Period**. Tech. rep. CMS-PAS-LUM-17-001. Geneva: *CERN*, 2017. url: http://cds.cern.ch/record/2257069 (see p. 59).

[166] **Measurement of the inelastic proton-proton cross section at $\sqrt{s} = 13$ TeV**. Tech. rep. CMS-PAS-FSQ-15-005. Geneva: *CERN*, 2016. url: https://cds.cern.ch/record/2145896 (see p. 60).

[167] **Pileup Removal Algorithms**. Tech. rep. CMS-PAS-JME-14-001. Geneva: *CERN*, 2014. url: http://cds.cern.ch/record/1751454.

[168] **Muon Identification and Isolation efficiency on full 2016 dataset**. In: (Mar. 2017). url: http://cds.cern.ch/record/2257968 (see pp. 60–62).

[169] **Effective areas used for Summer16 samples**. 2017. url: https://indico.cern.ch/event/482673/contributions/2187022/%20attachments/1282446/1905912/talk_electron_ID_spring16.pdf (see p. 64).

[170] Matteo Cacciari, Gavin P. Salam, and Gregory Soyez: **The Anti-k(t) jet clustering algorithm**. In: *JHEP*, **04**: (2008), p. 063. doi: 10.1088/1126-6708/2008/04/063. arXiv: 0802.1189 [hep-ph] (see p. 64).

[171] **Jet algorithms performance in 13 TeV data**. Tech. rep. CMS-PAS-JME-16-003. Geneva: *CERN*, 2017. url: http://cds.cern.ch/record/2256875 (see p. 65).

[172] V. Khachatryan et al.: **Jet energy scale and resolution in the CMS experiment in pp collisions at 8 TeV**. In: *Journal of Instrumentation*, **12**:02 (2017), P02014. URL: http://stacks.iop.org/1748-0221/12/i=02/a=P02014 (see pp. 65–67).

[173] **Jet energy scale and resolution performances with 13TeV data**. In: (June 2016). URL: http://cds.cern.ch/record/2160347 (see pp. 66–67).

[174] The CMS collaboration: **Identification of b-quark jets with the CMS experiment**. In: *Journal of Instrumentation*, **8**:04 (2013), P04013. URL: http://stacks.iop.org/1748-0221/8/i=04/a=P04013 (see pp. 67–68).

[175] **Identification of b quark jets at the CMS Experiment in the LHC Run 2**. Tech. rep. CMS-PAS-BTV-15-001. Geneva: *CERN*, 2016. URL: http://cds.cern.ch/record/2138504 (see pp. 67, 69).

[176] Nazar Bartosik: **Diagram showing the common principle of identification of jets initiated by b-hadron decays**. 2016. URL: http://bartosik.pp.ua/hep_sketches/btagging (see p. 68).

[177] **Identification of b quark jets at the CMS Experiment in the LHC Run 2**. Tech. rep. CMS-PAS-BTV-16-001. unpublished. Geneva: *CERN*, 2017 (see pp. 69–70).

[178] **Performance of missing energy reconstruction in 13 TeV pp collision data using the CMS detector**. Tech. rep. CMS-PAS-JME-16-004. Geneva: *CERN*, 2016. URL: http://cds.cern.ch/record/2205284 (see pp. 71, 76–77).

[179] Jordan Damgov: **Missing Et Optional Filters Run 2**. 2017. URL: https://twiki.cern.ch/twiki/bin/viewauth/CMS/MissingETOptionalFiltersRun2 (see p. 76).

[180] **EGM corrections for Moriond17**. URL: https://indico.cern.ch/event/613162/contributions/2472046/attachments/1410308/2156822/EGMSmearerAndRegression_PPD_022017.pdf (see p. 81).

[181] **Misalignment and Muon Scale corrections**. URL: https://www-cdf.fnal.gov/~jyhan/cms_momscl/rochcor_cmsnote.pdf (see p. 82).

[182] **Rochestor Correction**. Accessed: 2017-05-20. URL: https://twiki.cern.ch/twiki/bin/viewauth/CMS/RochcorMuon (see p. 82).